To the Graduate Council:

I am submitting herewith a dissertation written by Yinan Sun entitled "The Study of Crack Closure Phenomenon Following One Tensile Overload." I have examined the final electronic copy of this dissertation for form and content and recommend that it be accepted in the partial fulfillment of the requirements for the degree of Doctor of Philosophy, with a major in Materials Science and Engineering.

Peter K. Liaw
Major Professor

We have read this thesis
and recommend its acceptance:

Hahn Choo

YanFei Gao

John D. Landes

Accepted for the Council:

Carolyn R. Hodges
Dean of the
Graduate School

(Orginal signatures are on file with offical student records.)

The Study of Crack Closure Phenomenon Following One Tensile Overload

A Dissertation
Presented for the
Doctor of Philosophy
The University of Tennessee, Knoxville

Yinan Sun
May 2007

Acknowledgments

First and foremost, I am deeply indebted to my advisors, Dr. Peter K. Liaw and Dr. Hahn Choo. Their great efforts in guiding and supporting my research have been crucial for me to extend my potentials and develop my academic capabilities. I thank them for providing abundant opportunities and resources. Also, I would like to thank Dr. Yanfei Gao for many helpful discussions on the modeling part of my research. I would further like to thank Dr. Cam Hubbard at the Oak Ridge National Laboratory (ORNL) and Dr. Don Brown at the Los Alamos National Science Center (LANSCE) for generously giving me precious neutron-diffraction beam times, which made my thesis work possible.

I owe many thanks to those who did neutron experiments for me. Those are Dr. P. K. Liaw, Dr. H. Choo, Dr. C. Fan, Dr. D. Brown, Dr. K. An, Dr. C. Hubbard, and Dr. F. Tang. I also would like to thank Dr. R. Barabash, who did the X-ray microbeam experiments for me at the Advanced Photon Source (APS), and help me with the dislocation-density calculation.

I must express my appreciations to my family and many friends who have help relieve stresses of the graduate school, in particular, my husband, Yulin Lu, and my

son, James Lu, for putting up with me as a wife and a mother. I thank God everyday for giving them to me.

Finally, I would like to acknowledge the financial supports from the National Science Foundation (NSF), the Combined Research-Curriculum Development (CRCD) Programs (EEC-9527527 and EEC-0203415), the Integrative Graduate Education and Research Training (IGERT) Program (DGE-9987548), the International Materials Institutes (IMI) Program (DMR-0231320), and the Mayor Research Instrumentalities (MRI) Program (DMR-0421219) to the University of Tennessee (UT), Knoxville, with Ms. M. Poats, Drs. C. J. Van Hartesveldt, D. Dutta, W. Jenning, L. Goldlerg, L. Clesceri, C. Huber, and C. E. Bouldin as the program directors, respectively.

Abstract

During the load-controlled high-cycle fatigue test, when the overload was applied, it is shown that from the crack-growth rate (da/dN) versus stress-intensity-factor range (ΔK) curve, the crack-growth rate decreased, following the overload, which indicated the crack-closure phenomenon. The crack-growth-retardation period was observed after the overload. The goal of this study is to investigate the deformation evolution during tensile loading and unloading cycles using neutron diffraction.

Neutron diffraction is used to investigate the crack-closure phenomenon by measuring the changes in the elastic-lattice-strain profiles around the fatigue-crack tip in a compact-tension (CT) specimen during tensile loading and unloading cycles. Spatially-resolved-strain measurements were performed to determine the in-plane and through-thickness lattice-strain profiles ahead of the crack tip under a constant tensile load. The strain scanning was repeated under various applied loads ranging from 667 to 6,667 N. Subsequently, an overload at 8,889N was applied. The strain scans repeated. After the overload, large compressive strain fields were observed close to the crack tip, indicative of the crack-closure phenomena.

Residual strain/stress mapping using neutron diffraction was also designed to investigate the mechanism of the retardation phenomenon by mapping the changes in the lattice-strain profiles around the fatigue-crack tip in a series of compact-tension (CT) specimens, which were fatigued to various stages through the retardation period after the overload. Following the overload, compressive-strain fields were observed along the loading direction close to the crack tip. As the crack grows out of the retardation period, the residual compressive strains decreased. The results provide a microscopic understanding of the overload effect during cyclic loading.

The plastic deformation ahead of a fatigue-crack tip was measured from the diffraction-peak-width changes. The dislocation density was estimated from the full-width-half maximum (FWHM) of the diffraction peaks. High dislocation densities around the crack tip were observed after the overload. Furthermore, the plastic-zone size in front of the crack tip was estimated from the diffraction-peak broadening, which showed a good agreement with the calculated result. The plasticity-induced crack-closure phenomenon after an overload was observed.

The measured elastic strains and dislocation densities will be compared to the finite-element simulations that are based on an irreversible, hysteretic-cohesive interface model. The experimental and numerical results will be compared and discussed.

The deformation in the vicinity of the crack tip was not only studied with the neutron diffraction, but also the x-ray microbeam diffraction. The results help understand the overload effect, which induced a large plastic deformation causing dislocations inhomogeneously arranged around the crack tip. From neutron-diffraction measurements, the anisotropic line broadening was observed in front of the crack

tip. Furthermore, Laue patterns, obtained from the microbeam diffraction at different locations near the crack, provide a better spatial resolution and show alternating regions with high and low dislocation densities. Overall, the dislocation density was found to decrease with the distance from the crack tip.

Contents

1 Literature Review **1**

1.1 Background of the Chosen Material 1

1.2 Developments of Fracture Mechanics 5

1.3 Basic Concepts 6

1.4 Fatigue Mechanisms 11

1.4.1 Fatigue-Failure Mechanisms 16

1.4.2 Fatigue-Crack-Initiation Mechanisms 17

1.4.3 Fatigue-Crack-Growth Mechanisms 19

1.5 Overloading Effects 23

1.5.1 Plasticity-Induced Crack Closure 24

1.5.2 Roughness-Induced Closure 27

1.5.3 Oxide-Induced Closure 27

1.5.4 Phase-Transformation-Induced Crack Closure 28

1.5.5 Fatigue-Crack Deflection 29

1.5.6 Retardation 30

1.5.7 Retardation Following Tensile Overloads 32

1.5.8 Transient Effects Following Compressive Overloads 34
1.5.9 Load-Sequence Effects 35
1.5.10 Analyses of Variable-Amplitude Fatigue 39
1.5.11 Finite-Element Analyses of the Plasticity-Induced Fatigue-Crack Closure 41
1.5.12 Cohesive-Zone Modeling 45

2 Neutron-Diffraction Studies on Lattice-Strain Evolution around a Crack Tip during Tensile Loading and Unloading Cycles 57
2.1 Introduction 57
2.2 Experimental Details 60
2.3 Results and Discussions 63
2.4 Summary 67

3 The Study of Crack-Closure Phenomena after the Overload 68
3.1 Introduction 68
3.2 Experimental Details 71
3.2.1 Fatigue Experiments 71
3.2.2 Fatigue-Striation Measurements 72
3.2.3 Neutron-Diffraction Experiments 73
3.3 Results 74
3.3.1 Fatigue Experiments and Striation Measurements 74
3.3.2 Lattice-Strain Measurements from Neutron Diffraction 76
3.3.3 Peak-Width-Change Variation from Neutron diffraction 81

3.4 Discussion 83
3.4.1 Plasticity-Induced Crack Closure 83
3.4.2 Plasticity in Front of the Crack Tip 86
3.5 Conclusion 88

4 Multiscale Plastic Deformation Near A Fatigue Crack From Diffraction 89

4.1 Introduction 89
4.2 Experimental Details 92
4.3 Results and Discussions 94
4.4 Summary 100

5 Neutron-Diffraction Study and Cohesive-Interface Model of Fatigue-Crack-Deformation Behavior 102

5.1 Introduction 102
5.2 Experimental Details 103
5.3 Results and Discussions 106
5.4 Summary 110

6 Changes in Lattice-Strain Profiles around a Fatigue Crack through the Retardation Period after the Overload 111

6.1 Introduction 111
6.2 Experimental Details 112
6.3 Results and Discussions 115
6.4 Summary 118

7 The Study of Lattice Strain/Stress Mapping around a Fatigue Crack during the Retardation Period after an Overload Using Neutron Diffraction **119**

7.1 Introduction 119

7.2 Theory 121

7.3 Experimental Procedures 124

7.3.1 Specimen Preparation 124

7.3.2 Neutron Experiments 128

7.4 Results 129

7.4.1 Strain/Stress Profiles 129

7.4.2 Two-Dimensional (2-D) Strain-Mapping Contours 136

7.5 Discussions 138

7.5.1 Crack Closure 138

7.5.2 Perturbed-Plastic Zone 139

7.6 Conclusions 141

8 Conclusions **143**

9 Future Work **148**

Bibliography **150**

Vita **164**

List of Tables

1.1 Chemical composition of Type 316 low-carbon, nitrogen-added (LN) stainless steel (SS) (wt.%, weight percent) 1

1.2 Mechanical properties of Type 316 stainless steels at 27 and -196 °C . 4

7.1 Crack length of the specimens 128

7.2 Stress-intensity calculations and fatigue-plastic zone sizes for SP2, SP3, SP4, SP5, and SP6. 141

List of Figures

1.1 The three modes of loading a cracked body. 7

1.2 The crack-tip coordinate system and the stresses acting on an element ahead of the crack tip. 8

1.3 Elastic and elastic-plastic crack-tip-stress distributions in front of the crack tip and the plastic-zone sizes, r_y and r_p. [1] 10

1.4 Typical fatigue-crack-growth curves under a constant load range. [2] . 12

1.5 Typical fatigue-crack-growth diagram showing three different regimes. 15

1.6 Schematic of fatigue-crack growth across a specimen section, indicating three stages of fatigue failures. 16

1.7 Schematic showing the roughening of surfaces due to the formation of persistent slip bands (PSBs). 18

1.8 One of the various possible mechanisms of fatigue-crack growth. . . . 20

1.9 Schematic of the ductile rupture showing four stages. Bottom: the fracture surface illustrates dimples formed by large and small particles. 22

1.10 1. A schematic illustration of the mechanisms, which promote the retardation of fatigue-crack growth in the constant-amplitude fatigue. (a) plasticity-induced crack closure; (b) oxide-induced crack closure; (c) roughness-induced crack closure; (d) fluid-induced crack closure; (e) transformation-induced crack closure; (f) crack deflection; (g) crack-bridging by fibers; (h) crack-bridging by particles. 25

1.11 Definitions of different parameters used to describe transient crack-growth effects following single tensile overloads. 33

1.12 Typical fractography resulting from a high-low-high block loading sequence applied to a 2024-T2 aluminum alloy. [2] 36

1.13 Typical fracture surface due to a block loading in a 2024-T3 aluminum alloy. [2] 37

1.14 Schematic illustration of transient crack growth during constant-amplitude fatigue (A curve), and during variable amplitude loading involving single tensile overloads (C curve) or tensile-compressive overload sequences (B curve). The open circles represent the crack length locations at which each variable amplitude sequence is applied. [2] 38

1.15 Analyses of variable-amplitude fatigue with the Wheeler-retardation model. The overload plastic-zone size, $r_{y(0)}$, is chosen so as to minimize Φ_R [2] 40

1.16 Plastic deformation around a growing crack [2] 42

1.17 (a) Typical MT model and (b) typical CT model 44

1.18 Dugdale (left) and Barenblatt (right) crack models 46

1.19 Schematic representation of the cohesive-zone-model concept; (a) A plate containing a crack; At a potential crack-propagation path e.g., as circled in (b), a cohesive element is inserted, as shown in (c), which follows the specified cohesive-zone model shown in (d) for the normal traction; and (e) a cohesive zone in a Mode-I case [3] 47
1.20 Form of the TSL: a) cubic, from [4], b) constant, from [5], c) exponential, from [6], and d) trilinear, from [7, 8] 51
1.21 Traction and separation law for a hysteretic-cohesive model 53
1.22 Interactions between normal- and shear separations [3] 55

2.1 Schematic of the overload effect. 58
2.2 Compact-tension specimen of Type 316 LN stainless steel with a thickness of 6.35 mm, a notch length of 10.16 mm, and a crack length of 22.86 mm. Diffraction patterns were measured along the crack length with a scattering volume of $2 \times 1 \times 2\ mm^3$ with the 1 mm along the crack length. 60
2.3 Applied tensile loading-unloading sequence. Neutron-strain scanning was performed at each load point (LP) from LP1 through LP7. 62
2.4 In-plane lattice-strain profiles in front of the crack tip at applied loads of 667 N, 3,333 N, and 6,667 N, which correspond to LP1, LP2, and LP3, respectively, in Figure 2.3. 63
2.5 In-plane lattice-strain profiles in front of the crack tip at applied loads of 8,889 N, 6,667 N, and 667 N, which correspond to LP5, LP6, and LP7, respectively, in Figure 2.3. 64

2.6 Comparison between the in-plane lattice strain profile and the plastic-zone size (about $7 \sim 9$ mm) estimated from the changes in the diffraction-peak width at 667 N (LP7 in Figure 2.3). Note that the plastic-zone size calculated using Equation 2.3 is about 7.9 mm. 66

3.1 The load controlled high-cycle fatigue experimental result: crack-growth-rate curve. 75

3.2 Fracture-surface image at different ΔK levels. (a) Fracture-surface image at ΔK of 34.84 $MPa\sqrt{m}$, (b) at ΔK of 35.82 $MPa\sqrt{m}$, (c) at ΔK of 36.34 $MPa\sqrt{m}$, (d) at ΔK of 37.55 $MPa\sqrt{m}$, and (e) at ΔK of 39.29 $MPa\sqrt{m}$. 77

3.3 The comparison between the fatigue-striation spacing and the crack-growth rate at a function of the crack length. 78

3.4 In-plane lattice-strain profiles in front of the crack tip at applied loads of 667 N, 3,333 N, 6,667 N, and 3,333 N, which correspond to LP1, LP2, LP3, and LP4 in Figure 2.3. 79

3.5 Through-thickness lattice-strain profiles in front of the crack tip at applied loads of 667 N, 3,333 N, 6,667 N, and 3,333 N, which correspond to LP1, LP2, LP3, and LP4 in Figure 2.3. 79

3.6 In-plane lattice-strain profiles in front of the crack tip at applied loads of 8,889 N, 6,667 N, and 667 N, which correspond to LP5, LP6, and LP7 in Figure 2.3. 80

3.7 Through-thickness lattice-strain profiles in front of the crack tip at applied loads of 8,889 N, 6,667 N, and 667 N, which correspond to LP5, LP6, and LP7 in Figure 2.3. 81
3.8 Peak-width-change profiles as a function of the distance from the crack tip at applied loads of 667 N, 3,333 N, 6,667 N, and 3,333 N, which correspond to LP1, LP2, LP3, and LP4 in Figure 2.3. 82
3.9 Peak-width-change profiles as a function of the distance from the crack tip at applied loads of 8,889 N, 6,667 N, and 667 N, which correspond to LP5, LP6, and LP7 in Figure 2.3. 82
3.10 Crack-surface displacement and stress distributions along the crack line. [9] 85

4.1 Schematic of a neutron-diffraction experiment 93
4.2 Lattice-strain profiles at in-situ loading of 667 N after the fatigue and overload deformation along the IP direction 95
4.3 The dependence of FWHM on $2\pi/d$ for four types of $< hkl >$ at different distances from the crack tip 98
4.4 Dislocation density as a function of the distance from the crack tip . 99
4.5 Laue patterns obtained at different locations near the crack tip, (a) mapping sketch, (b) Laue pattern at (0.1 mm, 0 mm), (c) Laue pattern at (1 mm, - 0.85 mm), and (d) Laue pattern at (9 mm, - 0.85 mm) . 101

5.1 Elastic-lattice-strain and dislocation-density distributions at the minimum loads immediately before and after the overload, in (a) and (b), respectively. The inset shows the neutron-measurement positions behind and in front of the crack tip. 105
5.2 Elastic strain and plastic strain distributions at the minimum loads immediately before and after the overload, in (a) and (b), respectively 109

6.1 The effect of overload on fatigue-crack propagation. During the fatigue tests, seven specimens were prepared. 113
6.2 The lattice-strain profiles of SP1, SP2, SP3, and SP6 along the transverse direction. 116
6.3 The schematic illustration of the perturbed plastic zone. a_0 is the crack length, and r_c is the plastic-zone size. 117

7.1 The Wheeler model for fatigue retardation [10] 123
7.2 Compact-tension specimen of Type 316 LN stainless steel with a thickness of 6.35 mm, a notch length of 10.16 mm, and a crack length of 22.86 mm. 125
7.3 (a) Fatigue-loading pattern, (b) crack length vs.number of cycles, and (c) crack-growth rate vs. stress-intensity-factor range, ΔK. Six specimens were prepared at different stages during the retardation period. 126
7.4 Measurement positions for the two-dimensional (2-D) strain mapping 130
7.5 Lattice-strain profile for SP1, SP2, SP3, SP4, SP5 and SP6 along the transverse direction. 131

7.6 Lattice-strain profile for SP2 along transverse, longitudinal, and normal directions. 133
7.7 Stress distributions as a function of the distance from the crack tip for SP1 and SP2 134
7.8 Stress distributions as a function of the distance from the crack tip for SP4 and SP6 135
7.9 (a), (b), and (c) strain contours for SP1, SP2, and SP6, respectively . 137

Chapter 1

Literature Review

1.1 Background of the Chosen Material

This research will be conducted on compact-tension (CT) specimens made of a Type 316 low-carbon nitrogen-added (LN) stainless steel (SS). The basic composition of the 316 LN SS was listed in Table 1.1.

As a candidate target-container material of the Spallation Neutron Source (SNS) being designed and constructed at the Oak Ridge National Laboratory (Oak Ridge, TN), the Type 316 LN SS is required to have good fatigue resistance under severe

Table 1.1: Chemical composition of Type 316 low-carbon, nitrogen-added (LN) stainless steel (SS) (wt.%, weight percent)

Element	C	Mn	P	S	Si	Ni
wt.%	0.009	1.75	0.029	0.002	0.39	10.2
Element	Cr	Mo	Co	Cu	N	Fe
wt.%	16.31	2.07	0.16	0.23	0.11	Bal.

working environments, in terms of the radiation effects, stress, and compatibility with mercury. The material was melted by the electric-furnace, argon-oxygen decarburization process (EF/AOD) and met the American Society of Mechanical Engineers (ASME)NCA 3800 QSC-245 specification. The material was annealed at 1038°C for one hour [11–17]. The understanding of the main effects of alloying elements in 316 LN SS is needed.

- Carbon (C)
    1. A strong austenite former.
    2. Added to some high-strength alloys for hardening and strengthening effects.
    3. Adversely affecting the weld-metal corrosion resistance and toughness at low temperatures.
- Chromium (Cr)
    1. A ferrite and carbide former.
    2. A primary contributor to scaling and corrosion resistances.
    3. In the stainless steels, this element having little or no influence on the high-temperature strength and creep strength.
- Molybdenum (Mo)
    1. A ferrite and carbide former.
    2. Used to improve the high-temperature strength and creep resistance.

3. Employed to improve the general corrosion resistance of steels in non-oxidizing media, and the resistance to pitting corrosion in all media.

- Nitrogen (N)

1. A strong austenite former.
2. Used to minimize grains grown in high-chromium steels at high temperatures.
3. Adversely affecting the weld metal toughness at cryogenic temperatures.
4. Raising strength.

- Nickel (Ni)

1. An austenite former.
2. Used to improve the general corrosion resistance against non-oxidizing liquids.
3. Sometimes added in small amounts to improve the mechanical properties.
4. Generally improving the weld-metal toughness.

The Type 316 LN has a similar chemical composition to the 316 L stainless steel. The usual 316L austenitic stainless steel is fully austenitic after the solution heat-treatment but has poor mechanical properties. It has already been shown that nitrogen alloying clearly improves the monotonic and cyclic behavior of the 316 L stainless steel at room and high temperatures [18]. According to the phase diagram, nitrogen is an austenite stabilizer. The influence of nitrogen on stabilizing

Table 1.2: Mechanical properties of Type 316 stainless steels at 27 and -196 °C [19]

Materials	Test Temperature (°C)	σ_y (MPa)	σ_u (MPa)
316 L	27	262	574
	-196	402	1156
316 LN	27	328	697
	-196	902	1415

the austenite may change the presence of strains at low temperatures, because the mechanisms of the martensitic transformation may vary with the deformation. The work reported by Vogt *et al.* examines the effect of nitrogen and temperature on the fatigue behavior of a 316 L austenitic stainless steel [19]. A correlation between the macroscopic behavior, and the microstructure is developed for the low-cycle fatigue (LCF) and fatigue-crack-propagation behavior. Two austenitic stainless steels (316 L and 316 LN) were studied, whose chemical compositions differ significantly in their nitrogen contents. Table 1.2 summarizes the different tensile characteristics (the yield strength, σ_y, ultimate tensile strength, σ_u, total elongation, A, and reduction in area, S) deduced from tests performed at 27 and -196°C [19]. It shows that nitrogen increases the fatigue strength at 27 and -196°C. Nitrogen favors the planar slip by reducing the tendency for the cross slip and avoiding a three-dimensional cellular structure. In the 316 LN alloy, the stacking-fault energy (SFE) that is responsible for the planar slip is reduced by low temperatures and by the effect of nitrogen at low temperatures. Note that a lower SFE favors the planar slip instead of the cross slip. The result of the fatigue-crack-growth rate (FCGR) may be interpreted as a consequence of the cyclic hardening due to a combination of the interstitial-solute

strengthening, strain-induced phase transformation, and a decrease in the temperature. Lowering the temperature from 27 to -196°C for both 316 L and 316 LN materials decreases SFE, and hardens the materials, which produces a decrease of the crack-opening displacement (COD), resulting in a decrease of fatigue-crack-growth rates. Since the decrease in the SFE of 316 LN is even greater with the presence of interstitial solutes of nitrogen, the fatigue resistance of 316 LN is greater than 316 L SS [19].

1.2 Developments of Fracture Mechanics

In 1913, Inglis [20] proposed the concept of stress concentrations at geometrical discontinuities, thus providing an explanation for why fractures emanate from cracks, holes, or defects. In 1920, Griffith [21] proposed his hypothesis about the energy exchanges that take place during the fracture and derived the concept of a critical crack size necessary for a brittle fracture. In 1939, Westergaard [22] published the results of his analysis demonstrating that the stresses at the tips of cracks in elastic bodies varied as a function of $1/\sqrt{r}$, where r is the distance from the crack tip. In 1948, Irwin [23] and Orowan [24] proposed modifications to account for the plastic energy. In 1957, Irwin [25] used a technique and proposed a more complete description of the crack-tip stress distribution. In mid-1950s, aircraft and ship failures facilitated the U.S. Navy to accept the importance of the fracture-mechanics research. More fracture concepts, such as fracture toughness, K_{IR}, and crack-tip-opening displacement, CTOD, become widely accepted. In 1960, Paris and co-workers [26] first proposed

the relationship between the fatigue-crack-growth rate and the cyclic-stress-intensity-factor-range parameter. As the nuclear industry becomes prominent in nineteen sixties, ductile steels were used. The elastic-plastic-fracture theory had to be extended to include fracture mechanisms. In 1968, three papers of the considerable significance to the development of the elastic-plastic fracture mechanics appeared. Rice [27] idealized the plastic deformation as a nonlinear phenomenon for mathematical purposes and was able to generalize the energy-release rate for such a material. In 1972, the results of the first study to predict the initiation of fracture under elastic-plastic conditions were published by Begley and Landes [28, 29]. In subsequent years, much process occurred in the development of test methods, making the elastic-plastic fracture mechanics a viable engineering tool for the structural-integrity analysis. In the early of mid-seventies, creep conditions had already begun to be introduced into the fracture mechanics. Saxena [30] defined the C_t parameter, which can be used to characterize the creep-crack-growth behavior under conditions ranging from the small-scale to extensive creep. Although much progress has occurred in the fracture mechanics over the past 40 years, it still remains an active field of research [31].

1.3 Basic Concepts

There are three distinct modes in which a crack body can be loaded, as shown in Figure 1.1 where the Mode-I crack-opening mode is the one that we are interested in, because most fracture in metallic components occur under the Mode-I condition. In Mode I , the crack separates symmetrically. The stress and displacements in a

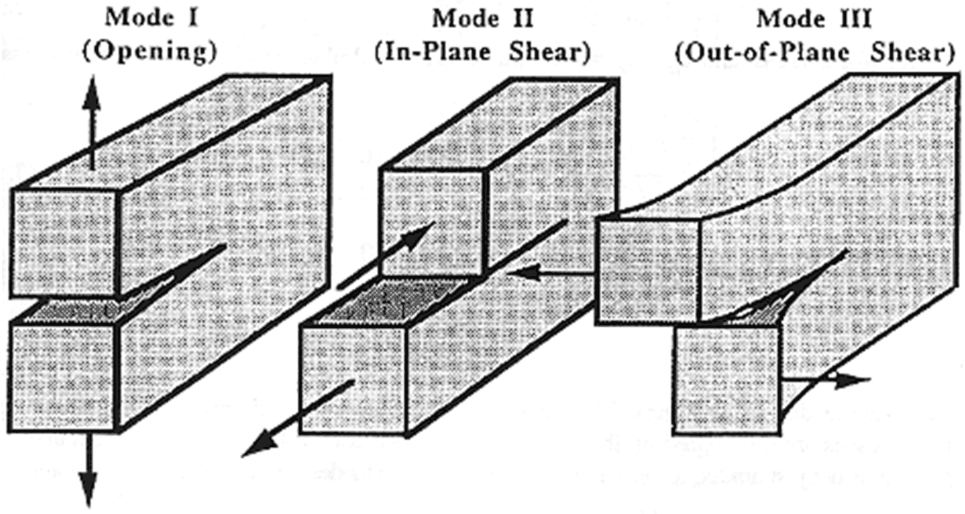


Figure 1.1: The three modes of loading a cracked body.

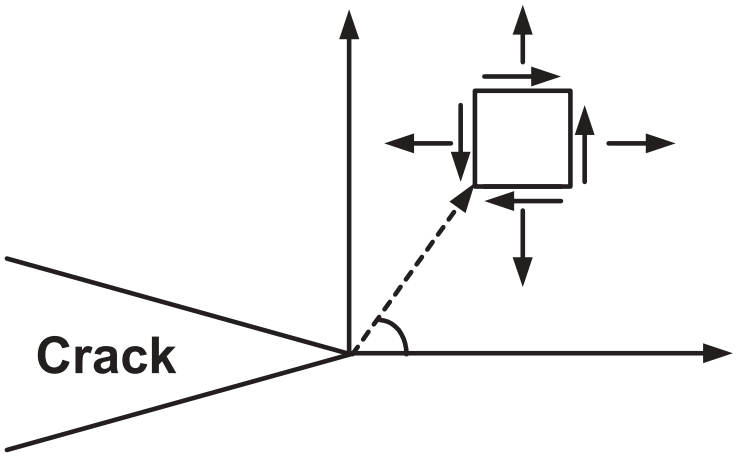


Figure 1.2: The crack-tip coordinate system and the stresses acting on an element ahead of the crack tip.

region near the crack tip are given by Equation 1.1 [1].

$$\begin{aligned} \sigma_x &= \tfrac{K}{\sqrt{2\pi r}} \left[\cos\tfrac{\theta}{2}\left(1 - \sin\tfrac{\theta}{2}\sin\tfrac{3\theta}{2}\right)\right] \\ \sigma_y &= \tfrac{K}{\sqrt{2\pi r}} \left[\cos\tfrac{\theta}{2}\left(1 + \sin\tfrac{\theta}{2}\sin\tfrac{3\theta}{2}\right)\right] \\ \tau_{xy} &= \tfrac{K}{\sqrt{2\pi r}} \left(\sin\tfrac{\theta}{2}\cos\tfrac{\theta}{2}\cos\tfrac{3\theta}{2}\right) \end{aligned} \tag{1.1}$$

see Figure 1.2 where K is the stress-intensity factor, r is the distance from the origin, and θ is the angle to the x axis.

The stress-intensity factor, K, represents the amplitude of the crack-tip-stress singularity and is dependent on the body geometry, crack size, load level, and loading configuration. For compact-tension specimens, the expressions for estimating K is,

$$K_{\max} = \frac{P_{\max}(2+\alpha)}{B\sqrt{W}(1-\alpha)^{3/2}}(0.886 + 4.64\alpha - 13.32\alpha^2 + 14.72\alpha^3 - 5.6\alpha^4) \tag{1.2}$$

where K is the stress-intensity factor, α is the function of total crack length, B is the thickness of the specimen, and W is the width of the specimen.

Irwin made a simple estimate of the plastic-zone size along $\theta = 0$ for elastic, perfectly-plastic materials. The simplest estimate can be made by substituting $\theta = 0$ in Equation 1.1 and solving for a distance, r_y, at which $\sigma_y = \sigma_0$. This calculation leads to Equation 1.3.

$$r_p = 2r_y = \frac{1}{\pi}\left(\frac{K}{\sigma_0}\right)^2 \tag{1.3}$$

where r_p is the plastic-zone size, and σ_0 is the yield stress

Figure 1.3 [1] shows the distance, r_y, schematically. This estimate of the plastic zone is incorrect because it is based on the elastic-stress distribution. The elastic-plastic stress distribution is also shown schematically in Figure 1.3. The plastic-zone boundary is located at r_p, according to this distribution. To satisfy the force equilibrium in the y-direction, the areas under the elastic and elastic-plastic stress distributions must be the same. Equation 1.3 has been derived for a nonhardening material. For hardening materials, which follow the Ramberg-Osgood relationship:

$$r_p = \frac{m-1}{m+1}\frac{1}{\pi}\left(\frac{K}{\sigma_0}\right)^2 \tag{1.4}$$

m is the inverse of the strain-hardening exponent, which was a material constant derived from the regression of the stress-strain curve, r, is the plastic zone size, and σ_0 is the yield stress.

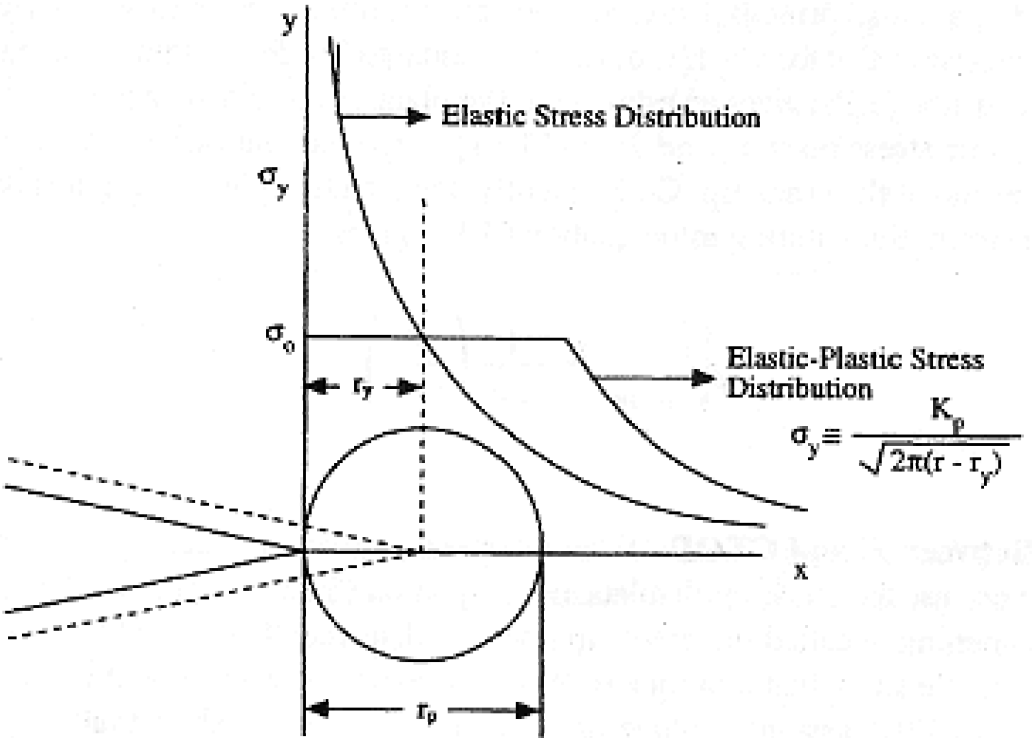


Figure 1.3: Elastic and elastic-plastic crack-tip-stress distributions in front of the crack tip and the plastic-zone sizes, r_y and r_p. [1]

1.4 Fatigue Mechanisms

The fatigue life is composed of both the crack-initiation and crack-growth stages. The useful fatigue life is, then, the time or the number of cycles to grow a dominant flaw of the initial size to a critical dimension, at which the catastrophic failure is expected. To predict the fatigue lives of these components for design and maintenance purposes, it is necessary to know the rates at which these flaws/cracks grow. The measurement of the crack-growth data for different combinations of the applied stress, crack length, and geometrical conditions of the cracked structure, and the mechanisms, which control the crack-growth rates under different conditions of the mean stress, test frequency, and environment, are research topics of scientific and practical interest. The crack-growth-rate data are generated through testing in laboratory. The crack-growth rate is expressed in terms of the crack-length increment per cycle or unit time, da/dN or da/dt, respectively. Figure 1.4 [2] illustrates a typical fatigue-crack-growth curve under a constant load range. The crack length increases with increasing the number of loading cycles. The fatigue-crack-growth rate is determined from such curves by graphical procedures or by computations. From these methods, the crack-growth rates resulting from a given cyclic load are $(da/dN)_{a_i}$ and $(da/dN)_{a_j}$ when the crack is of lengths, a_i and a_j, respectively. When the applied load range is held constant, the crack-growth rate most often increases with increasing the number of fatigue cycles. This trend is generally the case, though not always. For the same crack length, the crack-growth rate generally increases with increasing the applied load range, as indicated in Figure. 1.4. With the rapid development of the fracture mechanics, more reliable methods became available in the 1960s. Paris *et al.* [26, 32]

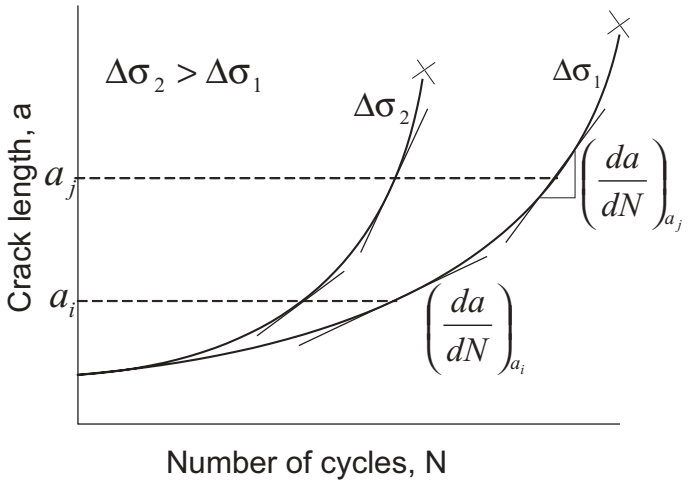


Figure 1.4: Typical fatigue-crack-growth curves under a constant load range. [2]

postulated that the controlling factor in the fatigue-crack-growth process is the stress-intensity-factor range,

$$\Delta K = K_{max.} - K_{min.} \tag{1.5}$$

$K_{max.}$ and $K_{min.}$ are the maximum and minimum stress-intensity factors, respectively, during a fatigue cycle. The stress-intensity-factor range, ΔK, is a function of the load range and crack length. Its particular form depends on the specimen geometry. For an edge-cracked specimen,

$$\begin{aligned} K_{\max.} &= Y\sigma_{\max.}\sqrt{a} \\ K_{\min.} &= Y\sigma_{\min.}\sqrt{a} \\ \Delta K &= Y\Delta\sigma\sqrt{a} \\ \Delta\sigma &= \sigma_{\max.} - \sigma_{\min.} \end{aligned} \tag{1.6}$$

where Y is a geometrical factor related to the ratio of the crack length, a, to the width of the specimen, W, and $\sigma_{max.}$ and $\sigma_{min.}$ are the maximum and minimum stresses in a fatigue cycle, respectively. Paris *et al.* [26, 32] plotted the values of da/dN versus those of ΔK for the same crack length, a, and demonstrated that there exists a relation of the form

$$\frac{da}{dN} = C\Delta K^m \tag{1.7}$$

where C and m are scaling constants that are dependent on material variables, environments, cyclic frequencies, temperatures, and load ratios, R, which is defined

as

$$R = \frac{\sigma_{min.}}{\sigma_{max.}} = \frac{K_{min.}}{K_{max.}} \tag{1.8}$$

This simple relation (Equation 1.7) is commonly called the *Paris-power law*. Although Equation 1.7 is empirical, it has remained one of the most used expressions in the fatigue-crack-growth analysis for a vast spectrum of materials and test conditions.

It is often desirable to estimate the useful component life for the purposes of design and failure analyze. The number of fatigue cycles to failure can be computed, using the Paris-power law, Equation 1.7. Assume that the initial flaw size is a_0 and the final critical crack size, a_f, and that Y remains constant as the crack grows. Assume also $\Delta K = Y\Delta\sigma\sqrt{a}$. Integrating Equation 1.7 results in

$$CY^m(\Delta\sigma)^m \int_0^{N_f} dN = \int_{a_0}^{a_f} \frac{da}{a^{m/2}} \tag{1.9}$$

The fatigue life is, thus, given by

$$N_f = \frac{2}{(m-2)CY^m(\Delta\sigma)^m}\left[\frac{1}{(a_0)^{(m-2)/2}} - \frac{1}{(a_f)^{(m-2)/2}}\right] \tag{1.10}$$

for $m \neq 2$ and

$$N_f = \frac{1}{CY^2(\Delta\sigma)^2} \ln\frac{a_f}{a_0} \tag{1.11}$$

for $m = 2$. The assumption that Y remains constant is generally not true. Therefore, the integration is usually performed numerically. It is easily seen from Equation 1.10 that when $a_0 \ll a_f$ (which is generally true for ductile alloys), the fatigue life, N_f,

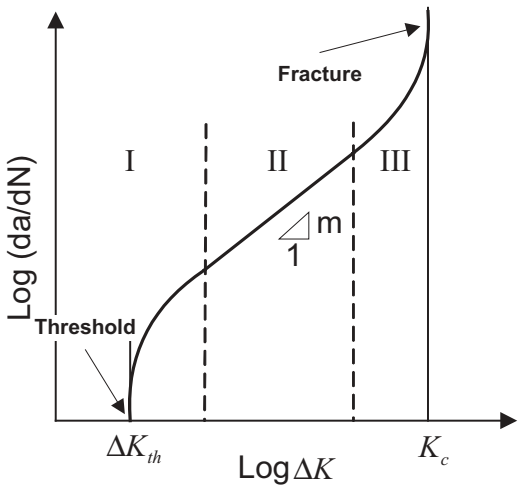


Figure 1.5: Typical fatigue-crack-growth diagram showing three different regimes.

is not sensitive to the final crack length, a_f, but is strongly dependent on the choice of a_0.

Many experimental data show a good agreement with the Paris-power-law relationship, Equation 1.7, under a proper choice of the constants, C and m. However, this observation is true only at a particular range of crack-growth rates. At the extreme values of ΔK, both below and above those of the Paris regime, the Paris-power law does not hold. The whole $\log(da/dN)$ versus $\log(\Delta K)$ curve assumes a sigmoidal shape, defining three distinct regimes, as shown in Figure 1.5. In Regime I, there exists a threshold-stress-intensity-factor range, ΔK_{th}, such that at $\Delta K < \Delta K_{th}$, the crack practically does not grow. Above the threshold, there is a steep increase in da/dN with increasing ΔK. The Paris-power law applies in Regime II. In Regime III, the $K_{max.}$ value approaches that of the fracture toughness, K_c. The crack-growth rates increase rapidly, causing catastrophic failures.

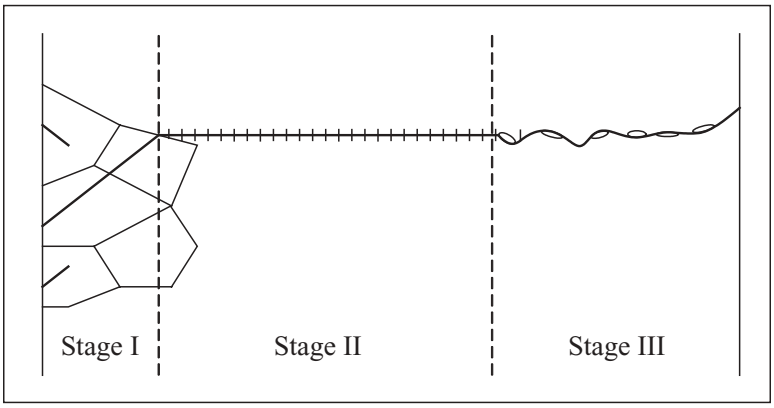


Figure 1.6: Schematic of fatigue-crack growth across a specimen section indicating three stages of fatigue failures. (After Laird [33].)

1.4.1 Fatigue-Failure Mechanisms

The fatigue-failure process begins with the accumulation of damages at localized regions, which leads to the nucleation of cracks and their subsequent propagation. When one of the cracks has grown to such an extent that the remaining net-section is insufficient to carry the applied load, a sudden fracture results. In general, the fatigue cracks nucleate at the free surface, and the crack growth occurs in three stages, as shown schematically in Figure 1.6 [33]. The Stage-I crack-propagation region is an extension of the initiation process (the initiated crack length here is of about 10 μm) and the crack grows in a crack-tip shear plane oriented at approximately 45° to the stress axis. The extent of this stage is usually a few grains. The Stage-II growth is controlled by the continuum response of the materials and is perpendicular to the applied stress. When the crack-tip deformation becomes large enough, the local static fracture (*i.e.*, hole growth) contributes to the crack advance until the final failure, which is in the stage-III crack-growth region. Stages I, II, and III are characterized

by the featureless, striated, and microvoid-coalescence regimes, respectively. The fractional area of the fracture surface for the three stages depends on the applied strain level. When the strain level is high, the failure life will be small, and the striated regime (stages II) covers almost the entire fracture surface. In contrast, when the strain level is small, the failure life will be long, and the featureless regime (stage I) begins to dominate. Only for very high strain-level tests will stage III occupy a significant area. In the total-life approach to fatigue, both the crack nucleation and the three crack-growth stages are involved. In the fatigue-crack-growth testing of the fracture-mechanics approach, usually only the last two stages of crack propagation will be present.

1.4.2 Fatigue-Crack-Initiation Mechanisms

It is generally agreed that the persistent slip bands (PSBs) are major nucleation sites for cracks in metals and alloys of high purity. The PSBs are thin lamellae where the plastic deformation is mainly concentrated during fatigue cycling. The plastic strain in the PSB lamellae is at least an order of magnitude higher than that in the matrix [34]. The cracks tend to form at the deep narrow intrusion, and the interface between the PSB and matrix, which is a plane of discontinuity and across which there are steep gradients in the density and distribution of dislocations. As schematically shown in Figure 1.7 [35], the formation of PSBs leads to surface roughening, which is manifested as microscopic *hills* and *valleys*, commonly referred to as *extrusions* and *intrusions*. The intrusions function as micronotches, and the effect of the stress concentration at the root of the intrusions promotes the additional

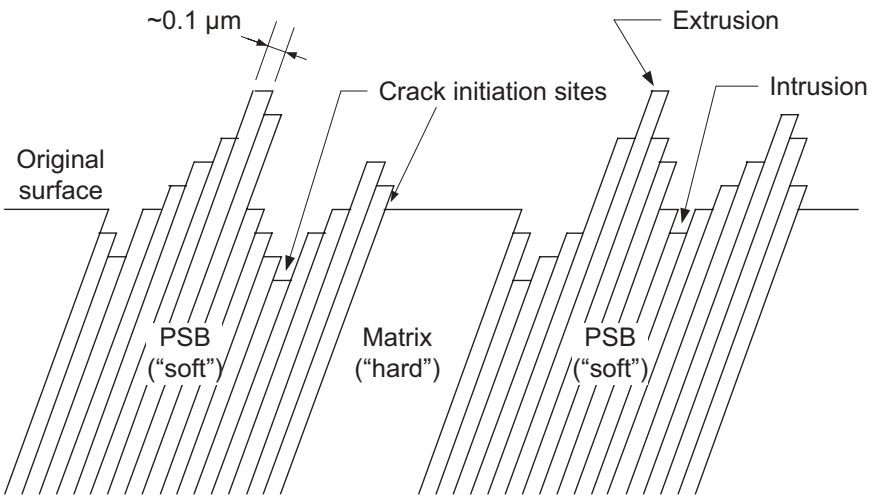


Figure 1.7: Schematic shows the roughening of surfaces due to the formation of persistent slip bands (PSBs). (After Ellyin [35].)

slip and fatigue-crack nucleation. The crack initiation in commercial alloys is very complicated. It could happen at voids, slag, or gas entrapments, inclusions, dents, scratches, forging laps and folds, macroscopic stress concentrations, as well as regions of microstructural and chemical non-uniformities [36–38]. In metals and alloys of high purity, cracks usually initiate at the free surface. In commercial alloys, it is common to see that fatigue cracks nucleate at both near-surface and interior locations. The exact initiation sites are often specific to the alloy system considered.

1.4.3 Fatigue-Crack-Growth Mechanisms

As mentioned earlier, the direction of the stage-I crack growth (see Fig. 1.6) is oriented at about 45° to the stress axis. The direction of the stage-II fatigue-crack growth is perpendicular to the applied stress. The stage-II growth is due to some irreversibility in the crack-tip flow within each cycle. A mechanism for the stage-II growth is shown in Figure 1.8 [39]. There are other mechanisms, which are not essentially different. Because of the high stress concentration, the plastic deformation is present at the crack tip even at very low loads. The plastic deformation means slip (due to shear stresses) of atomic planes (Fig. 1.8, stage B). Slip also occurs on the complementary planes, and the crack widens and becomes blunted (Fig. 1.8, stages B-D). Upon unloading (or compressive loading), the slip direction in the end zones is reversed, and the crack faces are crushed together to form a resharpened crack tip (Fig. 1.8, stage E). Theoretically, the whole slip process could be reversed so that the end result after unloading would again be as Stage A. However, because of the

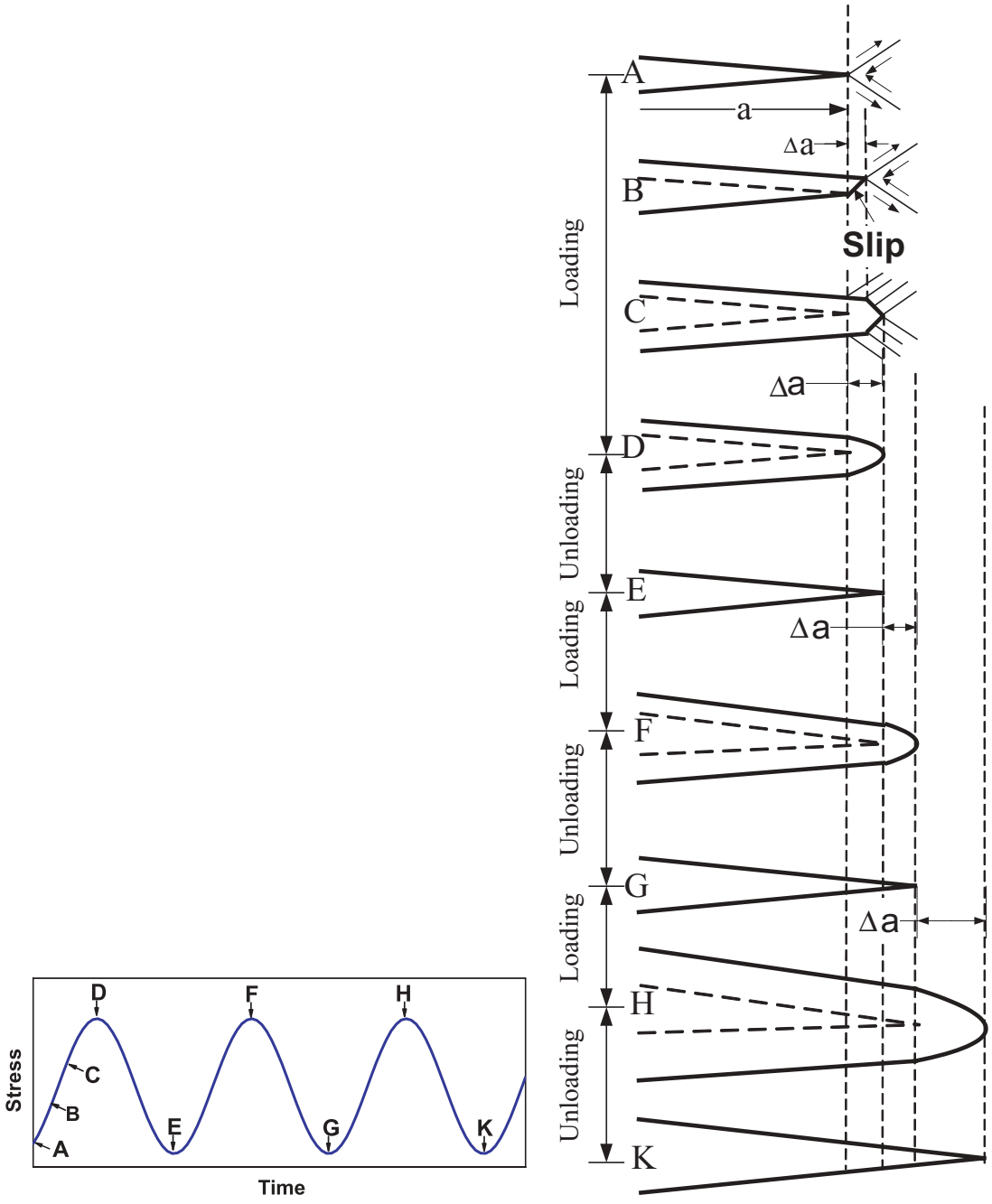


Figure 1.8: One of the various possible mechanisms of fatigue-crack growth. (After Broek [39].)

oxidation of the freshly exposed material along the slip steps, and the general disorder due to the slip, the process is irreversible in practice; and the crack extension, Δa, remains the same after each cycle. The resharpened crack (stage E) is, then, advanced and becomes blunted in the next stress cycle, and so on (stages F-K).

The crack growth per cycle is generally on the order of $10^{-7} - 10^{-3}$ mm ($10^{-8} - 10^{-4}$ inches). If the cycle number is $10^4 - 10^8$, the crack will grow by 25.4 mm (one inch). The repeated blunting and sharpening results in marks on the crack surface, which are visible at high magnifications in an electron microscope. These marks, commonly termed fatigue striations, represent the successive positions of the crack front.

The Stage-III fatigue-crack growth is the final fracture. It is unstable and very fast. It occurs by either cleavage or ductile rupture. Cleavage takes place along the low-index atomic planes, leading to a fracture surface of many flat and bright facets. The majority of engineering materials, however, factures by the ductile rupture. All engineering materials contain particles and inclusions. These particles are usually complex compounds of the alloying elements, which are added to improve the alloy's strength, castability, or machinability. The ductile rupture process, which is schematically illustrated in Figure 1.9 [39], is related to these particles and inclusions. Firstly, the large particles are broken or separated from the matrix, forming large holes. Secondly, concentrated slip occurs in channels connecting the cleaved large particles because of the stress concentration and the less load-bearing materials. The slip results in the separation of the small particles from the matrix, forming myriads of small holes. The final and quick separation happens along the small holes inside

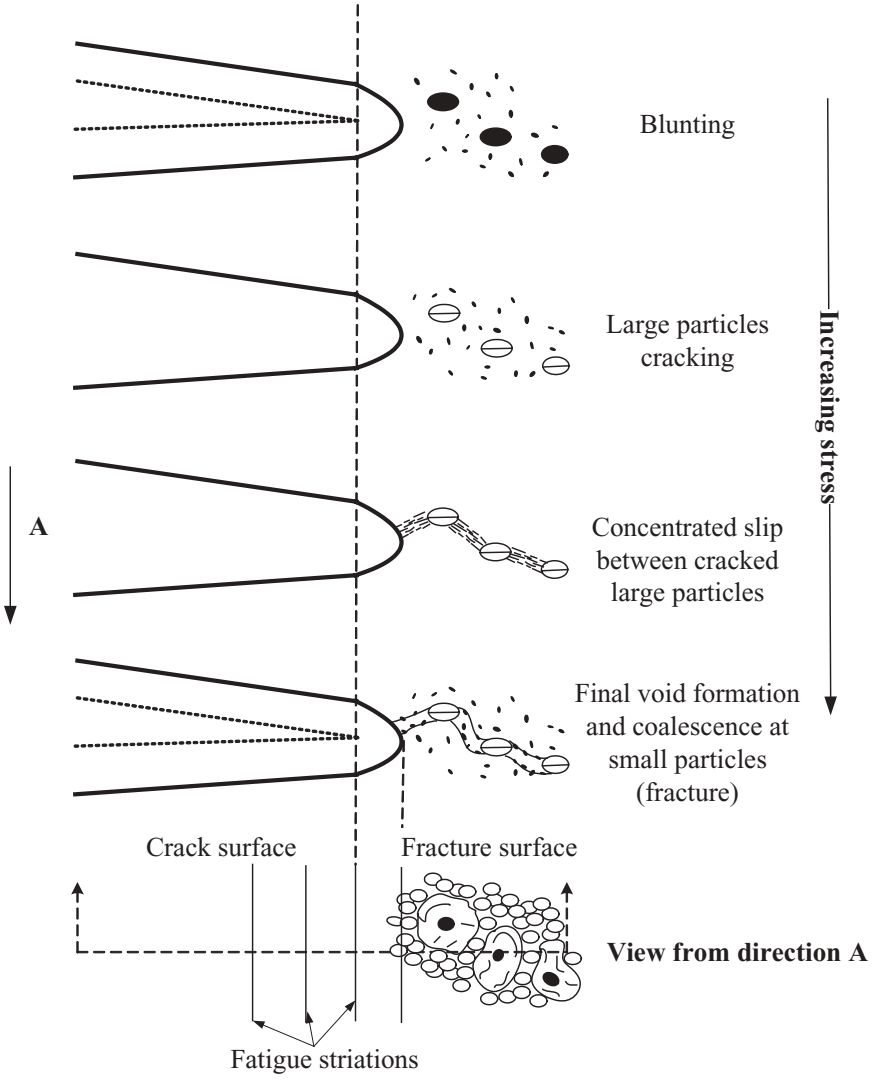


Figure 1.9: Schematic of ductile rupture showing four stages. Bottom: the fracture surface illustrates dimples formed by small and large particles. (After Broek [39].)

the channels. Thus, the large holes from the large particles and the small holes from the small particles are present on the fracture surface. These holes are visible with the electron microscopy, and are commonly termed *dimples*.

1.5 Overloading Effects

Structural components used in practical applications are subjected to variable amplitude fatigue loads. It is a challenge for engineers and scientists that the more realistic situations involving varying amplitudes of cyclic stresses or strains. This problem is further compounded by different effects induced by variable-amplitude -fatigue loads on the resistance of a material to crack initiation and crack growth. Traditional models based on the damage accumulation concepts imply that the total fatigue life of a component is decreased by the application of periodic overloads. However, an experimental observation on variable-amplitude fatigue-crack growth in a wide variety of metallic and non-metallic materials have established that the application of a periodic overload can significantly decelerate the rate of fatigue fractures. Elber [40, 41] first rationalized the possibility that a fatigue crack can close even at a far-field tensile load on the basis of experimental observations. Elber argued that a zone of the residual compressive deformation is left in the wake of a fatigue-crack tip. The attendant reduction in the crack-opening displacement gives rise to a premature contact between the faces of the crack and causes a reduction in the apparent 'driving force' for fatigue-crack advancement.

While concepts of fatigue-crack retardation were developed over the years mainly in the contact of fatigue in conventional metals, the expanding interest in the fatigue of the advanced metallic system, nonmetallic materials and composites has led to a surge in the research on several other mechanisms. These mechanisms include: the plasticity-induced crack closure; oxide-induced crack closure; roughness-induced crack closure; fluid-induced crack closure; transformation-induced crack closure; crack deflection; crack-bridging by fibers; and crack-bridging by particles. Figure 1.10 [2] schematically illustrates the various mechanisms by which the growth of a fatigue crack can be retarded. It is noted that the evolution of different crack closure and retardation mechanisms during both constant-amplitude and variable-amplitude fatigue is a process that can not be quantified accurately. These processes can be strongly influenced by even small variations in the path of the crack, environmental conditions, loading conditions, and testing methods. It is impossible to identify the individual contributions to the overall crack-growth rates from each of these retardation or shielding mechanisms. It is not surprising that there exists a considerate controversy and difference of the opinion on the applicability and significance of different retardation mechanisms to the fatigue-crack propagation

1.5.1 Plasticity-Induced Crack Closure

Experiments done by Elber [40, 41] suggested that crack-growth rates are not only influenced by the conditions ahead of the crack tip, but also by the nature of the crack-face contact behind the crack tip. Since the conditions extant in the wake of the crack tip are a result of such factors as the history of loading, the length of the crack

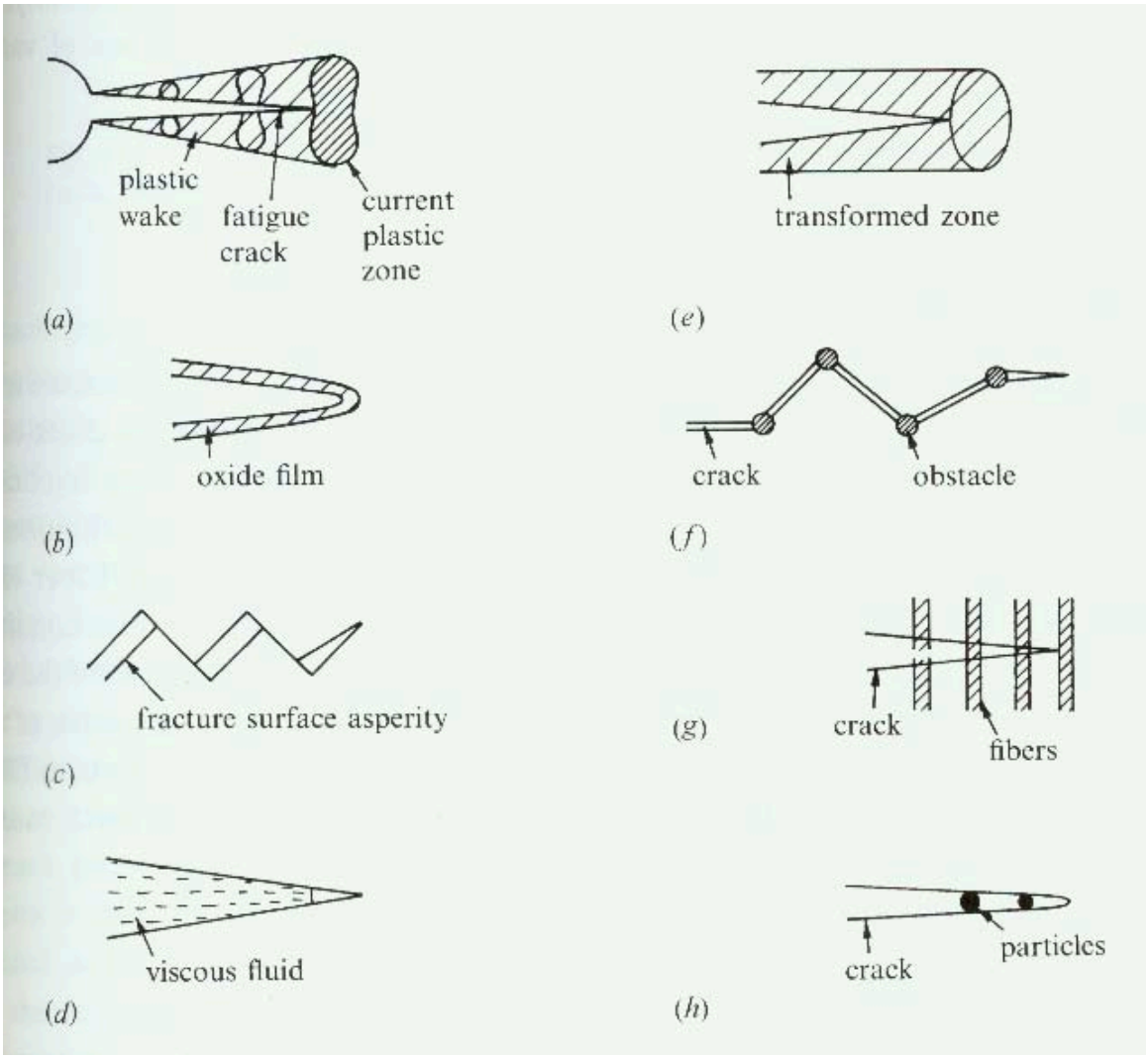


Figure 1.10: 1. A schematic illustration of the mechanisms, which promote the retardation of fatigue-crack growth in constant-amplitude fatigue. (a) plasticity-induced crack closure; (b) oxide-induced crack closure; (c) roughness-induced crack closure; (d) fluid-induced crack closure; (e) transformation-induced crack closure; (f) crack deflection; (g) crack-bridging by fibers; and (h) crack-bridging by particles.

and the stress state, this work also brought to light the very dependence of the crack growth rates on the prior history. From the load (stress) vs. displacement and stress intensity, K, vs. displacement plots, crack closure can be investigated. The fully open crack, partially open crack, and fully closed crack can be exhibited from these plots. In the context of the crack-closure measurements, it should be noted that: Since the crack closes gradually during a reduction of the stress-intensity factor, there is no unique definition for the closure stress-intensity factor. An averaged closure stress intensity factor, which is the mean value of the stress-intensity factors corresponding to the points of complete opening and complete closure, is used. Budiansky and Hutchinson [42] applied the Dugdale-Barenblatt strip-yield mode to this plasticity-induced crack-closure problem and showed that the residual stretch in the plastic wake causes the crack faces to close at a positive remote stress. Although quantitative predictions from the model do not agree with the experimental data, this model is useful for demonstrating qualitatively the effect of plasticity on crack closure. Several investigators have studied the plasticity-induced closure with finite-element (FE) analyses. One of the earliest FE models of the plasticity-induced crack closure under the plane-stress condition was published by Ohji, Ogura, and Yoshiji [42]. Their results indicated that the strain amplitude in the vicinity of the crack tip scaled with the effective stress intensity factor $\triangle K_{eff}$. In a parallel study, Newman [43] also performed two-dimensional FE analyses for the plan stress using the incremental theory of plasticity. The predictions of the dependence of crack closure on the R ratio were found to be consistent with the experimental observations. It seems to be

consistent among the FE results in that they all indicate a markedly reduced level of crack closure in the plane strain than in the plane stress.

1.5.2 Roughness-Induced Closure

The roughness-induced closure is influenced by the microstructure. Although a fatigue crack propagates in pure crack-opening model conditions on a global scale, crack deflections due to the microstructural heterogeneity can lead to mixed-mode conditions on the microscopic level. These displacements cause a mismatch between upper and lower crack faces, which, in turn, results in a positive closure load. Coarse-grain materials usually produce a higher degree of surface roughness in fatigue, and corresponding higher closure loads [44]. It has been traditionally regarded that finer-grained materials and wavy-slip deformation modes generally led to an improved resistance to the fatigue fracture. However, in many alloy systems, coarser-grained materials and enhanced planar-slip deformation modes give rise to a superior fatigue-crack-growth threshold. At the lower R ratio, where closure effects are pronounced, the coarse-grained materials have a higher threshold-stress-intensity-factor range, $\triangle K_{th}$, due to a higher closure load that is caused by greater surface roughness.

1.5.3 Oxide-Induced Closure

This mechanism is usually associated with an aggressive environment. Oxide debris or other corrosion products become wedged between crack faces. During the propagation of the fatigue crack, the presence of a moist atmosphere leads to the oxidation

of the freshly formed fracture surfaces. At low amplitudes of the cyclic crack-tip-opening displacement, at near-threshold levels and low R ratios, the possibility of the repeated crack-face contact during tensile fatigue is enhanced as a consequence of the locally mixed-mode crack opening, the microscopic roughness of the fracture surfaces, and some plasticity-induced closure. Many researchers [45–48] made references to the possibility of crack closure due to the fracture-surface oxidation during fatigue at both ambient and elevated temperatures. Suresh et. al. [48] reported the first quantification of the influence of oxide layers formed within the fatigue cracks on the threshold fatigue behavior in ferritic-pearlitic, bainitic, and martensitic steels. They also estimated the thickness of the oxide layers over the fracture surface covering a wide range of the crack growth rates and found the oxide thickness within the fatigue crack to be comparable to the scale of the crack-tip-opening displacement near the threshold. The oxide-induced crack closure is also known to have a decisive effect on the near-threshold crack-propagation response of copper [49], and nickel-base superalloys [50] fatigued in oxidizing media.

1.5.4 Phase-Transformation-Induced Crack Closure

A stress-induced transformation at the tip of a growing crack can result in a process zone wake. Residual stresses in the transformed zone can lead to crack closure. This phenomenon is commonly referred to as the transformation-induced plasticity (TRIP) effect. As the enlarged material in the transformation zone is left behind the advancing fatigue-crack tip, a net reduction in the crack-opening-displacement ensues. Pineau and Pelloux [51] and Hornbogen [52] studied the fatigue-crack growth

in metastale austenitic stainless steels and showed that the strain-induced matensitic transformation generally resulted in reduced crack-growth rates at low to mid-ΔK levels. The crack-propagation rates increased in the following sequence of microstructural variations: metastable austenite $\longrightarrow$ stable austenite $\longrightarrow$ martensite of the same composition. The experiments suggest that such transformation-induced closure is promoted by phase changes, which lead to a dilation of the region undergoing the transformation, and by conditions, which promote phase changes, viz., higher strain rates, lower temperatures, and increased metastability of the transforming phase. The transformation-induced closure is strongly influenced by the size and geometry of the test specimen and of the fatigue crack.

1.5.5 Fatigue-Crack Deflection

Methods make the path of a crack periodically deflected from its nominal growth plane, which can offer one possible way of enhancing the apparent resistance to fatigue-crack growth [53, 54]. Crack deflection viewed as a mechanism for causing obstacles in the path of the crack may cause a beneficial resistance to crack growth by tilting or twisting the crack front. In order to improve the resistance of engineering materials to fatigue-crack growth by the crack-deflection processes, an understanding of the following issues are necessary. How to design the micro- and macrostructure of a material? How does the structure affect the fatigue-crack path? What is the sole effect of the crack path on the overall resistance to fatigue-crack growth?

1.5.6 Retardation

Crack closure is one of the major causes for the retardation effects. It is instructive to examine the magnitude of the crack closure and its relative role in the crack-growth process. Crack closure has the influence on fatigue-crack-growth rates, and is strongly dictated by microstructural and environmental factors, and mechanical-loading parameters. There are some basic characteristics and trends, which are common to various types of crack closure and to a wide variety of materials.

- Crack closure is generally more dominant at lower $\triangle K$ levels and lower R ratios because of the smaller minimum crack-opening displacement.

- For the plasticity-induced or transformation-induced crack closure, the possibility of the enhanced crack closure may increase as a result of the larger crack wake sketch or transformed zone size at high $\triangle K$ levels and R ratios.

- There is a characteristic size scale associated with each closure process, such as the height of the residual plastic-crack wake for the plasticity-induced crack closure, the thickness of the oxide layer for the oxide-induced crack closure, the height of the fracture-surface asperities for crack closure due to the roughness, and the height of the transformation zone for closure arising from phase changes. When the size of this characteristic "closure dimension" becomes comparable to the crack-opening displacement, a premature crack-face contact has a marked effect on the rate of the fatigue-crack growth.

- As a fatigue crack emerges from a free surface or a stress concentration, the extent of crack closure generally increases with an increase in the crack length

up to a saturation crack length, beyond which the closure is normally crack length-independent.

- Closure is produced by mechanisms, such as the plastic deformation or phase transformations, as well as phenomena, which occur in the wake of the fatigue crack tip, such as the fracture-surface oxidation.

- No unique conclusion can be reached about the effect of the stress state on the extent of crack closure.

There are a number of complex issues, which pose a formidable challenge to experimental and theoretical attempts aimed at quantifying the effect of crack closure on fatigue behavior in engineering materials.

- Crack closure is often very specific to the conditions of the experiment, and its magnitude is influenced by the effects of material microstructure, test environments, and stress states.

- Even small fluctuations in the microstructural path of crack advance can cause large fluctuations in crack-propagation rates, especially near the fatigue threshold where the crack-opening displacements are small.

- High values of crack closure can often be led by standard procedures, such as the "load-shedding method", for the measurement of fatigue-crack-propagation rates at near-threshold stress-intensity levels.

- Crack closure is still strongly influenced by the specimen size and geometry, crack size, stress state, prior load history, and the location, with respect to the crack tip, where closure is measured.

- The application of nominally identical values of $\triangle K$ may lead to different levels of crack closure in the same material for different crack sizes.

- Bulk measurements of the crack closure does not distinguish between the different mechanisms of crack closure. These bulk measurement techniques do not provide insights into the fundamental closure phenomena because multiple closure mechanisms may simultaneously influence the rate of fatigue-crack growth.

1.5.7 Retardation Following Tensile Overloads

During the fatigue-crack growth, load excursions in the form of single tensile overload or high amplitude-low amplitude block loading sequences can result in the retardation of the crack advancement. The fatigue-crack-growth curve under a constant load range is shown in Figure 1.11, which schematically illustrates the typical crack-growth behavior following a singe tensile overload [2]. After a tensile overload, the ductile material generally exhibits a small amount of temporarily accelerated crack growth, which mainly occurs during the application of the tensile overload. The burst of the accelerated crack advancement is generally followed by the prolonged period of the decelerated crack growth. The reduction in the crack velocity continues over a crack-growth distance, which is known as the delay distance. After reaching a minimum

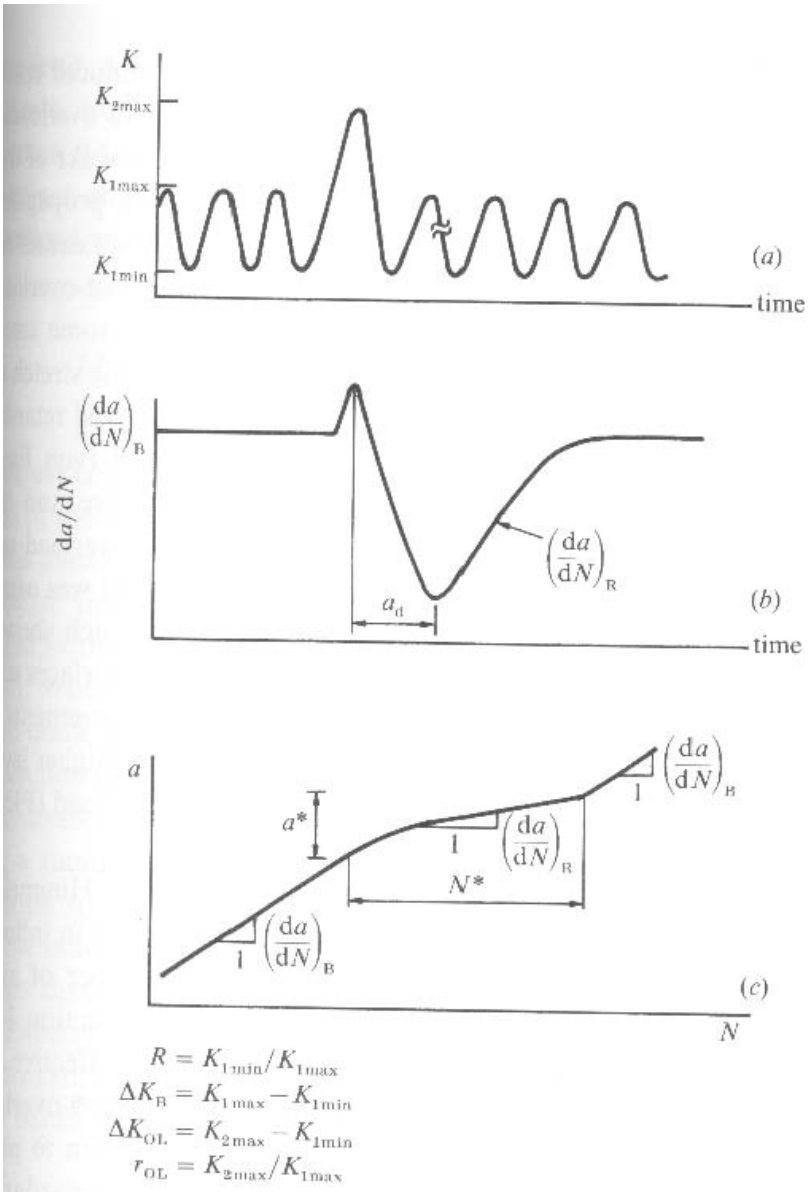


Fig. 14.17. Definitions of different parameters used to describe transient crack growth effects following single tensile overloads.

Figure 1.11: Definitions of different parameters used to describe transient crack-growth effects following single tensile overloads.

crack-growth rate, the crack-propagation rates begin to increase and eventually catch up with the pre-overload value. The total crack distance, a*, and the total number of post-overload cycles, N*, over which the transient effects of the single tensile overload affect crack growth, are a strong function of the stress-intensity-factor range $\triangle K$, the material microstructure and environment, as well as such factors as the nominal load ratio, R, and the overload ratio, $r_{OL}=\frac{P_{overload}}{P_{max}}$. $P_{overload}$ is the overload

1.5.8 Transient Effects Following Compressive Overloads

It is generally believed that compressive stresses do not make any significant changes in crack-growth rates, because fatigue cracks remain closed during the compressive loading. However, there has been a growing body of evidence, which shows that for both long and short crack lengths, the application of the compressive overloads can lead to the acceleration in the crack-growth rates. It is shown that fully compressive cyclic loads of both constant and variable stress amplitudes yield the nucleation and growth of fatigue cracks ahead of stress concentrations. The mechanism underlying this effect involves the generation of residual tensile stresses upon unloading. The influence of the compressive overloads on the growth of long fatigue cracks is strongly dependent on the micromechanisms of the crack growth, in particular on the prior development of the crack-surface morphology and roughness-induced crack closure. The factors depend on the microstructural dimensions as the grain size.

1.5.9 Load-Sequence Effects

Different combinations of cyclic loads influence fatigue fracture are studied. Examples of transient effects induced by block loads are presented. Figure 1.12 is a scanning-electron fractograph showing fatigue striations in a 2034-T3 aluminum alloy subjected to a high-low block loading sequence [2]. Block B leads to the formation of well-defined striation markings during each cycle. Upon switch from blocks B to A, crack growth continues at a slower rate with a corresponding reduction in the striation spacing. If the load is switched again from blocks A to B, a stretch zone is created as a consequence of the abrupt increase in the peak tensile stress. Figure 1.13 is another example of tensile block loading where the peak tensile stresses for the blocks are the same, and the stress amplitude in each block is different. Blocks B and C cause crack growth, with the rate of the crack advancement per cycle corresponding to the respective striation spacing see in Figure 1.13. The stress amplitude of block A was too small to cause any crack growth. The rate of the fatigue-crack growth is also depend on the order in which tensile and compressive overloads are applied. Figure 1.14 schematically shows typical effects of tension-compressive sequence effects on the variable-amplitude fatigue fracture. The application of the tensile overload blunts the crack tip. After a compressive overload applied immediately after a tensile overload, the crack tip, which is blunted by the tensile overload, behaves like a notch. The applied compressive load results in the formation of the residual tensile stresses, which nucleate a fatigue crack. These residual tensile stresses can partly or fully nullify the beneficial delay effects associated with the tensile overload [55]. If a compressive overload precedes a tensile overload, the rate of fatigue

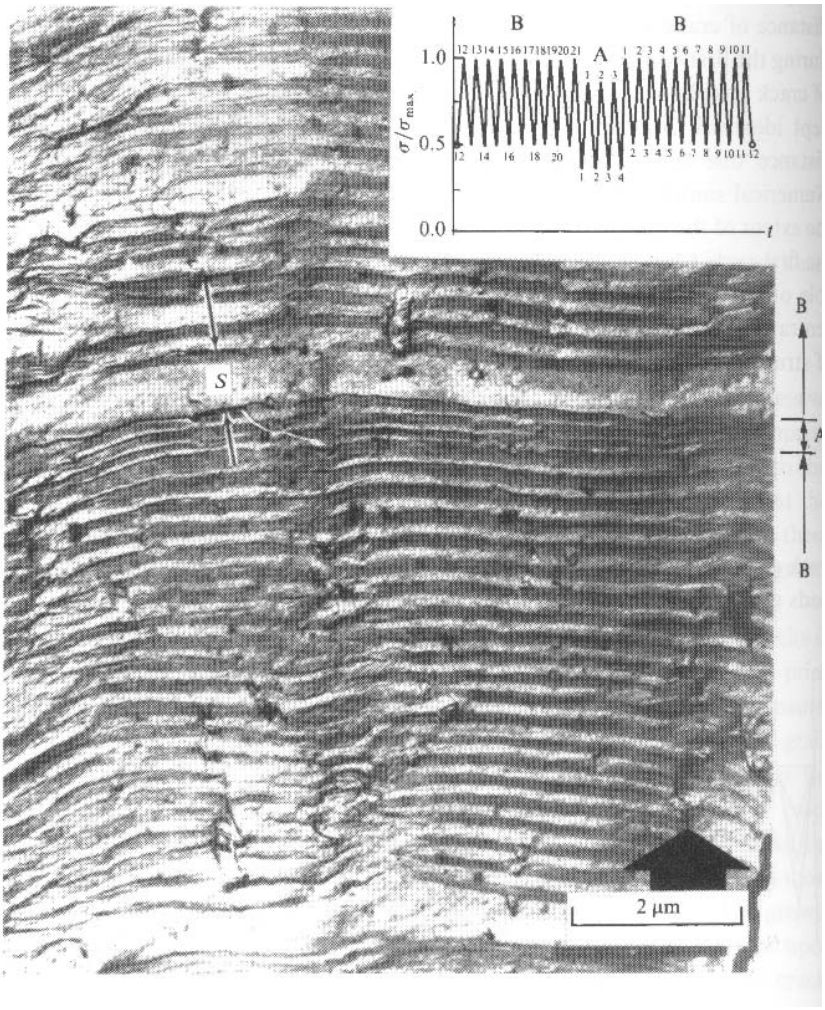


Figure 1.12: Typical fractography resulting from a high-low-high block loading sequence applied to a 2024-T2 aluminum alloy. [2]

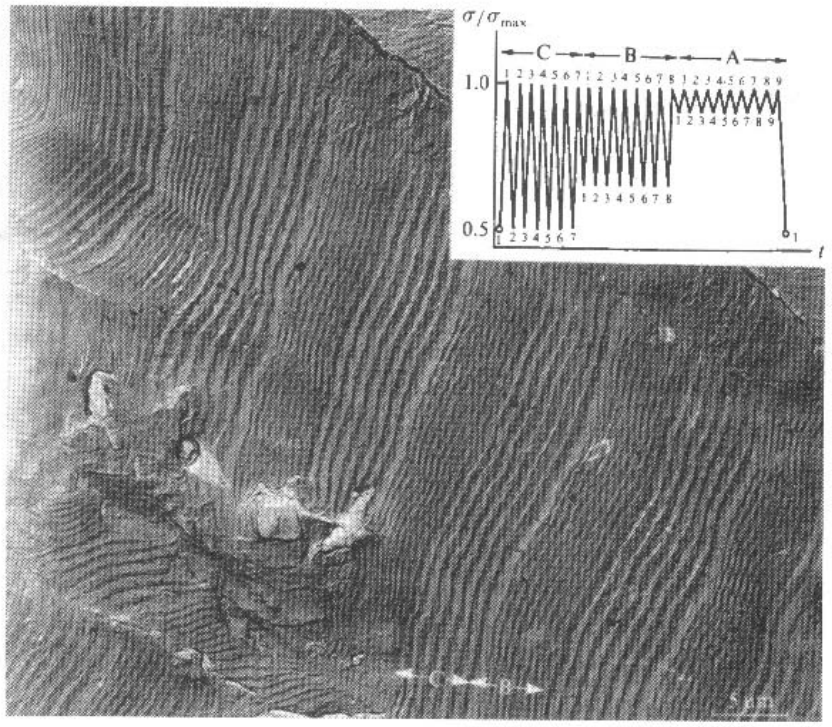


Figure 1.13: Typical fracture surface due to a block loading in a 2024-T3 aluminum alloy. [2]

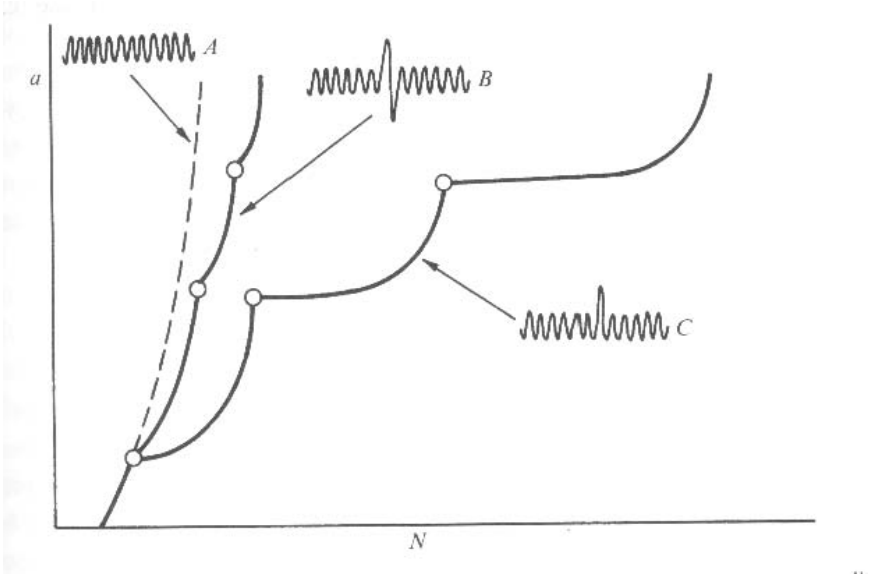


Figure 1.14: Schematic illustration of transient crack growth during constant-amplitude fatigue (A curve), and during variable amplitude loading involving single tensile overloads (C curve) or tensile-compressive overload sequences (B curve). The open circles represent the crack length locations at which each variable amplitude sequence is applied. [2]

crack may increase or remain the same, depending on the loading conditions. For long fatigue cracks, which grow in the Paris regime, the application of a compressive overload prior to a tensile overload may not have any significant effect on the delayed retardation.

1.5.10 Analyses of Variable-Amplitude Fatigue

Variable-amplitude fatigue can involve either a regular pattern of cyclic stresses or a random sequence of loads. For this analysis, the history effects can be quite pronounced. Currently, the most accurate means of quantifying the fatigue life in variable-amplitude loading involves the cycle-by-cycle integration of one of the retardation models, which is called Wheeler model. The Wheeler-retardation model is implemented in much the same manner as for overload cases, except that the overload plastic-zone size, $r_{y(o)}$, and the current plastic size, $r_{y(c)}$, must be evaluated for each cycle in a variable-amplitude problem. Figure 1.15 illustrated a typical scenario, where a very high-stress cycle occurred earlier in the history, and a moderately high stress occurred in the previous cycle. The overload plastic zone is chosen such that the retardation factor, Φ_R, is minimized. In this case, the more recent overload is considered, despite the fact that it produced a smaller plastic zone than the earlier peak stresses. An important point about the Wheeler model is that it depends on material properties and stress spectrum.

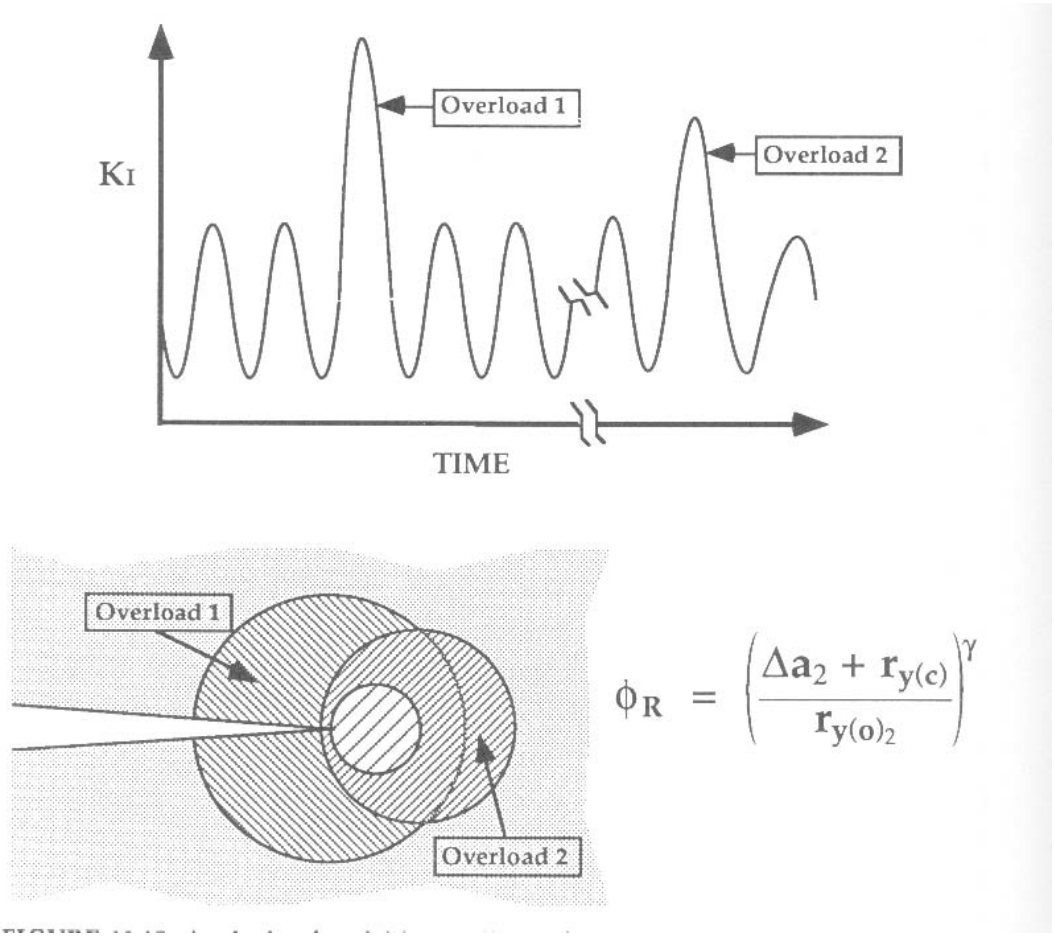


Figure 1.15: Analyses of variable-amplitude fatigue with the Wheeler-retardation model. The overload plastic-zone size, $r_{y(0)}$, is chosen so as to minimize Φ_R [2]

1.5.11 Finite-Element Analyses of the Plasticity-Induced Fatigue-Crack Closure

During loading, large tensile plastic strains are developed near the crack tip, which are not fully reversed upon unloading as the crack undergoes cyclic loading. This trend leads to the formation of the plastic wake behind the crack tip as the crack extends, and a subsequent reduction of the driving force for fatigue-crack growth. It is also noteworthy that the plastic deformation induced near the crack tip during loading results in a compressive residual stress when the load is released. The effect of this residual stress on the crack-driving force may also be significant, and it is in fact difficult to separate the mechanical behavior in front of and behind the crack tip.

Many researchers have performed finite-element analyses simulating the plasticity-induced fatigue-crack closure, considering different two-dimensional through-thickness cracked configurations under plane-strain or plane-stress conditions. Fewer efforts have been directed toward the three-dimensional problem.

- two-dimensional finite-element modeling

  A mesh is created with an initial crack, and then the mesh is loaded.

  1. Mesh refinement

     As a fatigue crack propagates, two different types of the crack-tip plastic zones are generated as shown in Figure 1.16. The forward plastic zone near the crack tip undergoes the plastic deformation at the maximum load. The second zone is the reversed plastic zone, which is defined near

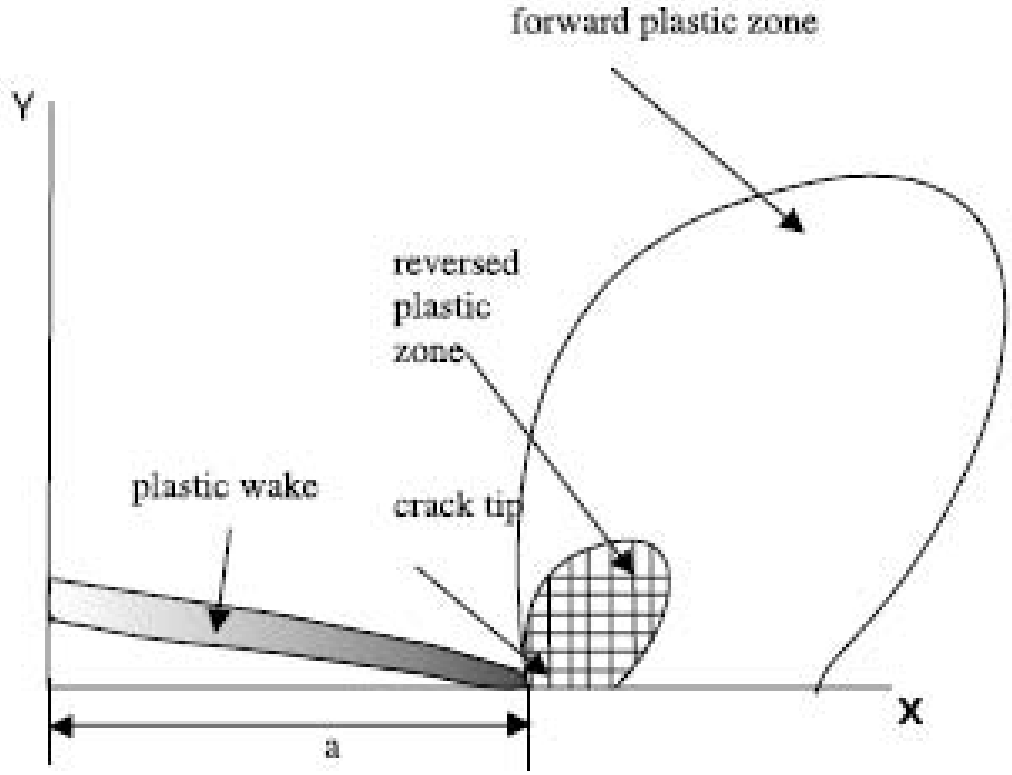


Figure 1.16: Plastic deformation around a growing crack [2]

the crack tip undergoing compressive yielding at the minimum load [56]. These crack-tip plastic zones will be used to characterize the degree of the finite-element-mesh refinement.

The level of the mesh refinement plays an important role. It is critical that finite-element meshes are not refined excessively, which give the severe computational burden associated with the finite-element simulation of fatigue growth. However, if the mesh used is too coarse, inaccurate results may be obtained.

2. Finite-element analyses

   Fatigue-crack-closure analyses were performed using ANAYS [57]. Two-dimensional finite-element analyses of compact-tension (CT) and middle-tension (MT) geometries were conducted using four-node quadrilateral elements and three-nodel triangular elements. The material was assumed to be elastic-perfectly plastic. The specimens geometries are shown in Figure 1.17. Following a monotonic analysis, if the actual initial forward plastic zone extended out of the refined region and into the transition region, then the refined region was enlarged so that the entire plastic zone was captured.

3. Results

   – A crack growing under cyclic loading with R = 0 showed a reversed plastic zone of about 1/10 of the forward plastic zone. This is in contrast to the stationary crack, which theoretically exhibits a reversed plastic zone of 1/4 of the forward plastic zone [58]. This difference is

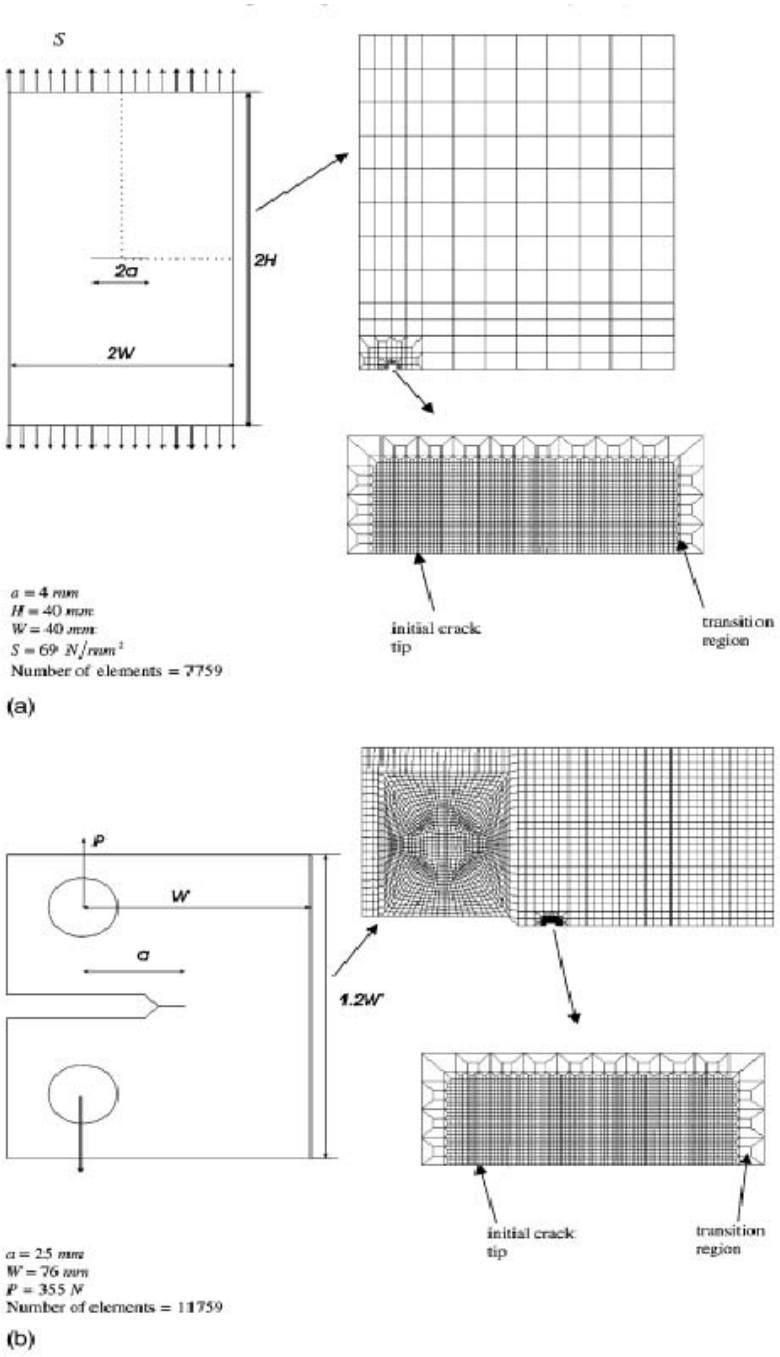


Figure 1.17: (a) Typical MT model and (b) typical CT model

a consequence of the plastic wake, which forms behind the growing crack.

  - The MT specimen crack-opening values converged with increasing levels of the mesh refinement under both plane-stress and plane-strain conditions. However, for the CT specimen, no convergence was observed under the plane-strain conditions. The plasticity-induced closure is negligible or does not exist under the plan-strain condition for the CT specimen.

- Three-dimensional finite-element modeling

  A relaively small number of investigators have modeled the plasticity-induced crack closure in three-dimensional (3-D) geometries using finite-element methods [59–64] In a three-dimensional geometry, the crack-opening value will vary along the crack front. For simplicity, the crack-shape evolution is neglected, and the crack front is extended uniformly during the analysis. The majority of the published 3-D modeling efforts have considered the MT geometry. In addition, limited modeling of the plasticity-induced crack closure in the part-through surface-flawed geometry has been performed.

1.5.12 Cohesive-Zone Modeling

The consideration of the infinite stresses at the crack tip is not realistic. Models to overcome this drawback have been introduced by Dugdale [65] and by Barenblat [66].

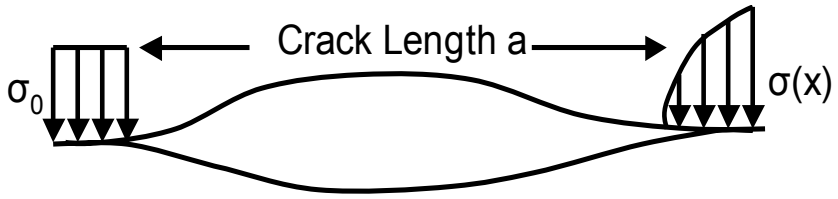


Figure 1.18: Dugdale (left) and Barenblatt (right) crack models

Both authors divided the crack in two parts: One part of the crack surfaces is stress free, and the other part is loaded by cohesive stresses in Figure 1.18 .

Cohesive-zone models provide advantages of allowing a spontaneous crack nucleation, crack branching, and fragmentation, as well as crack propagation without an external fracture criterion [67, 68]. Cohesive-zone models incorporate a cohesive strength and finite work to fracture in the description of the material behavior, and allow the simulation of the near-tip behavior and crack propagation.

The concept of the "cohesive failure" is illustrated in Figure 1.19 [3]. A cohesive zone is present in front of the crack tip. Within the extent of the cohesive zone, the material points, which are identical when the material was intact, separate to a distance, Δ, due to the influence of a high stress state at the crack-tip vicinity. The cohesive zone surface sustains a distribution of the traction, T, which is a function of the displacement, Δ, and the relationship between the traction, T, and separation, Δ, is defined as the traction-separation law.

- Mechanisms of cohesive models

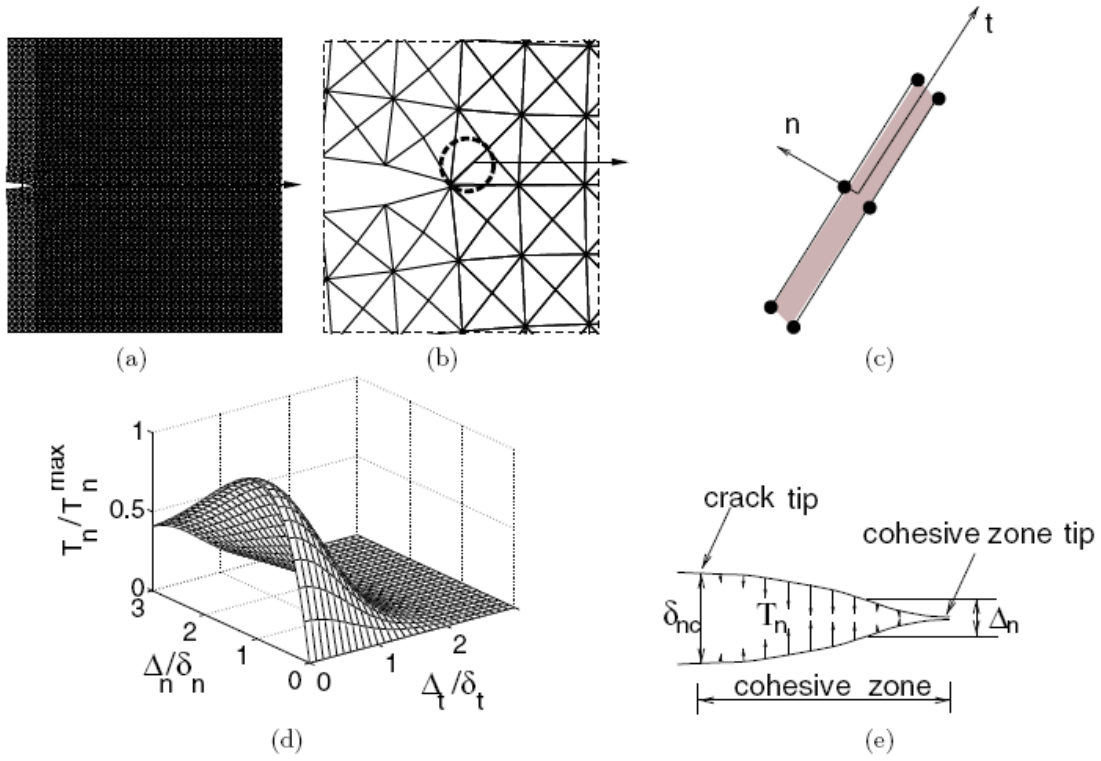


Figure 1.19: Schematic representation of the cohesive-zone-model concept; (a) A plate containing a crack; At a potential crack-propagation path e.g., as circled in (b), a cohesive element is inserted, as shown in (c), which follows the specified cohesive-zone model shown in (d) for the normal traction; and (e) a cohesive zone in a Mode-I case [3]

The cohesive models are different from Barenblatt's model in that they define the traction acting on the ligament in a dependency on the opening and not to the crack-tip distance as Barenblatt did.

The material separation and, thus, the damage of the structure are classically described by interface elements: no continuum elements are damaged in the cohesive model. Using this technique, the behavior of the material is split in two parts, the damage-free continuum with an arbitrary material law, and the cohesive interfaces between the continuum elements, which specify only the damage of the material.

The interface elements open when a damage occurs and loose their stiffness at failure so that the continuum elements are disconnected. For this reason the crack can propagate only along the element boundaries. If the crack-propagation directions are not known in advance, the mesh generation has to make different crack paths possible.

The separation of the cohesive interfaces is calculated from the displacement jump $[u]$, i.e., the difference of the displacements of the adjacent continuum elements, $\delta = [u] = u^+ - u^-$. More common than the definition of the separation vector in global coordinates is the description in a local coordinate system, namely the distinction between the normal separation, δ^N, and tangential separation, δ^T. The separation depends on the normal and the shear stress, respectively, acting on the surface of the interface. When the normal or

tangential component of the separation reaches a critical value, δ_0^N or δ_o^T, respectively, the continuum elements initially connected by this cohesive element, are disconnected, which means that the material at this point has failed [69].

Besides the critical separation, δ_0, the maximum traction (the stress at the surface of the continuum element), T_0, is used as a fracture parameter, also denoted as a "cohesive strength." The value of T_0 only describes the maximum value of a traction-separation curve, $T(\delta)$, in the following denoted as the cohesive law. Like the separations, the stresses, T, can also act in normal or in tangential direction, leading to a normal or shear fracture, respectively. The shape of the curve, $T(\delta)$, which is assumed to be a material-independent cohesive law, is defined differently by various authors [5–8]. Common to all cohesive laws is that

1. They contain the two material parameters, T_0 and δ_0, mentioned above and
2. For the total failure, the stresses become zero, $T(\delta > \delta_0 = 0$ for both the normal and tangential separations. [69]

The integration of the traction over the separation, either in normal or in tangential direction, gives the energy dissipated by the cohesive elements, Γ_0. This third parameter can be determined from the former two by $\Gamma_0 = \int T(\delta) d\delta$.

- Traction separation law, TSL

  The form of the function, $T(\delta)$, is defined in the traction-separation law (TSL). Since the cohesive model is a phenomenological model, there is no evidence for

choosing the form for $T(\delta)$. So it has to be assumed to be independent of the material. In the literature, one can find several approaches, some of them are shown in Figure 1.20 . The implemented TSL's are the cubic form of Needleman [4] with its extensions regarding the shear fracture and unloading due to the Tvergaard [70] and exponential curve from Needleman [4]. In addition, a TSL similar to the law with a constant stress [5], first mentioned in [71], is developed and implemented [69].

Cohesive-zone models can be categorized into two major groups [3]: intrinsic and extrinsic. In the intrinsic cohesive-zone model, the traction, T, first increases with increasing the interfacial separation, Δ, reaches a maximum value, δ, then decreases and finally vanishes at a characteristic separation value, δ_c, where a complete decohesion is assumed to occur. In contrast, the extrinsic cohesive-zone model does not display the initial ascending branch of the curve.

- Hysteretic-traction separation law

  Cohesive theories regard the fracture as a gradual process in which the separation between material surfaces is resisted by the cohesive law. In some models, unloading from - and subsequent reloading towards - the monotonic envelop is taken to be linear, e.g., towards the origin, and elastic, or nondissipative [68, 72]. Such models cannot be applied to the direct cycle-by-cycle simulation of fatigue-crack growth. The hysteretic-traction-separation law reveals that a crack subjected to constant-amplitude cyclic loading, and obeying a cohesive law with elastic unloading, tends to shake down, i.e., after the passage of a small number of cycles all material points, including those points

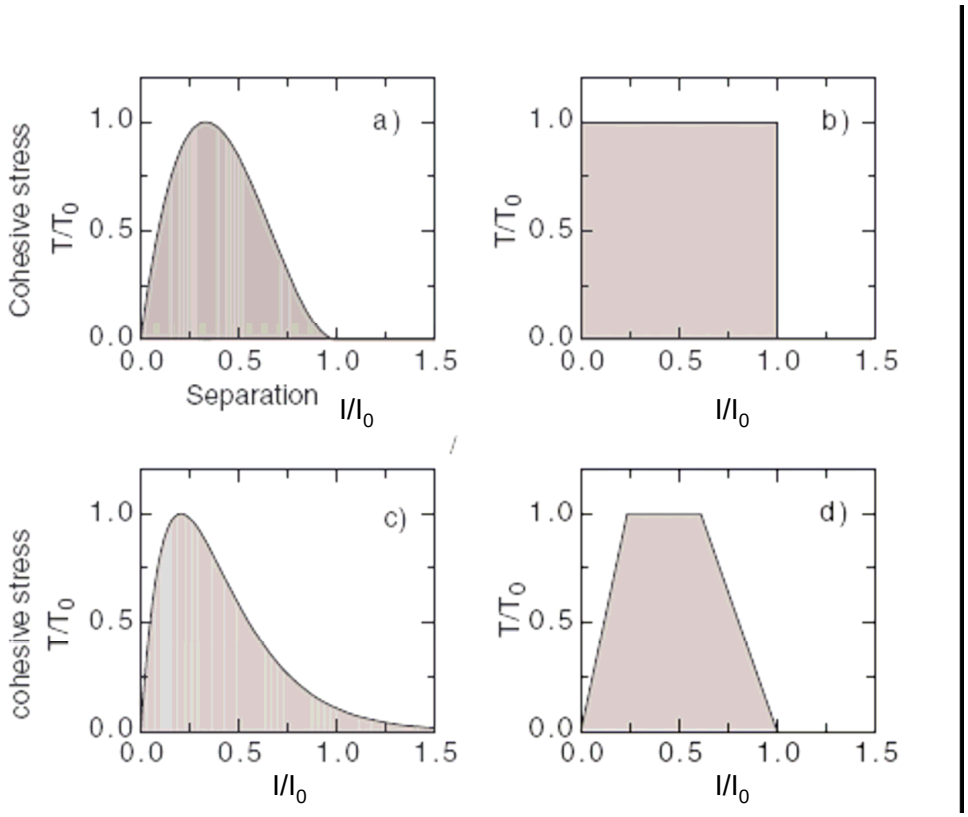


Figure 1.20: Form of the TSL: a) cubic, from [4], b) constant, from [5], c) exponential, from [6], and d) trilinear, from [7, 8]

on the cohesive zone, undergo an elastic cycle of deformation, and the crack arrests [73]. The centerpiece is an irreversible cohesive law with unloading and reloading hystereses. The inclusion of unloading-reloading hystereses into the cohesive law is intended to simulate the dissipative mechanism, such as the crystallographic slip and frictional interactions between asperities [73].

First monotonic-loading processes were considered, resulting in a pure mode-I opening of the crack. As the fracture surface opens under the action of the loads, the opening is resisted by a number of material - dependent mechanisms, such as the cohesion at the atomistic scale, bridging ligaments, interlocking of grains, and others [73]. For simplicity, the resulting cohesive traction, T, is assumed to decrease linearly with the opening displacement, δ, and eventually reduce to zero upon the attainment of a critical opening displacement, δ_c [68, 74]. The relation between T and δ under monotonic opening is referred as the monotonic cohesive envelope. For fatigue applications, the specification of the monotonic-cohesive envelope is not enough, and the cohesive behavior of the material under cyclic loading is of primary concern. The process of unloading from - and reloading towards - the monotonic cohesive envelope is assumed to be hysteretic. Furthermore, the unloading - reloading response degrades with the number of cycles. The traction and separation law for a hysteretic - cohesive model is shown in Figure 1.21. Thus, a fatigue-crack-growth model can be developed.

- Consideration of normal and shear fracture

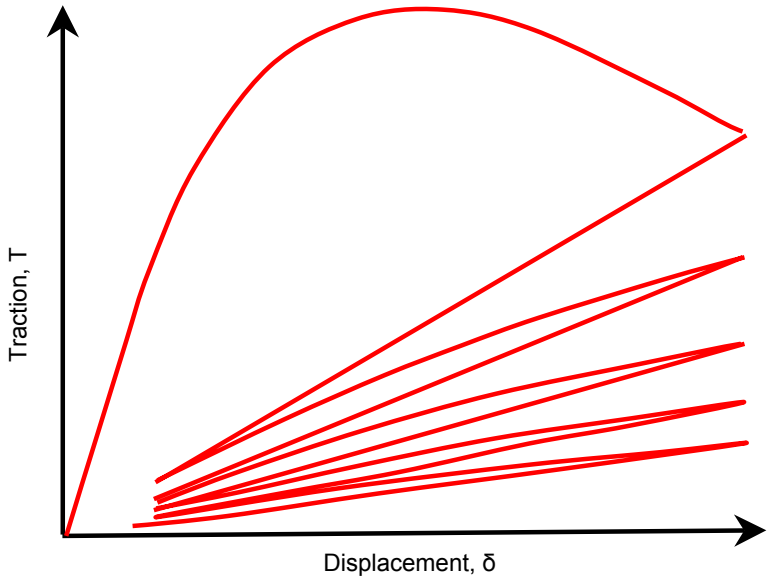


Figure 1.21: Traction and separation law for a hysteretic-cohesive model

In order to consider simultaneously acting normal and shear fracture, one has to define a new quantity for the damage and failure. Failure occurs in a pure normal fracture when the separation exceeds the maximum separation, δ_0^N. At the combined normal and shear fracture (local in the cohesive element), the quantity, which defines the failure, contains a normal and a shear component, i.e., the shear damage will reduce the ductility in the normal direction and vice versa. This influence of the competing normal and tangential separations is to define an interaction formula of the shear and normal separations

$$\sqrt[m]{(\frac{\delta^N}{\delta_0^N})^m + (\frac{\delta^T}{\delta_0^T})^m} \tag{1.12}$$

Equation 1.12 contains a model parameter, m, which is a connection parameter. One can determine two limiting cases from Equation 1.12, namely m = 1, that means a linear connection between the normal and tangential damages, and m = ∞, which leads to a vanishing influence of one fracture mode to another. The damage and final fracture of a cohesive element are plotted for m = 1 and m = 2 in Figure 1.22 . It should be mentioned that most references use m = 2 as the damage indicator, for which the damage is equal to the absolute value of the separation.

As can be seen in the figure, the maximum normal separation decreases with increasing the shear separation. Another way to embed the influence of the tangential on the normal opening (and vice versa) is to define the normal-traction dependence on δ^T explicitly. In both cases, the separation function

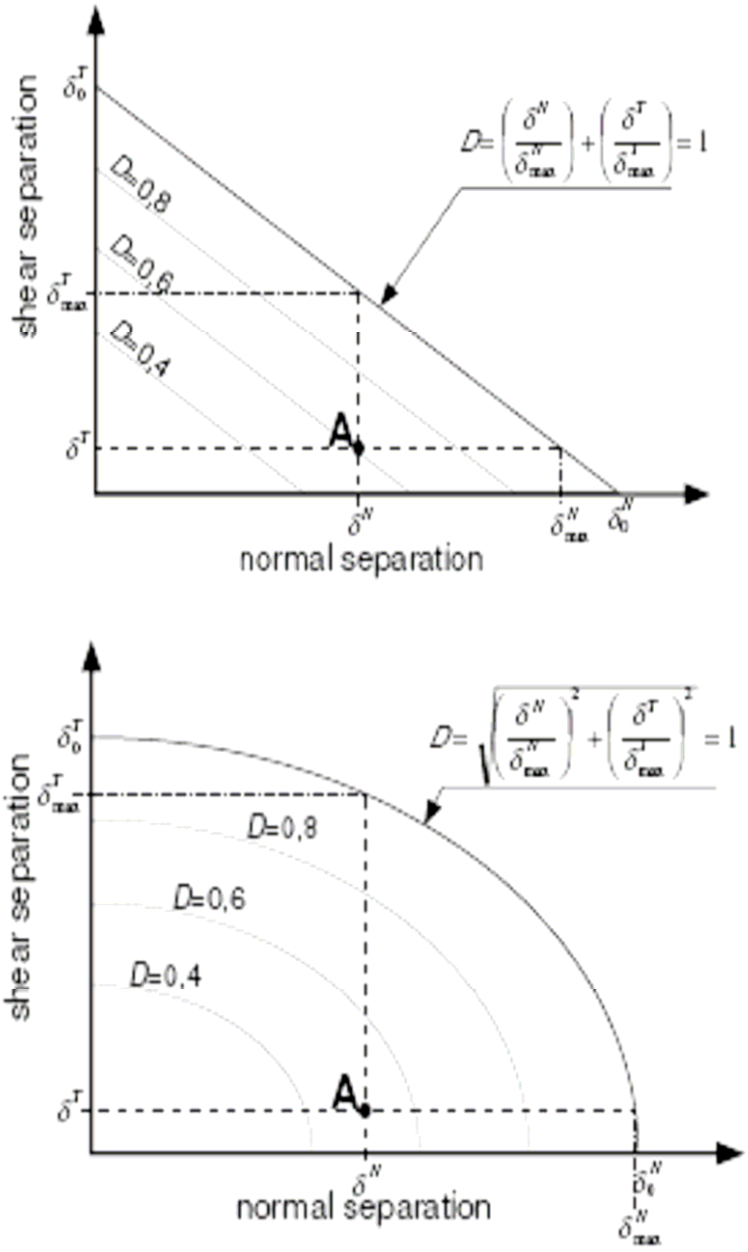


Figure 1.22: Interactions between normal- and shear separations [3]

does not only depend on δ^N, but also on δ^T and/or on the damage, D. Generally one can write for the TSL [69, 71]

$$T^N = T^N(\delta^N, D, \delta^T) T^T = T^T(\delta^T, D, \delta^N) \tag{1.13}$$

The cohesive model has been implemented using the programming language, FORTRAN, as a user-defined element within the FE code, ABAQUS [75]. The body of the user-element routine for two-dimensional problems (linear-shape cohesive elements) was developed by Siegmund [69].

Chapter 2

Neutron-Diffraction Studies on Lattice-Strain Evolution around a Crack Tip during Tensile Loading and Unloading Cycles

2.1 Introduction

Fracture mechanics is a science that relates the global-loading configuration to the stress and strain state around a crack tip. From a material-development perspective, new materials with a better cracking resistance could be designed only after a better understanding of the damage mechanism. The effect of an overload [76], as shown in Figure 2.1, on the crack-propagation behavior during a cyclic deformation has

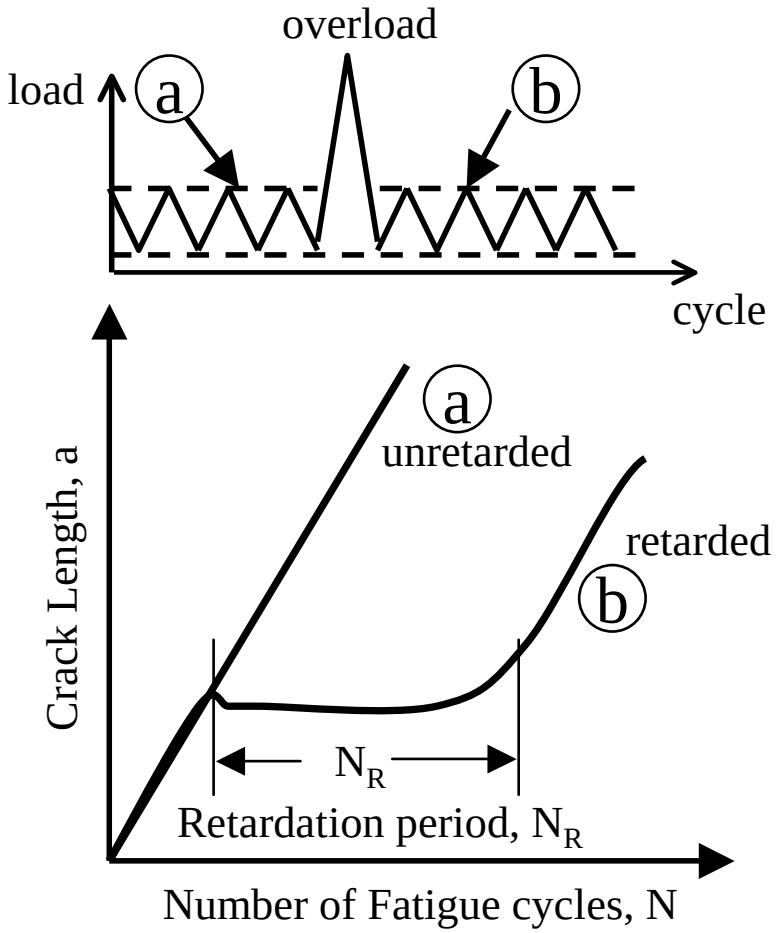


Figure 2.1: Schematic of the overload effect.

drawn much attention since its discovery in 1961 [77]. However, the phenomenon is still not well understood. After the overload, there is a period of crack-growth retardation (Figure 2.1) that is related to the magnitude [78–81] and number of overloads [76, 82, 83]. The retardation of the crack-growth behavior can be understood in the context of the plasticity-induced crack-closure mechanism. The plastic deformation of the material in the wake of the crack leads to the premature contact of the crack faces in the unloading sequence, resulting in the reduced cyclic-plastic deformation and, therefore, the decreased crack-propagation rate. Measuring the residual strains near the crack tip associated with the prior plastic deformation can help understand the crack-propagation behavior and investigate the overload effect. In general, compressive residual strains/stresses are found to decrease the crack-growth rates, while tensile residual strains/stresses increase the rates [84]. The size of the plastic zone at the crack tip created by prior loading can provide a measure of the deformation around the crack tip. Therefore, a method for measuring residual stresses and the plastic zone surrounding a crack is useful for understanding the crack-growth behavior and the crack-tip deformation mechanism [85].

Neutron diffraction, as a nondestructive-evaluation technique, can determine the elastic lattice strains in a polycrystalline material from the shift of the diffraction peaks. At the same time, the plastic deformation can be estimated from the broadening of the diffraction peaks. In the present investigation, lattice strains near a fatigue crack in a compact-tension (CT) specimen were measured during tensile loading and unloading cycles using neutron diffraction to determine the effect of the overload.

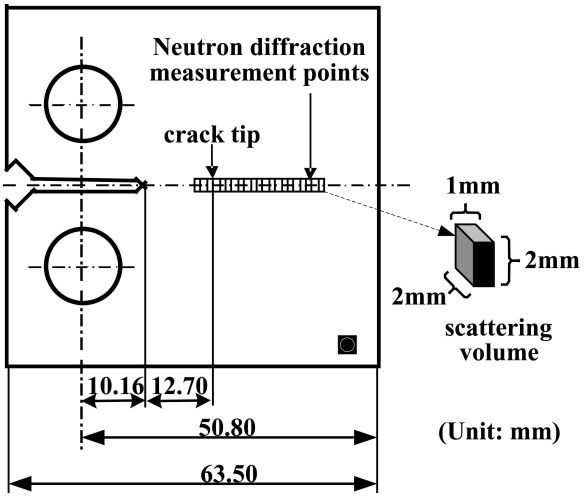


Figure 2.2: Compact-tension specimen of Type 316 LN stainless steel with a thickness of 6.35 mm, a notch length of 10.16 mm, and a crack length of 22.86 mm. Diffraction patterns were measured along the crack length with a scattering volume of $2 \times 1 \times 2\ mm^3$ with the 1 mm along the crack length.

Diffraction-peak broadening was also determined near the crack tip to estimate the plastic-zone size.

2.2 Experimental Details

The experiment was performed on a CT specimen of a Type 316 LN stainless steel, which is a low-carbon nitrogen-added (LN) austenitic-stainless steel. A schematic of the CT specimen, with a width of 50.8 mm, a thickness of 6.35 mm, and a notch length of 10.16 mm, is shown in Figure 2.2. The CT specimen was pre-cracked under a fatigue-loading condition using a Material Test System (MTS) electrohydraulic machine. Fatigue loading was performed in a load-control mode with a frequency of 10 Hz and a constant load ratio, R = 0.1, where $R = P_{min.}/P_{max.}$, $P_{min.}$ and

$P_{max.}$ are the applied minimum (667 N) and maximum (6,667 N) loads, respectively. The maximum stress intensity, $K_{max.}$, reached 38.8 MPa$\sqrt{m}$ during fatigue-crack growth. The K value was obtained, using Equation 1.2 [49, 86, 87]. The total crack length was extended to 22.86 mm after 169,052 cycles. Crack length was measured by the crack-opening-displacement (COD) gauge using the unloading-compliance technique [47, 88–91]. After the test, the crack length was also confirmed by the dye-penetrant inspection, and the results agree within 0.02 mm.

Neutron-diffraction measurements were performed on the Spectrometer for Materials Research at Temperature and Stress (SMARTS) [92] at the Los Alamos Neutron Science Center (LANSCE). Utilizing the continuous energy spectrum of the incident neutron beam, the entire diffraction pattern (d-spacings ranging from 0.5 to 4$\dot{A}$) was recorded in two stationary detector banks at fixed diffraction angles (2θ) of $\pm$ 90°. The samples were aligned such that the tensile load axis was 45° from the incident beam and, thus, the diffraction vectors associated with the two detector banks were parallel to the in-plane and through-thickness directions of the sample. The incident neutron beam was defined by 2 mm and 1 mm (along the crack length) slits, and the diffracted beams were collimated using 2 mm radial collimators, resulting in a 4 mm^3 gauge volume, Figure 2.2. Thirty-two diffraction patterns were recorded along the crack length at a given applied load. The interatomic spacings in the in-plane direction (parallel to the loading direction) were determined by the Rietveld refinement [93] of the diffraction patterns, and, subsequently, the lattice strains were calculated from

$$\varepsilon = \frac{a - a_0}{a_0} \tag{2.1}$$

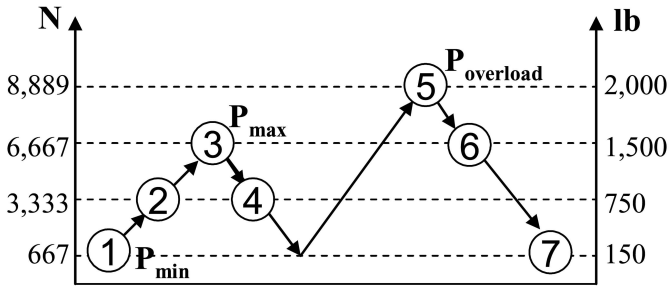


Figure 2.3: Applied tensile loading-unloading sequence. Neutron-strain scanning was performed at each load point (LP) from LP1 through LP7.

where a_0, the stress-free lattice parameter, was measured away from the crack tip (marked ■ in Figure 2.2). The analysis of the through-thickness data will not be discussed in this paper, due to the length constraint.

The strain scan was repeated at seven different load values as shown in Figure 2.3. In this paper, the measurement results at load points (LP) 1 (667 N), 2 (3,333 N), 3 (6,667 N), 5 (8,889 N), 6 (6,667 N), and 7 (667 N) are presented. The LP5 is an overload.

In polycrystalline materials, the plastic deformation may generally be related to the broadening of a diffraction peak [94] although other factors, such as small grain sizes, can contribute to broadening. The extent of the plastic zone in front of the crack tip is a function of the prior loading history of the CT specimen. From the changes in the full-width-half-maximum (FWHM) as a function of scanning positions, the plastic zone near the crack tip was estimated. The peak-width change was determined, using:

$$\Delta SIG = \frac{SIG_f - SIG_0}{SIG_0} \tag{2.2}$$

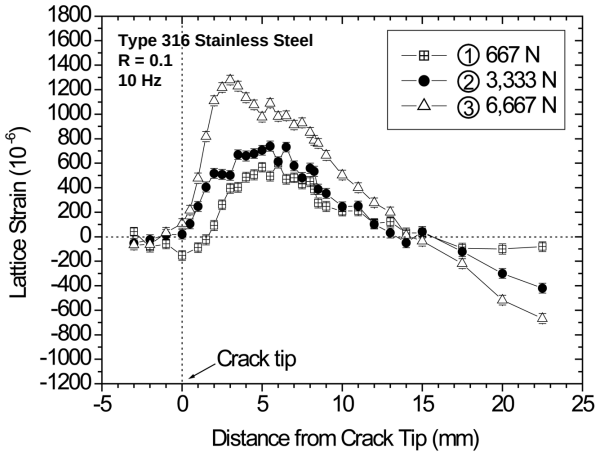


Figure 2.4: In-plane lattice-strain profiles in front of the crack tip at applied loads of 667 N, 3,333 N, and 6,667 N, which correspond to LP1, LP2, and LP3, respectively, in Figure 2.3.

where ΔSIG is the fractional peak-width change, and SIG_f and SIG_0 represent the square of the variance of the diffraction peaks, determined for the strained and unstrained materials, respectively, using the Rietveld refinement [93].

2.3 Results and Discussions

Figure 2.4 shows the in-plane (IP) lattice-strain profiles measured at various applied loads (LP 1, 2, and 3 in Figure 2.3). At 667 N (LP1), in the IP direction, small compressive strains (with a maximum of - 194×10^{-6} or $\mu\varepsilon$) were observed within $\pm$ 3 mm of the crack tip. The strains become tensile in front of the crack tip, reaching a maximum value of 526×10^{-6} (or $\mu\varepsilon$) at approximately 5 mm from the crack tip, and then decreasing as the distance increases. At about 15 mm, the strains become compressive. When the load is increased from 667 N to 6,667 N (LP3), the maximum

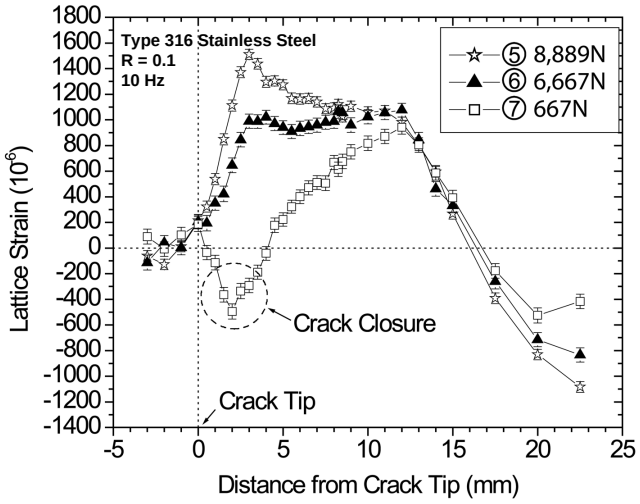


Figure 2.5: In-plane lattice-strain profiles in front of the crack tip at applied loads of 8,889 N, 6,667 N, and 667 N, which correspond to LP5, LP6, and LP7, respectively, in Figure 2.3.

strain gradually increased. Two maxima were observed in the strain profile at 6,667 N. The first maximum (at about 3 mm from the crack tip) is associated with the in-situ applied loading of the sample, while the second maximum (at about 6 mm from the crack tip) is associated with the bending effect due to the long crack length. Note that the bending effect is an unforeseen effect, which caused a tensile to compressive transition at around 15 - 17 mm.

The lattice-strain profiles in the IP direction in front of the crack tip as a function of the applied load after the overload at LP5 is presented in Figure 2.5. The first maximum in the strain profile (at around 2 - 3 mm from the crack tip) diminished as the applied load was decreased from 8,889 N (LP5) to 667 N (LP7). At the tensile load of 667 N following the overload to 8,889 N, compressive lattice strains of up to - 600 $\mu\varepsilon$ were observed within 4 mm from the crack tip, indicating the plasticity-induced crack closure. This trend could, subsequently, retard the crack propagation,

decrease the crack-growth rate, and increase the fatigue life. The lattice-strain profile associated with the bending continues to show a transition from the tensile to compressive strains at about 15 - 17 mm from the crack tip, showing maximum strains decreasing with a decrease in applied tensile loadings.

The plastic-zone size (2r) was calculated to be 7.9 mm at LP7 using [e.g., [1]]:

$$2r = \frac{m-1}{m+1} \times \frac{1}{\pi} \left(\frac{K_{\max}}{\sigma_0} \right)^2 \tag{2.3}$$

where K_{max} is the maximum stress-intensity factor of 51.8 MPa$\sqrt{m}$, which was calculated using Equation 1.2 with $P_{overload}$ = 8,889 N, crack length, a = 22.86 mm. Note that the crack length did not grow immediately after the overload (i.e., at LP7). σ_0 is the yield strength of the material (288 MPa) [23-25] and m (= 7.7) is the inverse of the strain-hardening exponent, which was a material constant derived from the regression of the stress-strain curve [22, 23].

The elastic lattice-strain profile at LP7 is plotted in Figure 2.6 along with the changes in the diffraction-peak width. The increase in the peak width in front of the crack tip indicates the plastic-zone size. Thus, there is a good agreement between the plastic-zone sizes determined from the theoretical prediction (7.9 mm) and peak-width-broadening measurements (about 7 - 9 mm). The plastic deformation during the overload caused the compressive lattice strain in front of the crack tip, which could induce the crack-closure phenomenon. Finally, it should be noted that the sharp transition from tensile to compressive strains at around 15 - 17 mm due to the bending effect did not cause any significant diffraction-peak broadening. The 1-mm

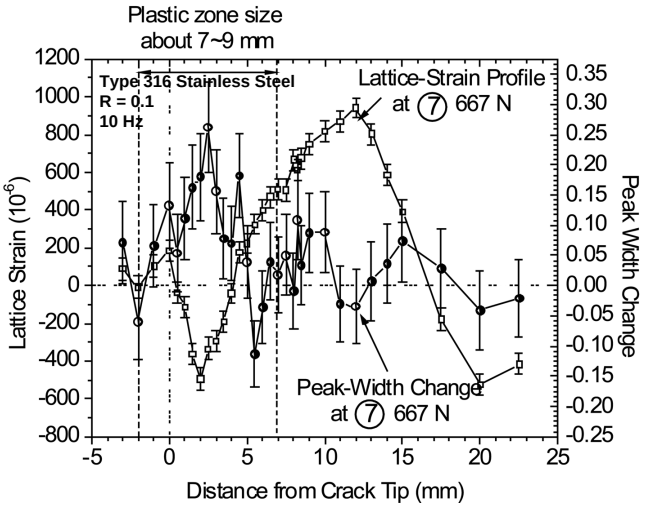


Figure 2.6: Comparison between the in-plane lattice strain profile and the plastic-zone size (about $7 \sim 9$ mm) estimated from the changes in the diffraction-peak width at 667 N (LP7 in Figure 2.3). Note that the plastic-zone size calculated using Equation 2.3 is about 7.9 mm.

spatial resolution used along the crack length may have been small enough to resolve the gradient around 16 mm avoiding significant diffraction peak broadening.

2.4 Summary

Elastic-lattice strains and the associated plastic zone around the crack tip in Type 316 LN steel were investigated using an in-situ neutron-diffraction technique. The elastic strains in the in-plane direction (parallel to the loading direction) were measured as a function of the distance from the crack tip at different applied loads ranging from 667 N to 8,889 N. The results showed the evolution of lattice-strain profiles associated with the in-situ applied loading as well as the residual-strain profile generated by an overload. After the overload, a significant compressive strain of - 600 $\mu\varepsilon$ (or $\times$ 10^{-6}) was observed in front of the crack tip, which is related to the crack-closure phenomenon and retardation of crack growth. The plastic zone size in front of the crack tip was also estimated, using the peak-broadening analysis, and it agrees well with the theoretically predicted plastic-zone size of 7.9 mm.

Chapter 3

The Study of Crack-Closure Phenomena after the Overload

3.1 Introduction

The material studied is a Type 316 low-carbon, nitrogen-added (LN) austenitic stainless steel (SS). It has already been widely used in the nuclear industry, because of its excellent ductility, corrosion resistance, and irradiation performance. It's often used over a wide temperature range [18], and employed in components that are loaded under severe conditions (stress, strain cycling, and thermal cycling) [11, 16, 17, 95]. However, this material hasn't been systematically investigated regarding its fatigue behavior including the crack-growth resistance. From a material-development perspective, new materials with a better cracking resistance could be designed only after a better understanding of the damage mechanism. The fatigue-crack-propagation

study is an essential part of the structural integrity-assurance-technology development based on damage-tolerance considerations. The fatigue-crack growth is strongly affected by the applied stress level and the extent of the near-tip plasticity.

The changes in the load patterns result in transient effects, which affect fatigue-crack-growth rates and the fatigue life. Load-interaction phenomena complicate life predictions, and their understanding is crucial to crack-growth predictions. For common engineering components, variable-amplitude loading is often much more realistic than constant-amplitude loading as the cause of fatigue failures. The ability to predict quantitatively the phenomenon of load interactions during fatigue-crack growth is, therefore, important in damage-tolerant designs and residual-life assessments. The effect of the overloading [76] on the crack-propagation behavior during cyclic deformation has drawn much attention since its discovery in 1961 [77]. After the overload, there is a period of the crack-growth retardation, which is related to the magnitude [78–81] and number of overloads [76, 82, 83]. However, the stress/strain distribution at the crack tip after the overload, which leads to crack closure at even a tensile load and causes the crack-growth-rate retardation, is still not well understood.

The current explanations of the crack-closure phenomenon are listed below:

1. crack-tip blunting
2. crack deflection, branching, and secondary cracking,
3. crack-tip strain hardening or residual stresses ahead of the crack tip,
4. plasticity-induced closure,
5. roughness-induced closure,

6. oxide-induced crack closure,

7. transformation-induced crack closure,

8. viscous fluid induce crack closure.

The plasticity-induced closure can be understood as the plastic deformation of the material in the wake of the crack, which leads to the premature contact of the crack faces in the unloading sequence, resulting in the reduced cyclic-plastic deformation and, therefore, the decreased crack-propagation rate. This mechanism has received considerable supports in the fatigue community. There are many experimental results in the literature that attribute the retardation effects to the plasticity-induced crack closure [96–99]. Our results about this mechanism will be discussed.

The residual-strain measurement near the crack tip associated with the prior plastic deformation can help understand the crack-propagation behavior and the overload effect. In general, compressive residual strains/stresses are found to decrease the crack-propagation rates, while tensile residual strains/stresses increase the rates [100]. The investigation of the elastic and plastic deformation at the crack tip created by the prior loading can provide a measure of the crack-tip deformation. Therefore, a method for measuring residual stresses and the deformation surrounding a crack is useful for understanding the crack-growth behavior and crack-tip-deformation mechanism [96].

Neutron diffraction as a nondestructive-evaluation technique can determine the elastic lattice strains in a polycrystalline material from the shift of the diffraction peaks. At the same time, the plastic deformation can be related to the broadening

of the diffraction peaks. In the present investigation, lattice strains and diffraction peak-width changes near a fatigue crack in a compact-tension (CT) specimen were measured during monotonic tensile loading and unloading cycles using neutron diffraction to determine the effect of the overload.

In this chapter, a single-overload-imposed fatigue experimental results will be presented. The fatigue-striation measurements were performed, and striation spacings confirmed the crack-growth-rate result, i.e., the overload retards the crack propagation. Lattice strains and diffraction peak-width changes from neutron-diffraction experiments explain the plasticity-induced crack-closure phenomenon after the overload.

3.2 Experimental Details

3.2.1 Fatigue Experiments

The experiment was performed on a CT specimen of a Type 316 LN stainless steel, which is a nitrogen-added, low-carbon austenitic stainless steel. The chemical composition of a Type 316 low-carbon, nitrogen-added (LN) stainless steel (SS) (wt.%, weight percent) is shown in Table 1.1. A schematic of the CT specimen, with a width of 50.8 mm, a thickness of 6.35 mm, and a notch length of 10.16 mm, is shown in Figure 2.2.

The specimens were precracked to approximately 1.27 mm. The final stress-intensity-factor range (ΔK) used during precracking was 20 MPa$\sqrt{m}$. The precracking was performed at a R ratio of 0.1, using a triangular waveform with a

frequency of 10 Hz. Fatigue testing was performed at room temperature. The CT specimen was tested under a fatigue-loading condition using a Material Test System (MTS) electrohydraulic machine. Fatigue loading was performed in a load-control mode with a frequency of 10 Hz and a constant load ratio. Crack length grew from 12.7 mm to 30.38 mm. The final ΔK used during the fatigue test was 62.4 MPa$\sqrt{m}$. The fatigue crack was extended to 30.38 mm. The crack length was measured by the crack-opening-displacement (COD) gauge using the unloading-compliance technique [91]. An overload of 8,888 N was applied at the crack length corresponding to 22.88 mm. After the overload, the fatigue test resumes its previous experiment parameters.

3.2.2 Fatigue-Striation Measurements

Scanning-election microscopy was used to observe the fracture surface after the fatigue test. Along the crack-growth direction, at different crack lengths, several micrographs were taken. Fatigue striations at different crack lengths were investigated. The average spacing of striation can be calculated by dividing lengths of the lines, which were drawn along the striation-propagation direction on the micrographs, over the number of the striation through the lines. In general, as the stress-intensity increases, the crack-growth rate increases. The spacing between striations should increase, as crack growth rate increases, because the striation development is generally proportional to the crack-growth. The measurement of the striation spacing can help investigate the crack-growth rate.

3.2.3 Neutron-Diffraction Experiments

Neutron-diffraction measurements were performed, using the Spectrometer for Materials Research at Temperature and Stress (SMARTS) instrument of the Los Alamos Neutron Science Center (LANSCE). Utilizing the continuous energy spectrum of the incident neutron beam, the entire diffraction pattern (from 0.5 to 4 $\dot{A}$) was recorded in two stationary detector banks at fixed 2θ angles of $\pm$ 90°, which are with diffraction vectors along the in-plane and through-thickness directions, respectively. The incident neutron beam was defined by 2-mm horizontal and 1 mm vertical slits, and the diffracted beams were collimated, using 2 mm radial collimators, resulting in a 4 mm^3 gauge volume as shown in Figure 2.2. Thirty-two diffraction patterns were recorded along the crack length at a given applied load. The interatomic spacings in the in-plane direction (parallel to the loading direction) were determined by the Rietveld refinement of the diffraction patterns. Subsequently, the lattice strains were calculated using Equation 4.1. The values of the full-width-half-maximum (FWHM) as a function of scanning positions are measured. The peak-width change was determined, using Equation 2.2. The scan was repeated at seven different load values as shown in Figure 2.3.

In this chapter, the measurement results at load points 1 (667 N), 2 (3,333 N), 3 (6,667 N), 5 (8,889 N), 6 (6,667 N), and 7 (667 N) are presented. The load point 5 is an overload.

3.3 Results

3.3.1 Fatigue Experiments and Striation Measurements

After the load-controlled high-cycle fatigue experiment, the da/dN versus ΔK curve was plotted as shown in Figure 3.1. Paris [26, 32] showed that the fatigue-crack-growth increment, da/dN, is related to the stress-intensity-factor range by the power-law relationship:

$$\frac{da}{dN} = C(\Delta K)^m \tag{3.1}$$

where C and M are scaling constants. These constants are influenced by such variables as material microstructure, environments and temperatures, and load ratios, R. The exponent, m, in Equation 3.1 is typically between two and four. The data generated in this experiment observed the Paris law, with an m value of 3.25. Upon the application of an overload at the crack length of 22.88 mm, the crack-growth rate first increased exponentially for a very short crack length and then decreased. This reduction in the crack-growth rate continued until a minimum crack-growth rate was reached, after which the crack-growth rates began to increase. Eventually, at the crack length of around 24.6 mm, the crack-growth rate went back to the trend defined by Paris power law with the same parameters, C and m, as those before the overload was introduced. Finally the sample fractured at a crack length of 30.38 mm. As shown clearly in Figure 3.1, the Paris power law was observed during the entire experiment except for a period right after the overload, in which the retardation in the crack growth rate appeared at crack lengths from 22.88 to 24.6 mm.

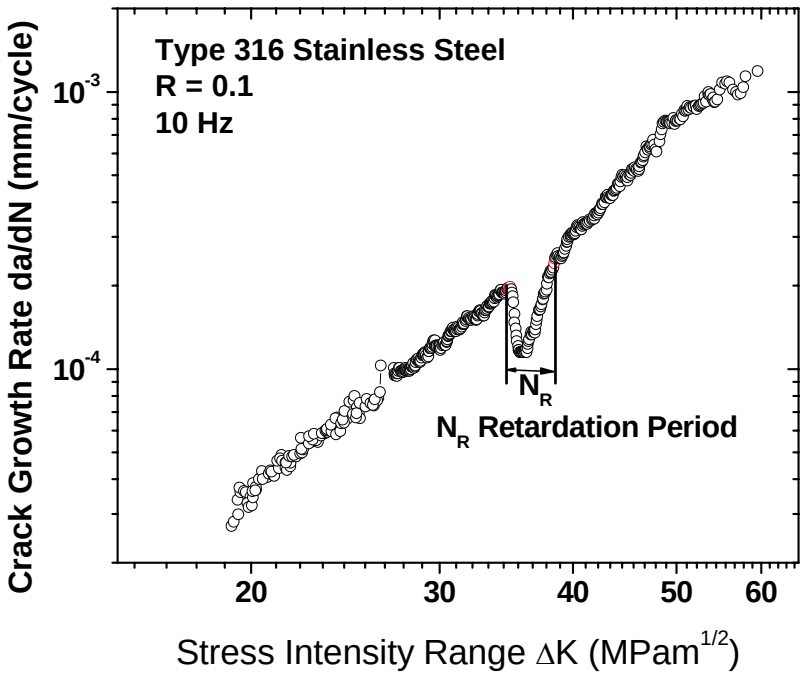


Figure 3.1: The load controlled high-cycle fatigue experimental result: crack-growth-rate curve.

Propagating fatigue cracks often leave their "footprints" on the fracture surface: fatigue striations. These striations are ripples on the fracture surface, as shown in Figure 3.2 . For cyclic loads in the Paris regime of the fatigue-crack advancement, it has been found that the spacing between adjacent striations correlates with the experimentally measured average fatigue crack-growth rate [101]. The striation spacing versus crack length curve in our study was plotted in Figure 3.3. A similar retardation period, as depicted in the da/dN versus ΔK curve (Figure 3.1), can be observed. Both the crack-growth-rate data and the fatigue-striation measurements indicated that the introduction of an overload led to a region with retarded crack-growth rates.

3.3.2 Lattice-Strain Measurements from Neutron Diffraction

Neutron-diffraction measurements were used to study the overload effect. Figure 3.4 shows the in-plane (IP) lattice-strain profiles measured at various applied loads (LP 1, 2, 3, and 4 in Figure 2.3). At 667 N (LP1), in the IP direction, small compressive strains with a maximum value of -194 x 10^{-6} were observed within $\pm$ 3 mm of the crack tip. The strains become tensile in front of the crack tip, reaching a maximum value of 526 x 10^{-6} (or $\mu\epsilon$) at approximately 5 mm from the crack tip, and then decreasing as the distance increases. At about 15 mm, the strains become compressive. When the load is increased from 667 N to 6,667 N (LP3), the maximum strain gradually increased. As the load decreased to 3,333 N (LP4), the maximum strain decreased. Figure 3.5 shows the through-thickness (TT) lattice-strain profiles measured at various applied loads (LP 1, 2, 3, and 4 in Figure 2.3). At 667 N (LP

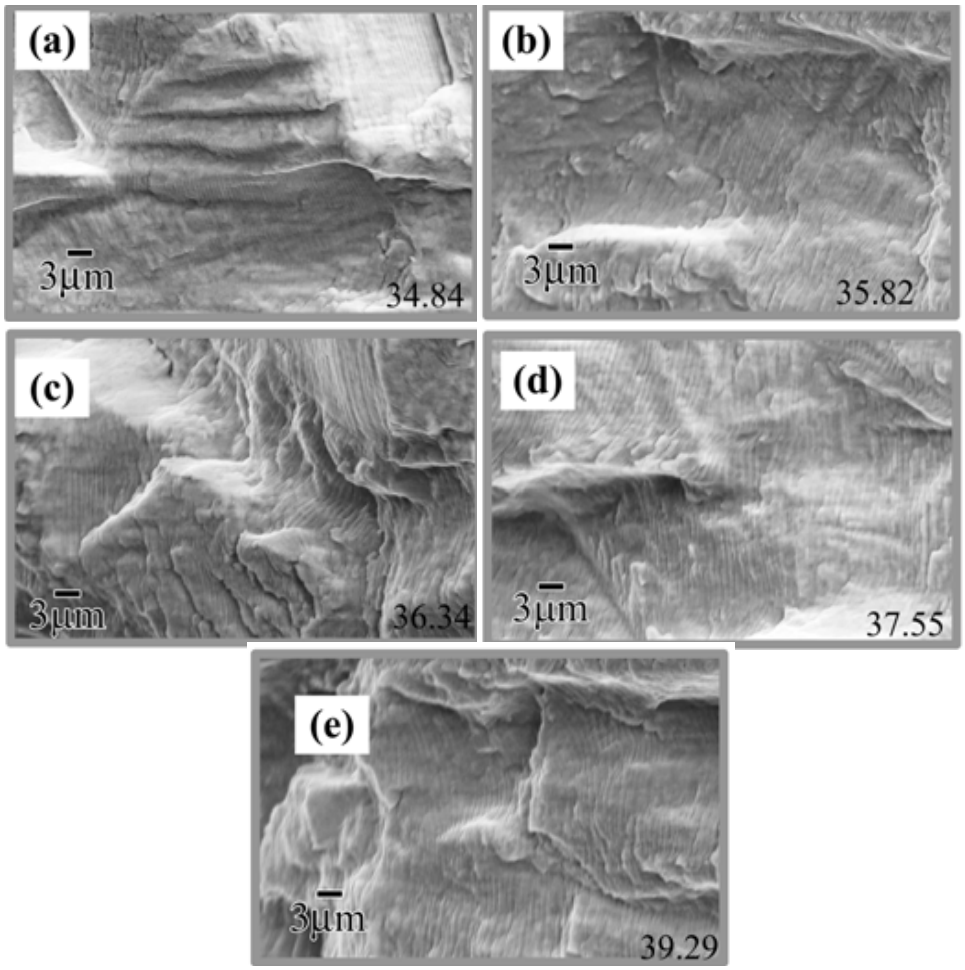


Figure 3.2: Fracture-surface image at different ΔK levels. (a) Fracture-surface image at ΔK of 34.84 $MPa\sqrt{m}$, (b) at ΔK of 35.82 $MPa\sqrt{m}$, (c) at ΔK of 36.34 $MPa\sqrt{m}$, (d) at ΔK of 37.55 $MPa\sqrt{m}$, and (e) at ΔK of 39.29 $MPa\sqrt{m}$.

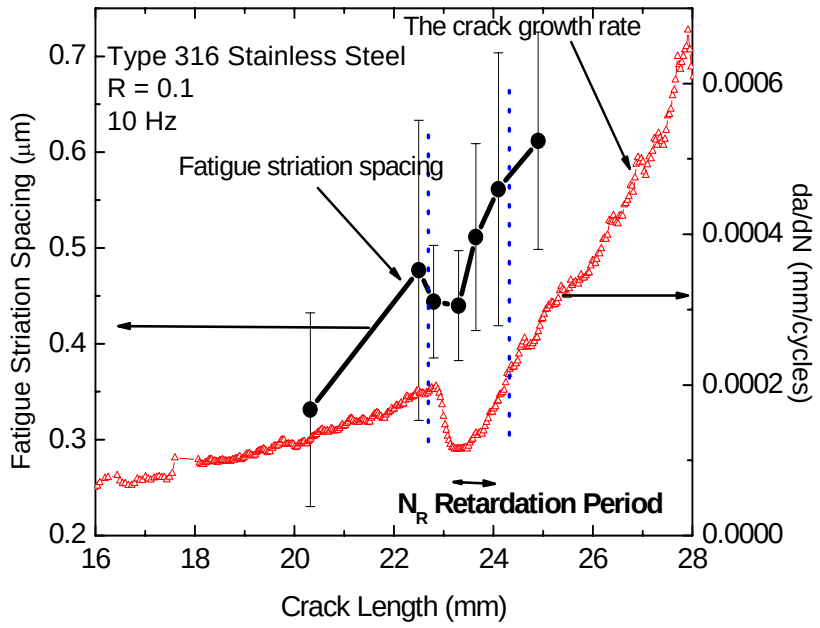


Figure 3.3: The comparison between the fatigue-striation spacing and the crack-growth rate at a function of the crack length.

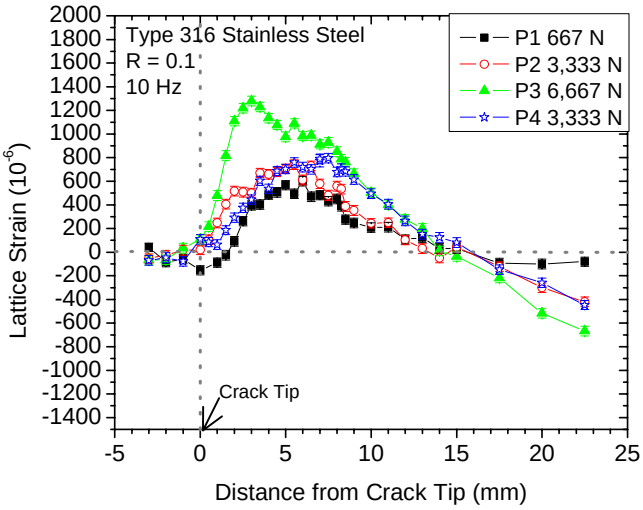


Figure 3.4: In-plane lattice-strain profiles in front of the crack tip at applied loads of 667 N, 3,333 N, 6,667 N, and 3,333 N, which correspond to LP1, LP2, LP3, and LP4 in Figure 2.3.

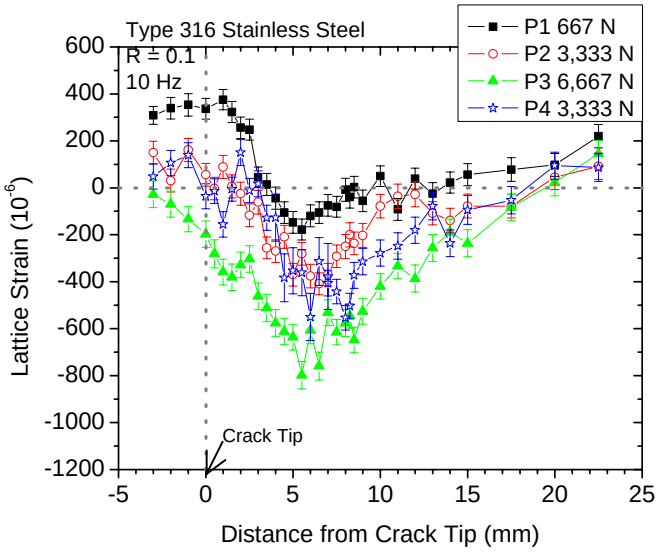


Figure 3.5: Through-thickness lattice-strain profiles in front of the crack tip at applied loads of 667 N, 3,333 N, 6,667 N, and 3,333 N, which correspond to LP1, LP2, LP3, and LP4 in Figure 2.3.

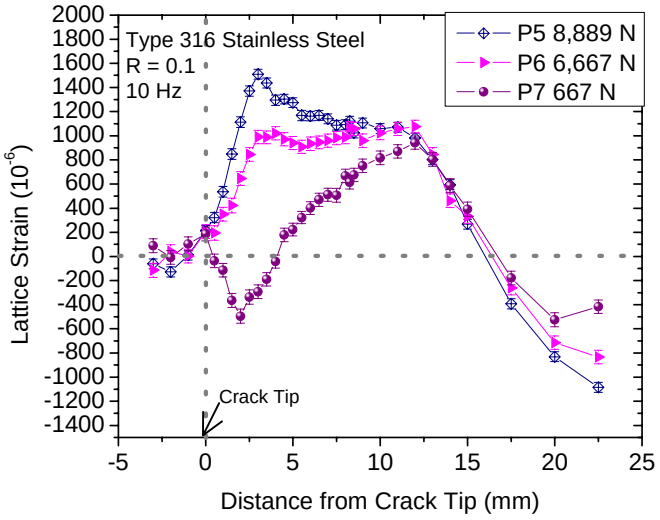


Figure 3.6: In-plane lattice-strain profiles in front of the crack tip at applied loads of 8,889 N, 6,667 N, and 667 N, which correspond to LP5, LP6, and LP7 in Figure 2.3.

1), tensile strains up to 300 x 10^{-6} were observed within ± 3 mm of the crack tip. The strains become compressive in front of the crack tip ranging from 3 mm to 15 mm from the crack tip. When the load is increased from 667 N to 6,667 N, the maximum compressive strains increased. As the load decreased to 3,333 N (LP4), the maximum compressive strain decreased. The signs of the lattice strains along IP and TT directions are opposite, which is mostly due to the Possion's effect.

The lattice-strain profiles in the IP direction in front of the crack tip as a function of the applied load after the overload at LP5 is presented in Figure 3.6. The maximum in the strain profile (at around 2 - 3 mm from the crack tip) diminished as the applied load was decreased from 8,889 N (LP5) to 667 N (LP7). At the tensile load of 667 N following the overload to 8,889 N, compressive lattice strains of up to - 600 $\mu\varepsilon$ were observed within 4 mm from the crack tip. The lattice-strain profiles along the

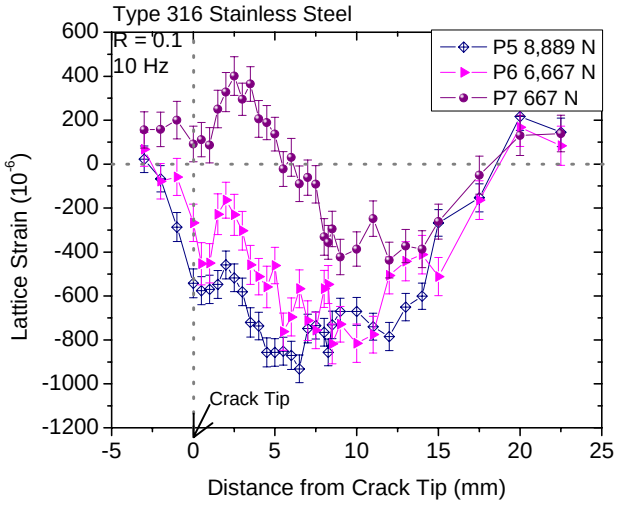


Figure 3.7: Through-thickness lattice-strain profiles in front of the crack tip at applied loads of 8,889 N, 6,667 N, and 667 N, which correspond to LP5, LP6, and LP7 in Figure 2.3.

TT direction at various applied loads (LP 5, 6, and 7) are presented in Figure 3.7 . As the in-situ loads increase the lattice strain values increased. At P_{min} of 667 N following the overload, tensile strains were observed in front of the crack tip.

3.3.3 Peak-Width-Change Variation from Neutron diffraction

The peak-width-change profiles in the IP direction as a function of the applied load are shown in Figures 3.8 and 3.9 . We had total 7 points neutron measurements, shown in Figure 2.3, at LP1 = 667 N, LP2 = 3,333 N, LP3 = 6,667 N, LP4 = 3,333 N, LP5 = 8,889 N, LP6 = 6,667 N, and LP7 = 667 N.

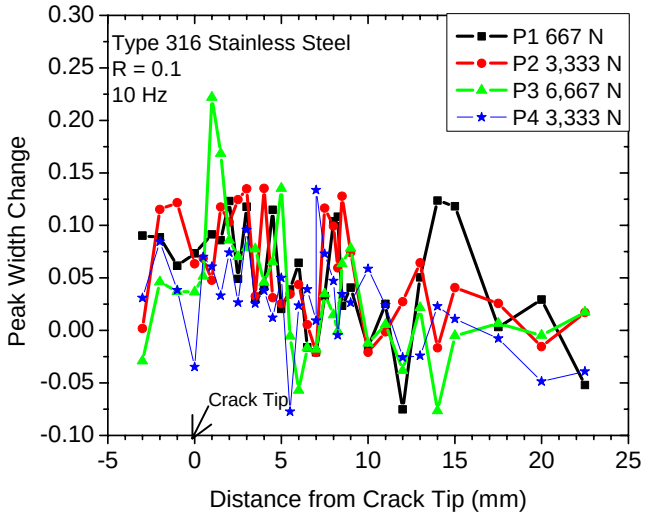


Figure 3.8: Peak-width-change profiles as a function of the distance from the crack tip at applied loads of 667 N, 3,333 N, 6,667 N, and 3,333 N, which correspond to LP1, LP2, LP3, and LP4 in Figure 2.3.

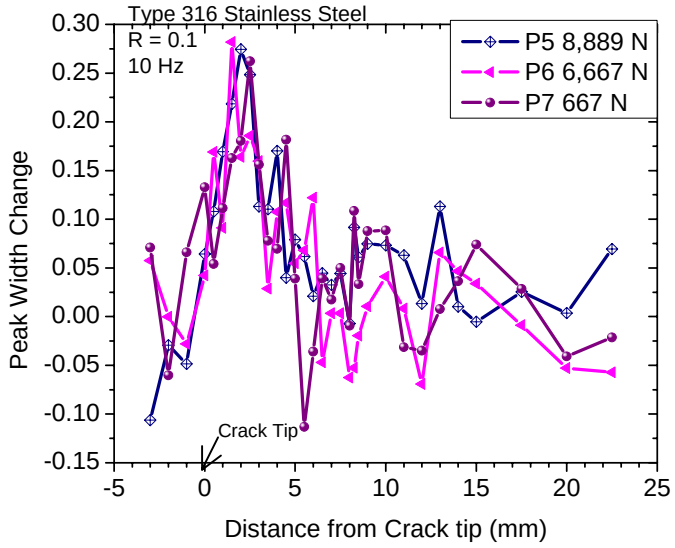


Figure 3.9: Peak-width-change profiles as a function of the distance from the crack tip at applied loads of 8,889 N, 6,667 N, and 667 N, which correspond to LP5, LP6, and LP7 in Figure 2.3.

The peak-width-change profiles at a function of applied loads at LP 1, 2, 3, and 4 are presented in Figure 3.8. As the load increased from 667 N to 6,667 N, the maximum peak-width-change value increased from 10 to 22.2 percents. At P3 of 6,667 N, it is obvious that the peak-width change is larger in front of the crack tip than far away from the crack tip.

The load decreased to 3,333 N, the maximum peak-width-change value decreased to 10 percent. From the peak-width change profiles in Figure 3.9, at loads of LP5, LP6, and LP7, the peak-width changes are large near the crack tip. As the load decreased from 8,889 N to 667 N, the maximum value in the peak-width-change profiles did not decease. The peak-width-change is irreversible. The maximum value is about 27 percents.

3.4 Discussion

3.4.1 Plasticity-Induced Crack Closure

The possibility that a fatigue crack can be close even at a far-field tensile load was first rationalized by Elber [40, 41] on the basis of experimental observations. Elber postulated that crack closure decreased the fatigue-crack-growth rate by reducing the effective stress-intensity-factor range. When a specimen is cyclically loaded at K_{max} and K_{min}, the crack faces are in contact below a stress-intensity value, K_{op}. The stress intensity range, $K_{op} - K_{min}$ does not contribute to fatigue-crack growth.

Constant-amplitude loading was interrupted by a single overload. Prior to the overload, the plastic zone would have reached a steady-state size, but the overload

cycle produced a significant larger plastic zone. When the load dropped to the original $P_{max.}$ and $P_{min.}$, the residual stresses that resulted from the overload plastic zone were likely to cause the crack closure and influence the subsequent fatigue behavior. In the crack-growth curve (Figure 3.1), a retardation period, running from crack lengths of 22.8 to 24.6 mm, was evident after the overload. The retardation period is also confirmed by the fatigue-striation measurements, as shown in Figure 3.3. The overload-induced the retardation of the crack-growth rate. The crack-propagation rate resumes its earlier power relationship with ΔK once the crack had grown through the overload plastic zone.

The crack-surface displacements are influenced by the plastic yielding at the crack tip and residual deformations left in the wake of the advancing crack. The applied load level, at which the crack surfaces become fully open (no surface contact), is directly related to the stress/strain distribution around a crack. Figures 3.10 shows a schematic of the Newman's model at maximum and minimum applied loads [9]. There are three regions: (1) a linear-elastic region containing a fictitious crack length, a, (2) a plastic region of the length C_p, and (3) a residual plastic-deformation region along the crack surfaces. The compressive plastic zone is w. The shaded region, in Figures 3.10 a and b, indicates the material, which is in a plastic state. The stress distributions at $P_{max.}$ and $P_{min.}$ along the crack line are shown. The large tensile plastic strain forms when the structure is loaded to $P_{max.}$. At $P_{min.}$, the material near the crack tip exhibits a reverse plasticity, which results in a compressive plastic zone. From the strain measurements by the neutron diffraction, the compressive strains in front of the crack tip were observed at the $P_{min.}$ loading (P1 and P7).

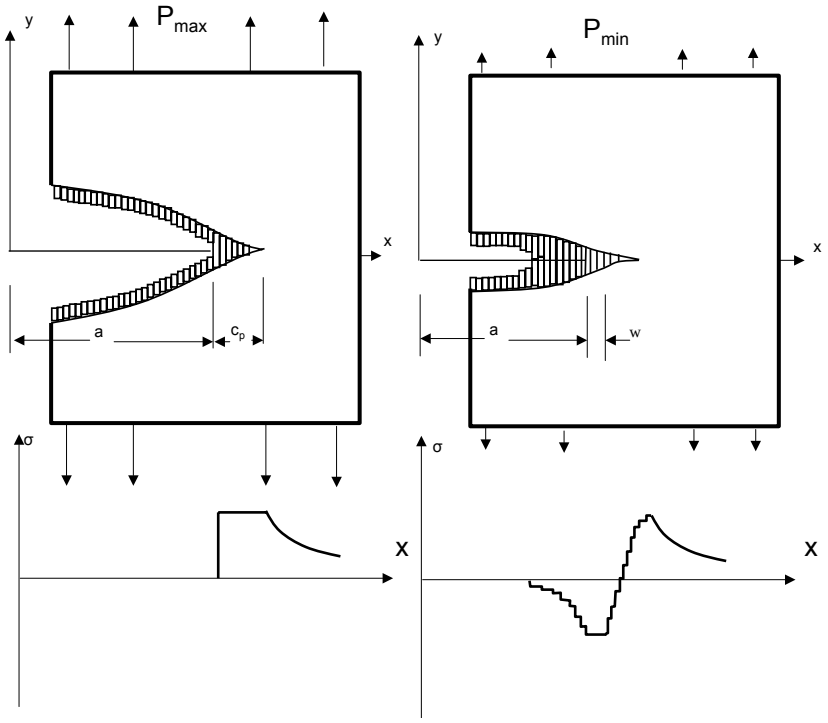


Figure 3.10: Crack-surface displacement and stress distributions along the crack line. [9]

The overload induces the significant large plastic zone and the attendant fracture-surface contact, which causes the reversed plastic-zone size increasing, and the compressive stress/strain within the reversed plastic zone increasing. From the comparison of the lattice strains plots at $P_{min.}$ of P1 and P7, larger compressive strains were observed at P7 (after the overload). The compressive stress fields at the crack tip influences the subsequent deformation and the crack growth. As the fatigue crack propagates through the overload-induced plastic zone, the two fracture surfaces contact and the reversed plastic zone cause an enhancement at the level of the plasticity-induced crack closure in the post-overload regime, which, in turn, promotes a retardation of growth rates [74, 102].

3.4.2 Plasticity in Front of the Crack Tip

In general, the diffraction peak-width change are due to many factors:

- Type 1 macroscopic stresses (the stress distribution averaged in the gauge volume),
- Type 2, anisotropic polycrystalline intergranular stresses (resulting from large differences in the stress/strain levels between different families of grains with different lattice orientations),
- Type 3, plastic deformation,
- Instrument broadening, small grain size (e.g., nano particles).

The peak-width-change profiles as a function of the distance from the crack tip are presented. As the in-situ load increased from 667 N to 6,667 N, the peak-width change

increases. After the load decreased to 3,333 N, the peak-width change decreased, indicating that the peak-width change is due to mostly macroscopic stresses and intergranular stresses (Types I and II). The reason is that the peak-width change varied with the in-situ loading. In another word, the deformations from LP1 to P4 are recoverable. At loads of LP1, LP2, and LP4 (Figure 3.8), the peak-width changes do not vary with the distance from the crack tip, even though there are plastic deformations induced by the fatigue. The plastic deformations around the crack tip left by fatigue experiments were not large. However, in the lattice-strain profiles (Figure 3.8), there are larger lattice strains near the crack tip than far away from the crack tip.

At the overload of 8,889 N, the peak-width change is large in front of the crack tip. As the following in-situ loads decreased to 667 N, the maximum of the peak-width change in front of the crack tip did not decrease. The peak-width change after the overload is due to the plastic deformation (Type III). The reason is that the large amount of the overload induced plastic deformation around the crack tip (the applied overload increased K_{max} from 38.8 to 51.6 MPa$\sqrt{m}$ at the same crack length). The plastic deformation is so large that the plastic-deformation effect is larger than the macroscopic-stresses effects or the intergranular stress effects. We believe that the large plastic deformation induces the compressive strain in front of the crack tip, which caused the crack closure, and the crack-growth rate decreased. From the region where the peak-width change is large, we can also estimate the plastic-zone size. The plastic-zone size after the overload is about 7 - 9 mm [103].

3.5 Conclusion

- During fatigue experiments with a single overload imposed, the crack-growth-retardation period was observed after the overload. The retardation period was confirmed by the measurement of the striation-spacing changes before and after the overload.

- The neutron-diffraction results showed the evolution of lattice-strain profiles associated with the in-situ applied loading as well as the residual-strain profile generated by an overload. After the overload, a significant compressive strain of - 600 $\mu\varepsilon$ (or x 10^{-6}) was observed in front of the crack tip, which was related to the crack-closure phenomenon and retardation of crack growth.

- The neutron-diffraction results showed the evolution of the peak-width-change associated with the in-situ applied loading. The overload-induced irreversible large plastic deformation was observed from the large peak-width change in front of the crack tip after the overload.

- The lattice-strain and peak-width-change profiles measured by neutron diffraction confirm the plasticity-induced crack-closure phenomenon.

Chapter 4

Multiscale Plastic Deformation Near A Fatigue Crack From Diffraction

4.1 Introduction

For common engineering applications, variable-amplitude loading is often much more realistic than constant-amplitude loading as the cause of fatigue failures. The ability to quantitatively predict the phenomenon of load interactions during fatigue-crack growth is, therefore, important in damage-tolerant designs and residual-life assessments. The effect of overloading on the crack-propagation behavior during cyclic deformation has drawn much attention since its discovery in 1961 [31]. However, the phenomenon is still not well understood. The retardation of the crack-growth

behavior can be understood in the context of the plasticity-induced crack-closure mechanism. The plastic deformation of the material in the wake of the crack leads to the premature contact of the crack faces in the unloading sequence, resulting in the reduced cyclic-plastic deformation and, therefore, the decreased crack-propagation rate. Near the crack tip, the plastic deformation is not uniform. External loads will give rise to a non-uniform stress and strain state near the crack tip. The resulting residual stresses and strains can be either beneficial or detrimental, depending on the magnitude and sign. In general, compressive residual strains/stresses are found to decrease the crack-propagation rates, while tensile residual strains/stresses increase the rates [84].

Measuring the residual strains near the crack tip helps understand the crack-propagation behavior and investigate the overload effect. Furthermore, the study of the plastic deformation at the crack tip created by prior loading can provide a measure of the severity of the deformation around the crack tip. Therefore, a method for measuring residual stresses and plastic deformations surrounding a crack is useful for understanding the crack-growth behavior and the crack-tip deformation mechanism [85].

Neutron diffraction as a nondestructive-evaluation technique has a great penetrating power. Therefore, measurements using the neutron method are not restricted to surface locations. Neutron diffraction provides a unique technique for determining the elastic lattice strains in a polycrystalline material from the shift of the diffraction peaks. At the same time, the plastic deformation can be estimated from the broadening of the diffraction peaks.

In addition, the polychromatic x-ray microdiffraction (PXM) can provide a submicron spatial resolution, which is an excellent technique for mapping the deformation around the crack tip at the mesoscale. The development of unltrabrilliant third-generation synchrotron x-ray sources and the recent progress in x-ray optics have led to the intense x-ray beam. Together with the new instrumentation, it is possible to use the Laue method to quantitatively determine the elastic strain and the local orientation distribution in individual grains or subgrains. The Laue spot is sensitive to the grain orientation, unit-cell shape, and deformation, which can provide the precise information on the phase, grain orientation, and morphology of polycrystalline materials. As a polychromatic x-ray beam penetrates a sample, the x-ray produces a Laue pattern from each subgrain that it intercepts. The quantitative information on the number and kind of unpaired random dislocations can be recovered from streaking in Laue images.

In this chapter the deformation near a crack tip was investigated using diffraction methods in multi-scales, neutron diffraction and PXM measurements. The lattice strain and broadening of the scattered intensity distribution results were obtained from neutron measurements. The Laue patterns at different locations around the crack tip were measured. Three issues are examined: (1) The compressive lattice-strains were analyzed, which contain the information about the crack-closure phenomenon; (2) The dislocation density near the crack tip was determined before and after the overload; and (3) The inhomogeneous plastic deformation was investigated from the streaking of the Laue patterns.

4.2 Experimental Details

The fatigue experiment was performed on a compact-tension (CT) specimen, with a width of 50.8 mm, a thickness of 6.35 mm, and a notch length of 10.16 mm, of a Type 316 low-carbon nitrogen-added (LN) austenitic stainless steel. The CT specimen was pre-cracked under a fatigue-loading condition using a Material Test System (MTS) electrohydraulic machine. Fatigue loading was performed in a load-control mode with a frequency of 10 Hz and a constant load ratio, R = 0.1, where $R = P_{min.}/P_{max.}$ $P_{min.}$ and $P_{max.}$ are the applied minimum (667 N) and maximum (6,667 N) loads, respectively. The maximum stress intensity, K_{max}, reached 38.8 MPa during fatigue-crack growth.

Neutron-diffraction measurements were performed using the Spectrometer for Materials Research at Temperature and Stress (SMARTS) [92] of the Los Alamos Neutron Science Center (LANSCE). Utilizing the continuous energy spectrum of the incident neutron beam, the entire diffraction pattern (d spacings ranging from 0.5 to 4 $\mathring{A}$) was recorded in two stationary detector banks at fixed diffraction angles (2θ) of $\pm$ 90°, Figure 4.1. The sample (a view of the sample is shown in Figure 4.1) was aligned such that the tensile load axis was oriented 45° from the incident beam, and, thus, the diffraction vectors associated with the two detector banks were parallel to the in-plane (IP) and through-thickness (TT) directions of the sample. The incident neutron beam was defined by 2 mm and 1 mm (along the crack-length direction) slits, and the diffracted beams were collimated using 2-mm radial collimators, resulting in a 4 mm^3-gauge volume. In-situ tensile loadings were applied. The loads range from the

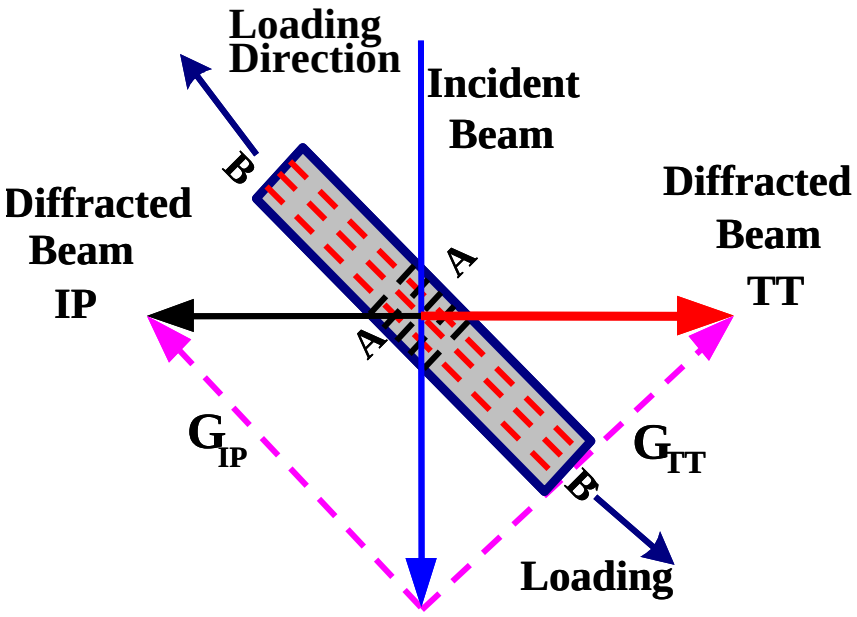


Figure 4.1: Schematic of a neutron-diffraction experiment

minimum load of 667 N to the overload of 8,889 N. At each in-situ loading, thirty-two diffraction patterns were recorded along the crack-length direction at a given applied load. The interatomic spacing in the IP direction (parallel to the loading direction) and in the TT direction were determined by the Rietveld refinement [93] of the diffraction patterns. Subsequently, the lattice strains, ε, were calculated from

$$\varepsilon = \frac{a - a_0}{a_0} \tag{4.1}$$

where the stress-free lattice parameter, a_0, was measured at a reference point away from the crack tip.

PXM was performed with a focused polychromatic synchrotron beam, which intercepts the sample surface in an area of 0.5 μm in diameter at a 45° incidence. As the polychromatic beam penetrates the sample, the x-ray produces a Laue pattern in each subgrain that it intercepts. The penetration length depends on the atomic number of the material, and for steel samples, it is about 30 μm. The overlapping Laue patterns are detected by an x-ray-sensitive Charged-Coupled Device (CCD) positioned at 90° to the incident beam [104–106].

4.3 Results and Discussions

The dependence of lattice-strain components on the distance from the crack tip measured in IP direction under in-situ tensile loading of 667 N after the fatigue and overload deformations is plotted in Figure 4.2. After the fatigue deformation, compressive strains (up to -150 $\mu\varepsilon$) near the crack tip was observed. The tensile strain

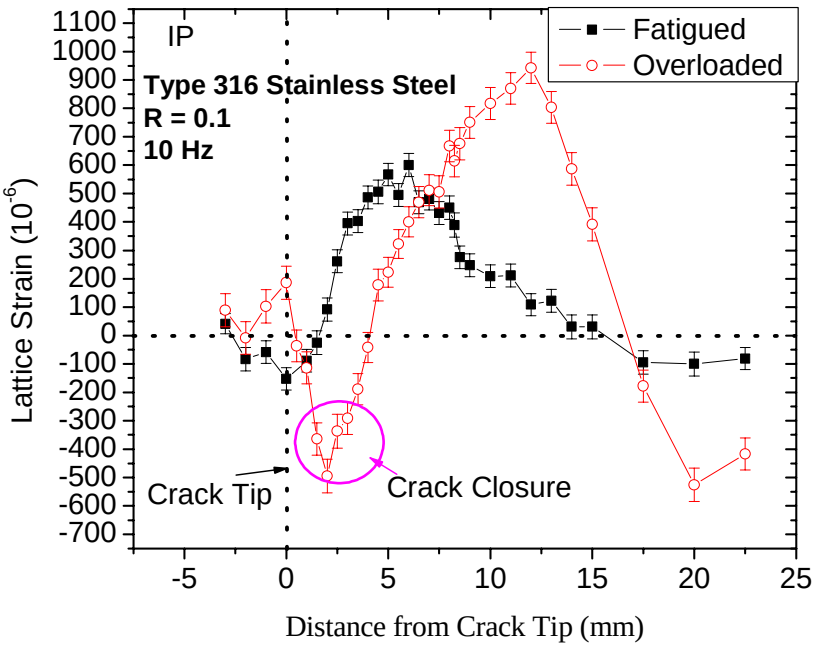


Figure 4.2: Lattice-strain profiles at in-situ loading of 667 N after the fatigue and overload deformation along the IP direction

exists ranging from 2 mm to 15 mm from the crack tip, and the maximum tensile strain is about 600 x 10^{-6} (or $\mu\varepsilon$). After the overload, there is a large compressive strain field (up to - 600 $\mu\varepsilon$), ranging from 0 mm to 5 mm from the crack tip. The tensile strain exists ranging from 5 mm to 17 mm from the crack tip. The maximum tensile strain reaches about 900 $\mu\varepsilon$. After the fatigue deformation, the small compressive strains near the crack tip are due to the reversed plastic deformation induced by fatigue deformation. After the overload deformation, the overload-induced large plasticity near the crack tip. The large compressive strain in front of the crack results from the large plastic deformation induced by the overload. The compressive strains in front of the crack tip can retard the crack propagation rate and increase the fatigue life [103].

Elber [40, 41] first discovered the fatigue-crack closure and brought to light the very dependence of fatigue-crack-growth rates on the prior history. The overload induced the large plastic deformation near the crack tip. The severity of the plastic deformation can be estimated by observing the diffraction-peak-width changes. For randomly-distributed dislocations, the broadening can be expressed by

$$2\delta q_{hkl} \propto \frac{\pi C_{hkl} b}{d_{hkl}} \sqrt{n} \tag{4.2}$$

where d_{hkl} is the d-spacing of the (hkl) reflection, b is the Burger's vector, 2 q_{hkl} is the FWHM along the diffraction vector (G_{IP} and G_{TT} for IP and TT directions, respectively, Figure 4.1), n is the total density of randomly distributed dislocations, and C_j is the orientation factor [107, 108] corresponding to the (hkl) reflection. If the dislocations are randomly distributed, FHWM should linearly increase as $1/d_{(hkl)}$

increases. The profiles for FWHM as a function of $2\pi/d$ for four reflections, (111), (200), (220), and (311) along the IP direction are plotted in Figure 4.3. For each reflection, the FWHM values are obtained over a range of -5 to 25 mm from the crack tip. In Figure 4.3. the results for only four positions are presented, including the distances of 0, 2, 5, and 10 mm from the crack tip. The linear dependence of the averaged FWHM on $2\pi/d$, which is predicted by the Equation 4.2, was experimentally observed for the IP direction. The estimated dislocation density, n, relative to the reference point along the IP diffraction direction was calculated from the peak-width change. The dislocation density in the IP direction as a function of the distance from the crack tip at the in-situ loads of 667 N following the fatigue load and overload are plotted in Figure 4.4. . The averaged dislocation density following the fatigue load is about 0.3 x 10^{10} cm^{-2}. After fatigue, the dislocation density does not change as a function of the distance from the crack tip at the microscale. In contrast, after the overload, the dislocation density near the crack tip is much higher than that after the fatigue load, and the change in the dislocation density is clearly observed after the overload. The maximum dislocation density reached 3.5 x 10^{10} cm^{-2} at 2.5 mm from the crack tip. The increased dislocation density is due to the large plastic deformation occurring in front of the crack tip due to the overload. The large plastic deformation induced by the overload caused the compressive strains in front of the crack tip, which, in turn, retard the crack-propagation rate. In contrast, the polychromatic X-ray microbeam provides the local structural information around the crack tip. While the FWHM of neutron measurements depends on the square root of the total dislocation density, the length of the streak of the Laue pattern depends mainly on the

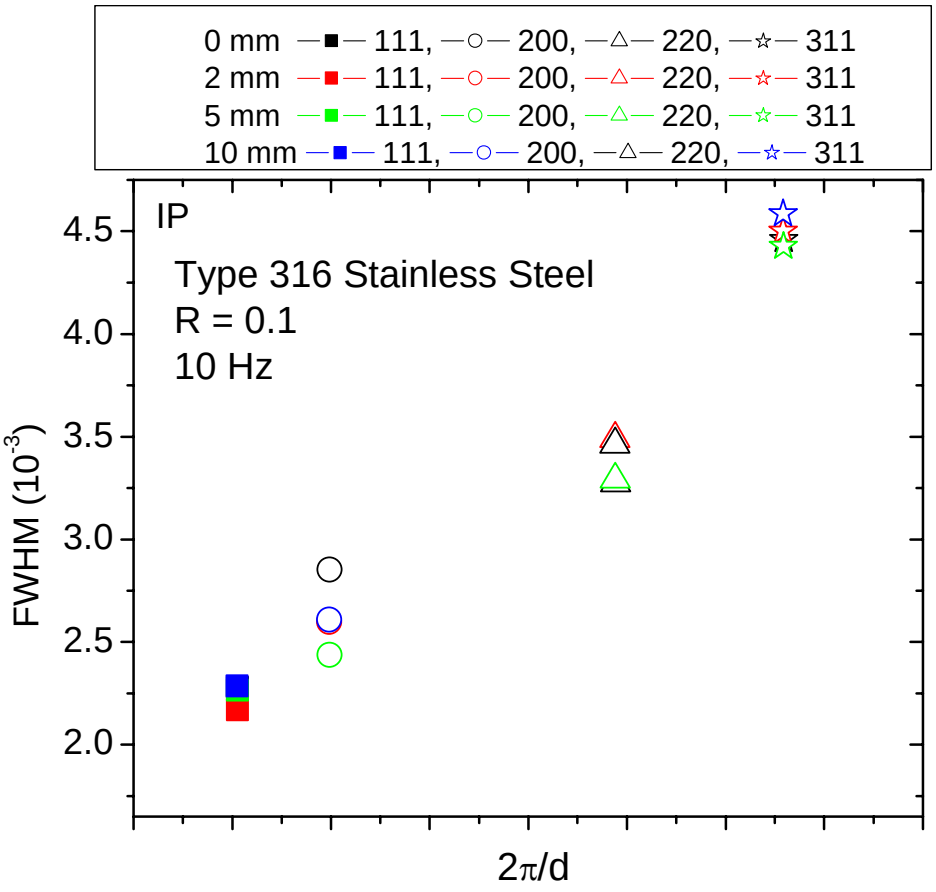


Figure 4.3: The dependence of FWHM on $2\pi/d$ for four types of $< hkl >$ at different distances from the crack tip

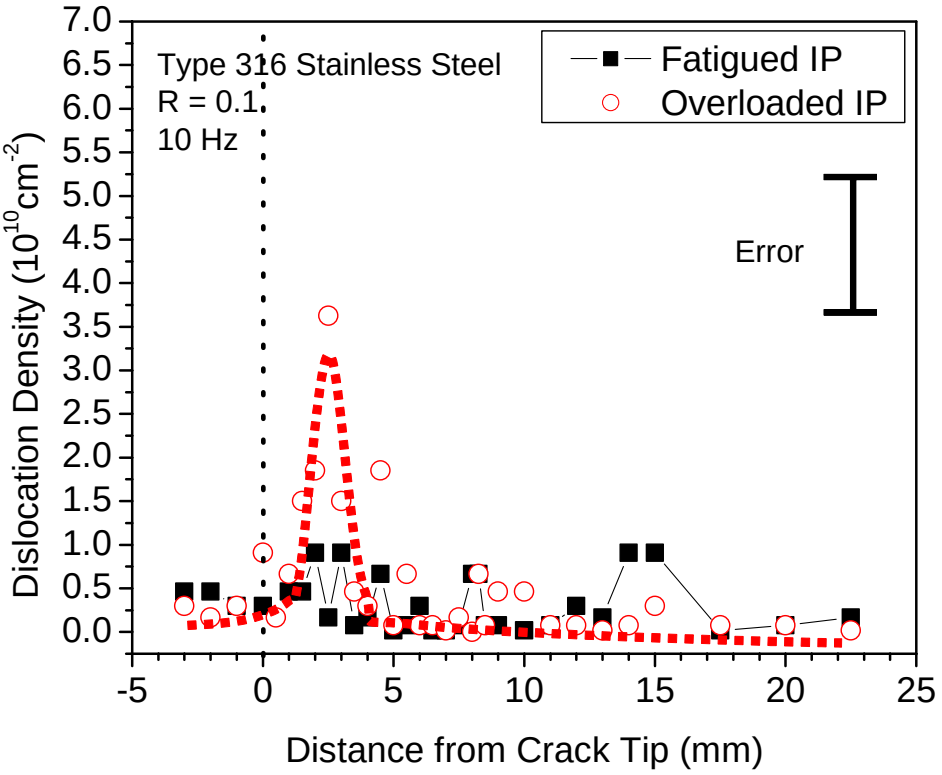


Figure 4.4: Dislocation density as a function of the distance from the crack tip

number of geometrically necessary dislocations (GNDs) within the irradiated volume (about 0.5 diremeter), causing local lattice rotations [104]. Figure 4.5 shows the Laue patterns obtained at different locations near the crack tip. The analysis of these Laue patterns demonstrates that the plastic deformation results in the formation of the alternating regions with high and low GND densities. Some of the patterns consist of relatively sharp spots corresponding to grains with a relatively low GND density. At the same time, some of the patterns show intensive "streaking" of all Laue spots. Such streaking is indicative of the strong lattice curvature in these grains. The length of streaks characterizes the total lattice rotation in the probed region of the grain. In one gauge volume, the severely-deformed grains are found neighboring with wildly deformed ones. The quantitative dislocation-density distributions near the crack tip can be obtained from the microbeam diffraction, and the results will be presented in a future publication.

4.4 Summary

1. The elastic-strain profiles in the IP direction reveal the crack-closure phenomena.

2. A higher dislocation density was observed near the crack tip after the overload, which indicates the plasticity-induced crack closure.

3. The inhomogeneous plastic deformations at a mesoscale ($\sim$ 1 μm) were observed using the synchrotron PXM. Neighbor grains were deformed differently, depending on their crystallographic orientation, size, and surroundings.

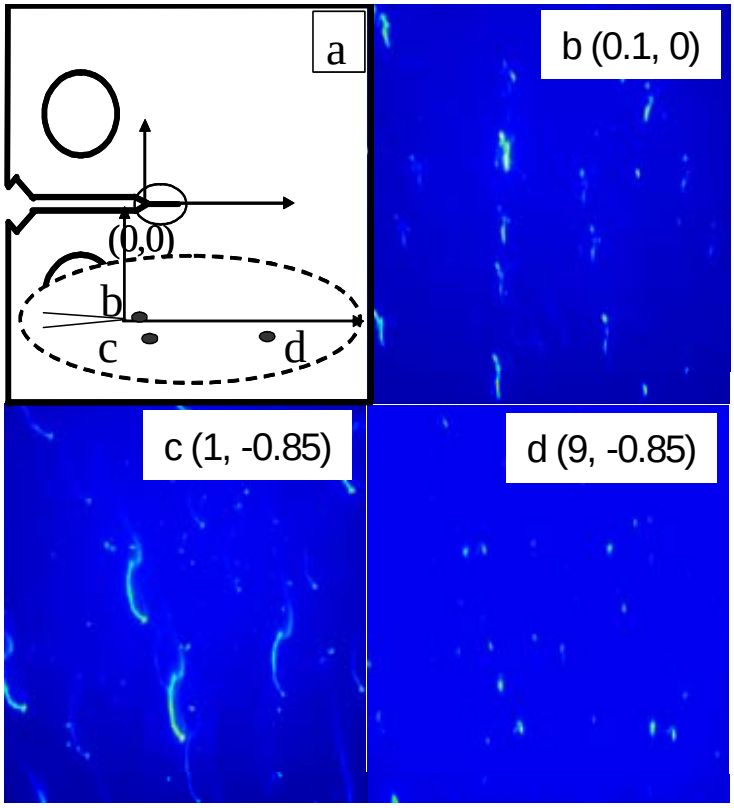


Figure 4.5: Laue patterns obtained at different locations near the crack tip, (a) mapping sketch, (b) Laue pattern at (0.1 mm, 0 mm), (c) Laue pattern at (1 mm, - 0.85 mm), and (d) Laue pattern at (9 mm, - 0.85 mm)

Chapter 5

Neutron-Diffraction Study and Cohesive-Interface Model of Fatigue-Crack-Deformation Behavior

5.1 Introduction

It is of critical importance to be able to predict the growth rate of a fatigue crack for the damage-tolerant designs and residual-life assessments [76]. The commonly used constant-amplitude loading profile in fatigue tests is not sufficient to address the complicated working conditions in service. It was found that a single overload in the fatigue-loading history could result in a period of crack-growth retardation, which can

be understood in the context of the plasticity-induced crack-closure mechanism [47–49,49,78–80,88–90,109]. Measurements of the elastic and plastic strain distributions near the crack tip can provide an experimental basis for the development of predictive models of fatigue-crack-propagation behavior. However, owing to the small plastic-zone size, direct measurements are a challenging task, so that the understanding of the fatigue-overload effects remains largely qualitatively in nature.

This work aims to study the elastic/plastic strain distributions around a fatigue crack by the neutron-diffraction (ND) technique and a cohesive-interface model. Because of the deep penetration capability of neutron beams, the ND technique allows bulk measurements with a typical spatial resolution on the order of millimeter. Volume-averaged elastic-lattice strains in a polycrystalline material under residual or applied stresses can be determined from the shift of the diffraction peaks [94,110–113], and the dislocation density can be estimated from the broadening of the diffraction profiles [85, 114, 115]. The measured lattice strains and dislocation densities will be compared to the finite-element simulations that are based on an irreversible, hysteretic-cohesive interface model [67,73,116,117]. The experimental and numerical results will be compared and discussed.

5.2 Experimental Details

The material used in this study is a 316 stainless steel. Compact-tension (CT) specimens (with a width of 50.8 mm and a thickness of 6.35 mm) were machined and fatigue tested with a frequency of 10 Hz. The maximum and minimum loads are 6,667

N and 667 N, respectively. When the crack length reached 22.8 mm, an overload of 8,889 N was applied. ND measurements were performed using the Spectrometer for Materials Research at Temperature and Stress (SMARTS) at the Los Alamos Neutron Science Center (LANSCE) [92]. The CT specimens were aligned such that the tensile load axis was 45 from the incident beam and, thus, the diffraction vectors associated with the two detector banks were parallel to the in-plane (IP) (parallel to the loading direction) and through-thickness (TT) directions of the sample. The incident neutron beam was defined by 2 mm and 1 mm (along the crack length) slits, and the diffracted beams were collimated using 2 mm radial collimators, resulting in a 4 mm^3 gauge volume. Thirty-two diffraction patterns were recorded along the crack length, as shown in the inset of Figure 5.1. The interatomic spacings were determined by the Rietveld refinement [93] of the diffraction patterns. The lattice strains caused by the fatigue deformation and overloading,

$$\varepsilon = \frac{a - a_0}{a_0} \tag{5.1}$$

where a_0, the stress-free lattice parameter, was measured away from the crack tip. The lattice strains (ϵ), were obtained along both IP and TT directions, where a is the lattice parameter, and a_0 is a "stress-free" reference measured at the corner of the CT specimen. Furthermore, diffraction-peak broadening was measured along both IP and TT directions. Here we only report the results along the IP direction.

The severity of the plastic deformation can be estimated from the ND measurements by observing the broadening of the diffraction-peak-width change. The estimated changes in the dislocation density, n, due to the fatigue deformation and

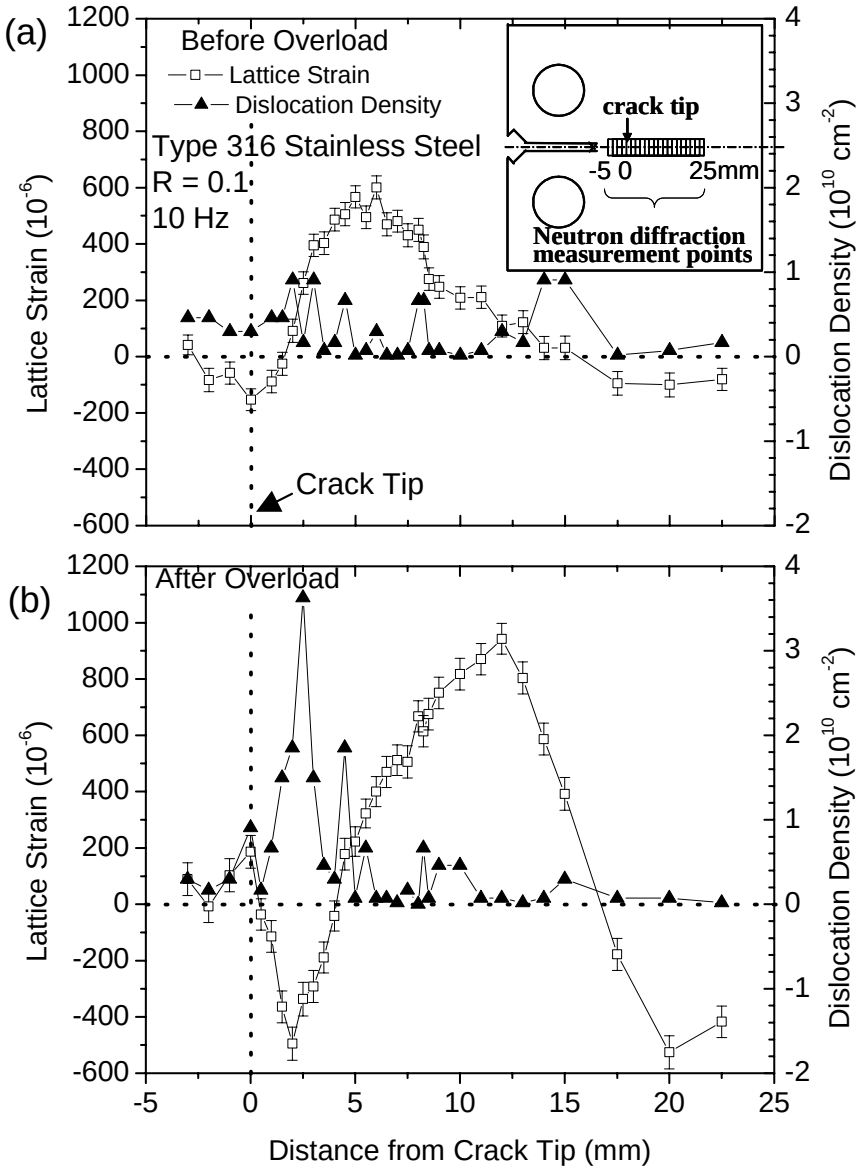


Figure 5.1: Elastic-lattice-strain and dislocation-density distributions at the minimum loads immediately before and after the overload, in (a) and (b), respectively. The inset shows the neutron-measurement positions behind and in front of the crack tip.

overloading relative to the reference point can be calculated by

$$n = \frac{3619(FWHM - FWHM_0)^2(1-\upsilon)^2}{b^2G^2[29 - 76\upsilon + 72\upsilon^2 - (1 + 4\upsilon - 24^2]} \tag{5.2}$$

where $FWHM$ is the full-width-half maximum of the diffraction peaks measured along the crack-length direction, $FWHM_0$ is the full-width-half maximum at the reference point at the corner of the CT specimen, υ is Poisson's ratio, b is the magnitude of the Burgers vector, and G is the diffraction vector.

5.3 Results and Discussions

The lattice-strain and dislocation-density profiles at $P_{min.}$ of 667 N along the IP direction are shown in Figures 5.1 (a) and (b), for the cycles immediately before and after the overload. In Figure 5.1(a), small compressive strains (with a maximum of - 200×10^{-6}) are observed within about 3 mm around the crack tip. The small compressive strain is due to the elastic unloading. The dislocation-density distribution varies slightly without a significant trend as a function of the distance from the crack tip. The averaged dislocation density, about $0.3 \times 10^{10} cm^{-2}$, is a small difference relative to the reference point. After the application of the overload, Figure 5.1(b), the compressive lattice strains of up to - 600×10^{-6} are observed within about 4 mm in front of the crack tip. Had it not been for the overload, the corresponding lattice strain and dislocation-density curves in the next cycle would have shown little difference from those shown in Figure 5.1(a). Consequently, the large compressive

strains in front of the crack tip strongly suggest the crack-closure phenomenon associated with the overload. The dislocation-density distribution profile shows a much higher value near the crack tip than that in Figure 5.1(a). The maximum dislocation density reaches $3.5 \times 10^{10} cm^{-2}$ at 2.5 mm from the crack tip. The high dislocation density is due to the large plastic deformation occurring in front of the crack tip during the overload. The overload-induced large plastic zone will retard the crack propagation, because the crack has to grow out of such plastic zone to resume a steady-state growth [74, 103, 118]. Tensile strains between 4 and 16 mm in front of the crack tip are observed, and at about 16 mm, the strains become compressive because of the finite specimen size.

An irreversible, hysteretic cohesive model has been implemented into the commercial FEM software, ABAQUS, through a user-define element (UEL) subroutine. In this model, the crack is modeled by a set of cohesive interface elements, which separate according to the constitutive equations relating the tractions acting on the two bonded solids to the separation between them. The nucleation and propagation of the crack are the natural result of the finite-element simulation; no ad hoc fracture criterion is required. The introduction of the hysteresis and irreversibility allows the fatigue crack to grow under an applied stress-intensity-factor range that is smaller than the intrinsic fracture toughness, which is determined from the area underneath the traction-separation curve. The traction, T_n, and separation, Δ_n, are related by

$$T_n = \sigma_{max} \frac{\Delta_n}{\delta_n} exp(1 - \frac{\Delta_n}{\delta_n}) \tag{5.3}$$

where T_n is the traction, Δ_n is the separation, $\sigma_{max} = 800$ MPa and $\delta_n = 1$ μm in this study.

During unloading and reloading, the interface stiffness evolves according to a set of damage equations, which largely follows the model in [73]. The surrounding material is modeled by the elastic-perfectly plastic behavior, with the elastic modulus E = 210 GPa, Poisson's ratio $\upsilon = 0.3$, and yield stress $\sigma_Y = 288$ MPa. A total number of 800 fatigue cycles is applied, and at the 400^{th} cycle, an overload of 1.33 P_{max} was imposed during the constant-amplitude-fatigue experiment.

In Figure 5.2, the FEM simulations show the evolution of the elastic and plastic strain distributions before and after the overload. The insets are the corresponding two-dimensional plastic strain (i.e., ε_{22}^p, where ε_{22} denotes the strain along the IP direction) contours. It should also be noted that, to illustrate the results, the abscissa is normalized by the crack-tip location, x_{tip}, stress-intensity factor, K, and the yield strength, σ_y. Results in Figures 5.1 and 5.2 show a good qualitative agreement. The plastic-strain profile changes considerably from the cycle before the overload to the one after the overload. This comparison indicates the occurrence of the overload-induced plastic zone, which correspond to the large increase of dislocation densities observed in Figure 5.1(b). The elastic-strain distribution after the overload reveals a discontinuity near the crack tip. Evidently, the application of the overload produces a large plastic zone. During unloading, this plastic zone tends to maintain its permanent deformation, while the surrounding elastic-deformation zone tends to shrink. Consequently, a large compressive strain will be superposed onto this zone, leading to the discontinuity of the elastic-strain distribution near the crack tip.

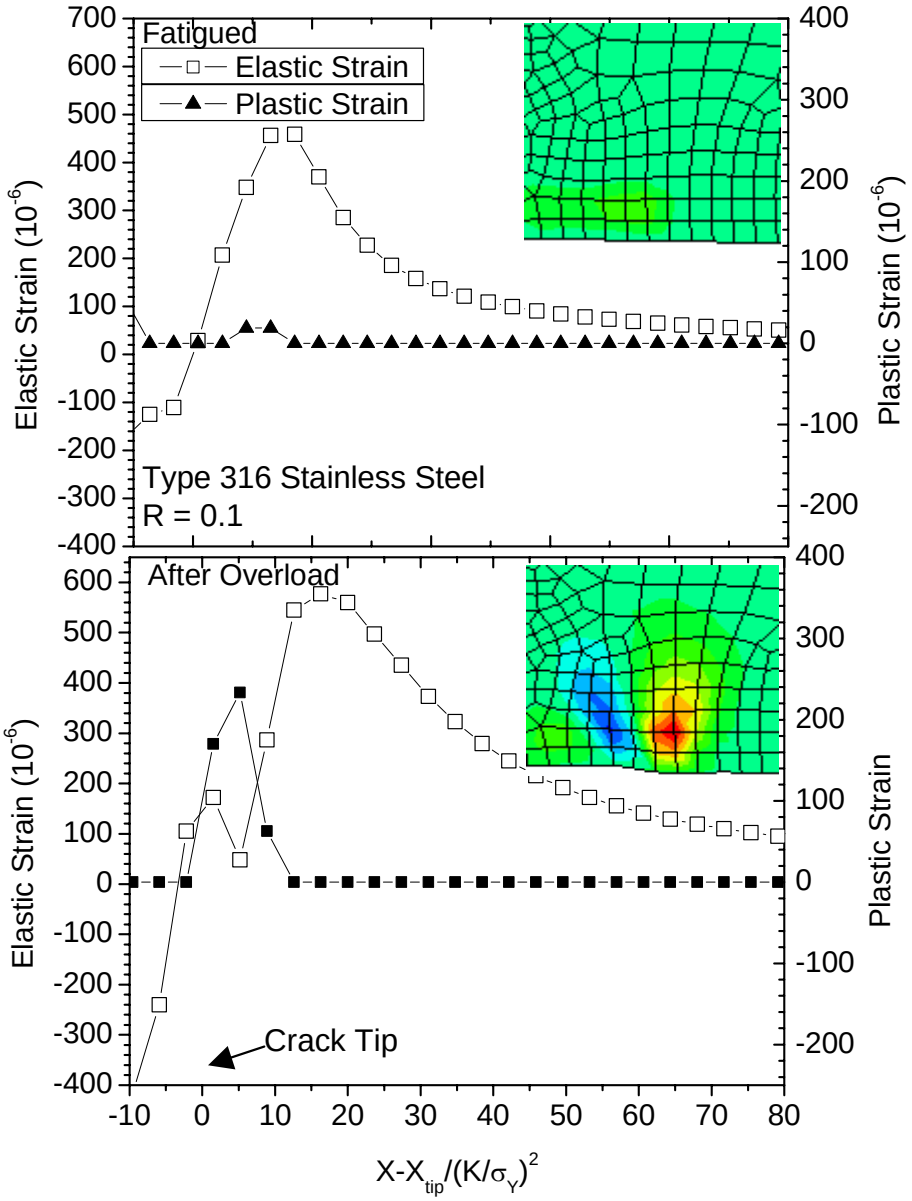


Figure 5.2: Elastic strain and plastic strain distributions at the minimum loads immediately before and after the overload, in (a) and (b), respectively

5.4 Summary

The physical mechanisms of the plasticity-induced crack closure resulting in the retardation of the crack propagation were investigated using the FEM simulation and ND technique. The overloading produces a large plastic zone, which has been observed from plastic strains (FEM) and the dislocation-density (ND) distributions. The overload-induced plastic deformation results in compressive elastic strains (FEM and ND) in front of the crack tip. The compressive elastic strains and large plastic zones are responsible for the retardation of the post-overload crack propagation.

Chapter 6

Changes in Lattice-Strain Profiles around a Fatigue Crack through the Retardation Period after the Overload

6.1 Introduction

Fatigue-crack growth is driven predominantly by the crack-tip plasticity. Sudden changes in the loading patterns during cyclic deformation could result in complicated plastic zones around the crack tip and influence the crack-growth rate and the fatigue life. More specifically, "overloading" beyond the regular stress amplitude during fatigue causes the retardation of crack-growth rates. The retardation persists

until the crack has propagated through the perturbed plastic zone. Therefore, the retardation period depends on both the fatigue-induced and overload-induced plastic zones [119, 120].

Neutron diffraction is a nondestructive method [121] that is useful for the study of the overload effects by mapping the elastic internal strains around the crack tip. Previously, a compressive lattice-strain profile was clearly observed ahead of a fatigue-crack tip after an overload using neutron diffraction [103]. In this paper, the evolution of the residual-strain profiles around a fatigue crack is investigated during the retardation period, and the result is discussed in the context of the perturbed plastic zone. The results provide a microscopic understanding of the overload effect during cyclic loading.

6.2 Experimental Details

Figure 6.1 shows a typical crack-growth rate (da/dN) vs. stress-intensity-factor range (ΔK) curve measured from a Type 316 LN (low-carbon nitrogen-added) austenitic stainless steel. A total of seven compact-tension (CT) specimens were prepared to represent different stages through the da/dN vs. ΔK curve as marked in Figure 6.1. The CT specimens (with a width of 50.8 mm, a thickness of 6.35 mm) were fatigue-deformed using a Material Test System (MTS) electrohydraulic machine with a frequency of 10 Hz and a constant load ratio, R = 0.1, where R = $P_{min.}/P_{max.}$, $P_{min.}$ and $P_{max.}$ are the applied minimum (988 N) and maximum (9,880 N) loads, respectively [103, 120]. The crack lengths of the specimens (SP) are: SP1 = 13 mm, SP2 =

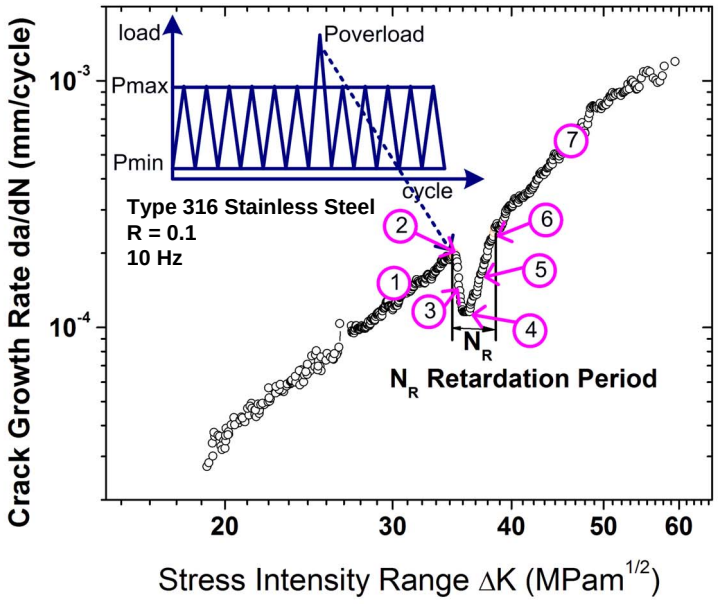


Figure 6.1: The effect of overload on fatigue-crack propagation. During the fatigue tests, seven specimens were prepared.

15.3 mm, SP3 = 15.6 mm, SP4 = 16.3 mm, SP5 = 17 mm, SP6 = 17.9 mm, and SP7 = 25.3 mm. Crack lengths were measured by the crack-opening-displacement (COD) gauge using the unloading-compliance technique [49, 88, 89]. Specimen 1 (SP1) did not experience the overload and was subjected only to the fatigue deformation. The overload (13,189 N) was applied as the crack length reached 15.3 mm. At the overload, the maximum stress-intensity factor, K_{max}, was 51.8 MPa$\sqrt{m}$. The specimen 2 (SP2) was stopped right after the overload. Specimens 3 to 7 were fatigue deformed further after the overload through the retardation period as shown in Figure 6.1. Note that the values of ΔK and K_{max} can be calculated using the applied load and crack length for the CT specimens [49, 88, 89, 103].

Neutron-diffraction strain measurements were performed using the NRSF2 instrument at the High Flux Isotope Reactor of the Oak Ridge National Laboratory. The wavelength from the Si331 doubly-focusing monochromator was 1.73 $\dot{A}$. The stainless-steel (311) reflection was used for determining the strain. The incident neutron beam was defined by 2-mm wide and 1-mm tall (along the crack length) incident beam slits, and the diffracted beam was collimated using a 2-mm wide slit, resulting in a 4 mm^3 gauge volume defined at the middle of the specimen thickness. About thirty diffraction patterns were recorded for each specimen along the crack length from approximately 5 mm behind the crack tip to about 20 mm ahead of the crack tip. The d-spacings along transverse (parallel to fatigue loading), longitudinal (along crack growth direction), and normal (through-thickness) directions were determined by the Pseudo-Voigt fitting of the (311) reflections. Subsequently, the lattice strains

were calculated using:

$$\varepsilon = (d - d_0)/d_0 \tag{6.1}$$

where d_0 is the stress-free lattice parameter, which was measured away from the crack tip at a corner of each CT specimen, using the same gauge volume for all orientations. For brevity, only the strain data of SP1, SP2, SP3, and SP6 along the transverse direction are reported here, and the data for the other specimens and the strain components measured along the longitudinal and normal directions will be discussed in a future publication.

6.3 Results and Discussions

Strain profiles along the transverse direction are shown as a function of the distance from the overload point, Figure 6.2. The error bars are from the diffraction peak fitting. Note that the distance from the overload point is the same as the distance from the crack-tip position of the SP2. The profile of SP1 shows small compressive (negative) strains near its crack-tip position (- 5 - 0 mm) with balancing tensile (positive) residual strains at 0 - 8 mm. SP2 (the overloaded specimen) exhibits large compressive strains (maximum of about - 950×10^{-6} or $\mu\varepsilon$) around 0 - 7 mm in front of its crack tip due to the overload. Tensile strains were observed around 7 - 15 mm. SP3, which was fatigue deformed for 28,414 cycles after the overload, shows a similar profile as SP2. However, SP6 exhibits a significantly different strain profile with a smaller magnitude (about - 600 $\mu\varepsilon$) and a wider double-peak shape.

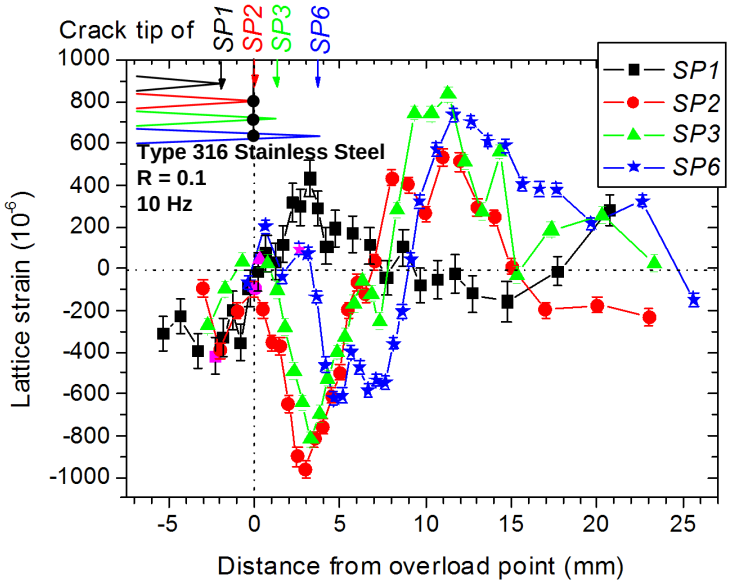


Figure 6.2: The lattice-strain profiles of SP1, SP2, SP3, and SP6 along the transverse direction.

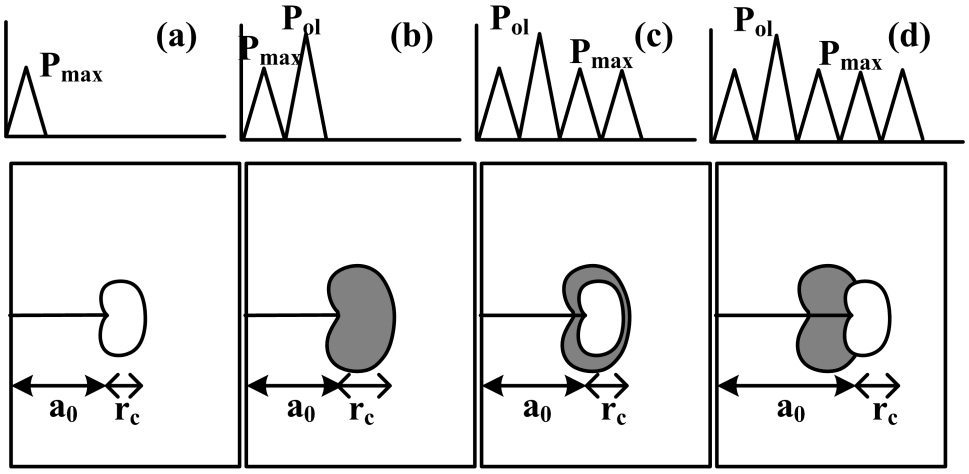


Figure 6.3: The schematic illustration of the perturbed plastic zone. a_0 is the crack length, and r_c is the plastic-zone size.

The evolution of strain profiles described above could explain the retardation phenomenon with a schematic of the perturbed plastic zone represented in Figure 6.3. SP1, without the overload, showed small compressive strains generated by the fatigue deformation, Figure 6.3(a). The large compressive strains observed after the overload, shown in Figure 6.2, are associated with the overload-induced plastic zone, as illustrated in Figure 6.3(b). The strain profile of SP3 is quite similar to that of SP2 because the increase in the crack length during the subsequent fatigue is too small (0.31 mm) to go through the plastic zone already created by the overload, Figure 6.3(c). SP6, with a sufficiently longer crack length (about 2.3 mm longer than that of SP3), there are two peaks in the compressive strain profile. The first peak (about 5 mm away from the overload point) is due to the large plastic zone created by the overload, which seems to have relaxed by about 300 $\mu\varepsilon$, and the second peak (about 7 mm away from the overload point) is caused by the subsequent fatigue

cycles, Figure 6.3(d). This trend indicates that the fatigue-induced plastic zone had grown out of the large plastic zone caused by the overload.

6.4 Summary

In summary, as it was illustrated in Figure 6.1, the overload produced the large plastic deformation (SP2), which, in turn, led to a dramatic decrease in the crack-growth rates (SP3). As the crack grew longer and out of the overload-perturbed region during the subsequent fatigue deformation (SP6), the crack-growth rates recovered to the original slope. These results greatly enhance our understanding of the overload effect during cyclic loading.

Chapter 7

The Study of Lattice Strain/Stress Mapping around a Fatigue Crack during the Retardation Period after an Overload Using Neutron Diffraction

7.1 Introduction

The research on the fatigue of materials can be traced back to the first half of the nineteenth century. Since then, many scientists and engineers have made pioneering contributions to the understanding of fatigue in a wide variety of metallic and

nonmetallic, brittle and ductile materials. In 1913, [20] proposed the concept of stress concentrations at geometrical discontinuities, and, thus, provided an explanation for why fractures emanate from cracks, holes, or defects. In 1960, Paris and co-workers [26] first proposed the relationship between the fatigue-crack-growth rate and the cyclic-stress-intensity parameter. Their approach has been widely adapted for characterizing the growth of fatigue cracks. The studies of crack initiation and propagation are mostly based on microscopic observations and bulk measurements of crack growth (such as those based on compliance changes that are estimated from strain gauges, clip gauges and push-rod gauges, the ultrasonic or acoustic-emission methods [38], or changes in electrical potentials [122–125]. There is no direct quantitative data describing the actual complete crack-tip stress/strain field accompanying fatigue-crack growth. Despite nearly one hundred years of study, a comprehensive understanding of the fundamental mechanism of fatigue-crack propagation has yet to be established.

The fatigue-crack closure, even at far-field tensile loads, was first discovered experimentally by Elber [40, 41]. During the growth of a fatigue crack, load excursions in the form of single tensile overloads can result in the retardation of the crack advance. The plasticity-induced crack-closure mechanism has received considerable supports in the fatigue community. After the overload, large tensile plastic strains are developed near the crack tip, which are not fully reversed upon unloading. The irreversible plastic strains lead to the formation of the plastic wake behind the crack tip, which can decrease the crack-propagation driving force. On the other hand, the plastic deformation induced near the crack tip during loading results in a compressive

residual stress when the load is released. The effect of this residual compressive stress near the crack is significant, which can retard the post-overload crack growth [102].

A complete mechanistic understanding of the retardation phenomena following the tensile overload is required, in order to develop complete models to predict the crack-propagation behavior under various amplitude loading conditions. It is imperative that the stresses associated with the crack closure are fully understood and quantified for these models to be verified and developed further. Neutron-diffraction techniques offer a means of probing the local elastic-microstrain evolution, and, hence, the microstress evolution. Therefore, such measurements can provide a needed insight and validation regarding local deformation processes. As an example, one could use the variation of the micostrain/microstress as a function of the distance from the crack tip to obtain critical insights on the development of the deformation around the crack tip. The objective of this paper is to study the fatigue-crack-growth behavior and measure associated crack-tip strains/stresses, in particular with respect to the crack closure. This paper is intended to give a report on the recent work based on the experimental results of specimens with the fatigue crack that was subjected to an overload.

7.2 Theory

In 1972, Wheeler [10] presented how to improve the accuracy of crack growth predictions in metal subjected to variable-amplitude-cyclic loading. In his model, he

assumed the retardation of the crack propagation following an overload was responsible for the plastic zone in front of the crack tip. Wheeler's model is one of the simplest and most widely used retardation analyses [74]. This model relates the crack growth rate to the overload plastic zone size and the current plastic zone size (Figure 7.1). The former quantity is given by

$$R_{y(o)} = \frac{1}{\beta\pi}(\frac{K_0}{\sigma_Y})^2 \tag{7.1}$$

where K_o is the stress intensity at the overload, and $\beta = 2$ for plane stress and $\beta = 6$ for plane strain. The plastic zone size that corresponds to the current K_{max} is given by

$$R_{y(c)} = \frac{1}{\beta\pi}(\frac{K_{max}}{\sigma_Y})^2 \tag{7.2}$$

where K_{max} is the stress intensity at the maximum load, and $\beta = 2$ for plane stress and $\beta = 6$ for plane strain.

Wheeler [10, 74] assumed that retardation effects persist as long as $R_{y(c)}$ is contained within $R_{y(o)}$ (Figure 7.1), known as the perturbed plastic zone. The overload effects disappear when the current plastic zone begins to grow out of the overload plastic zone. For a crack that has grown Δa since the overload, Wheeler defined a retardation factor C_p in order to calculate the crack propagation within the perturbed plastic zone. The crack growth rate is reduced from a baseline value by C_p:

$$(\frac{da}{dN})_R = C_p\frac{da}{dN} \tag{7.3}$$

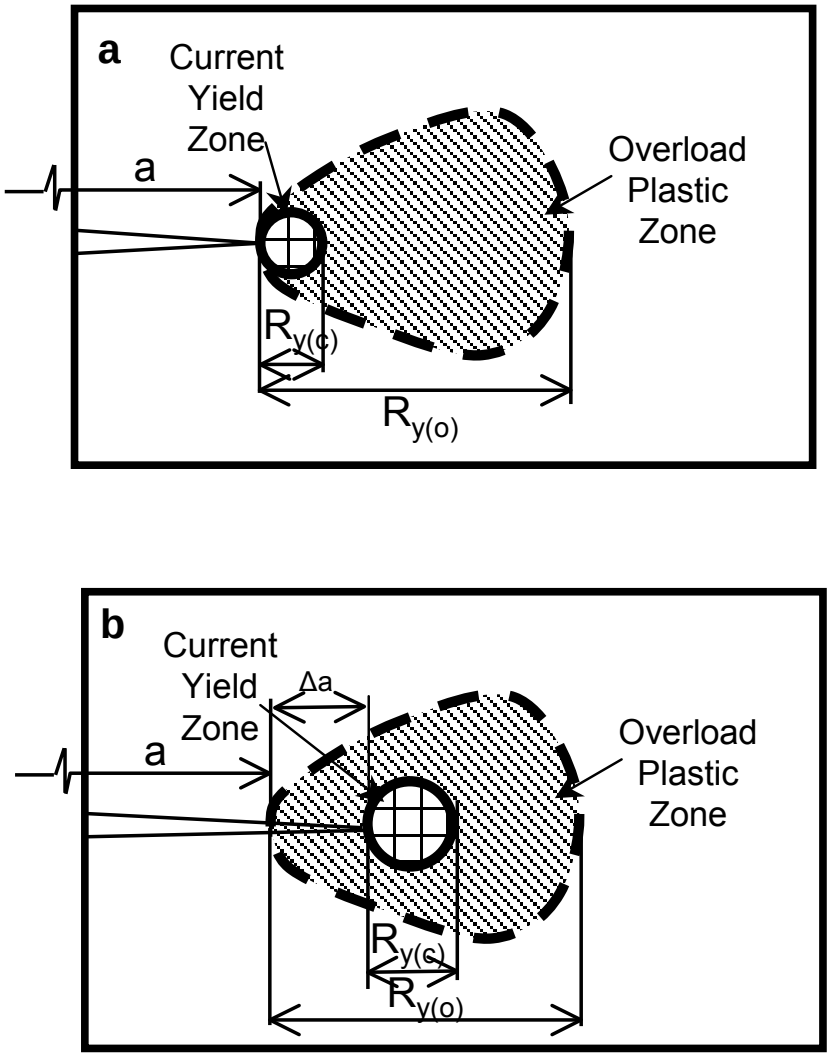


Figure 7.1: The Wheeler model for fatigue retardation [10]

Using Wheeler's assumptions and model, the retardation of crack growth due to variations in applied loading can be computed and with reasonable accuracy. However, the retardation following an overload is a complicated phenomenon. The perturbed plastic zone has not been observed or investigated. In this study, several specimens representing different stages within the retardation period are prepared in order to study the mechanisms of the retardation phenomenon.

7.3 Experimental Procedures

7.3.1 Specimen Preparation

The experiments were performed on six CT specimens of a Type 316 LN stainless steel, which is a low-carbon nitrogen-added (LN) austenitic stainless steel. A schematic of the CT specimen, with a width of 50.8 mm, a thickness of 6.35 mm, and a notch length of 10.16 mm is shown in Figure 7.2. The CT specimens were pre-cracked under a fatigue-loading condition using a Material Test System (MTS) electrohydraulic machine. Fatigue loading was performed in a load-control mode with a frequency of 10 Hz and a constant load ratio, R = 0.1, where R = $P_{min.}$ /$P_{max.}$ $P_{min.}$ and $P_{max.}$ are the applied minimum (988 N) and maximum (9,880 N) loads, respectively. The K value was obtained, using the Equation 1.2 [49, 86, 87]. The crack length was measured by the crack-opening-displacement (COD) gauge using the unloading-compliance technique [47, 88–91]

An overload (13,189 N) was applied when the crack reached 15.3 mm. Figure 7.3. shows a sketch of the fatigue-loading pattern with one tensile overload (a), and (b)

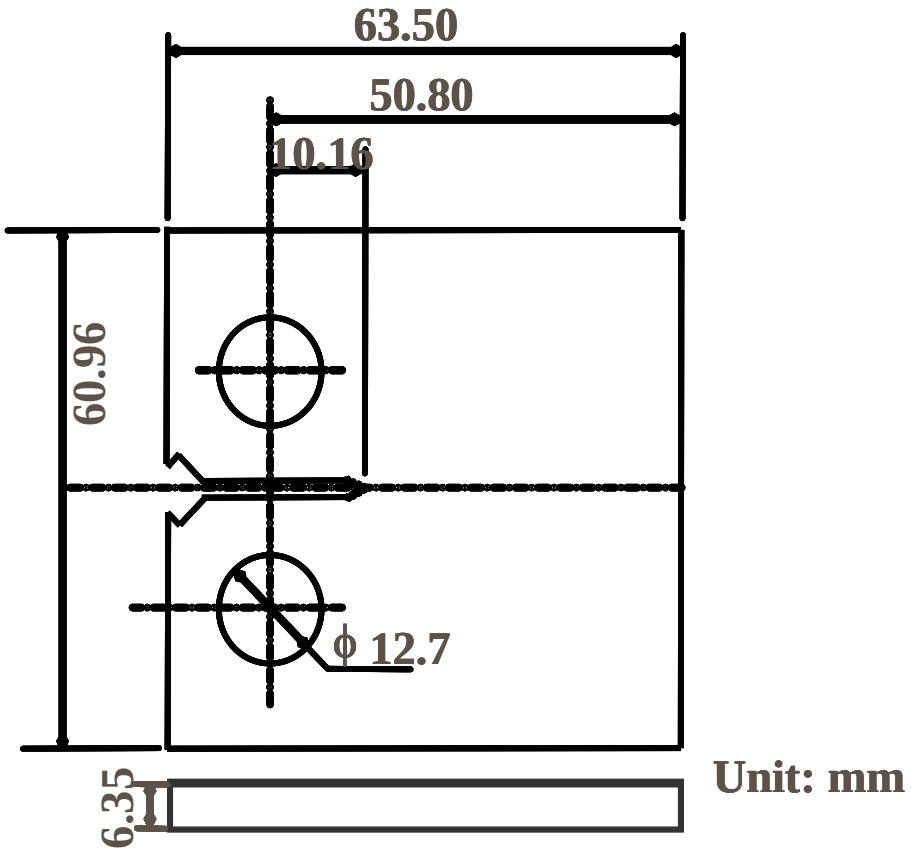


Figure 7.2: Compact-tension specimen of Type 316 LN stainless steel with a thickness of 6.35 mm, a notch length of 10.16 mm, and a crack length of 22.86 mm.

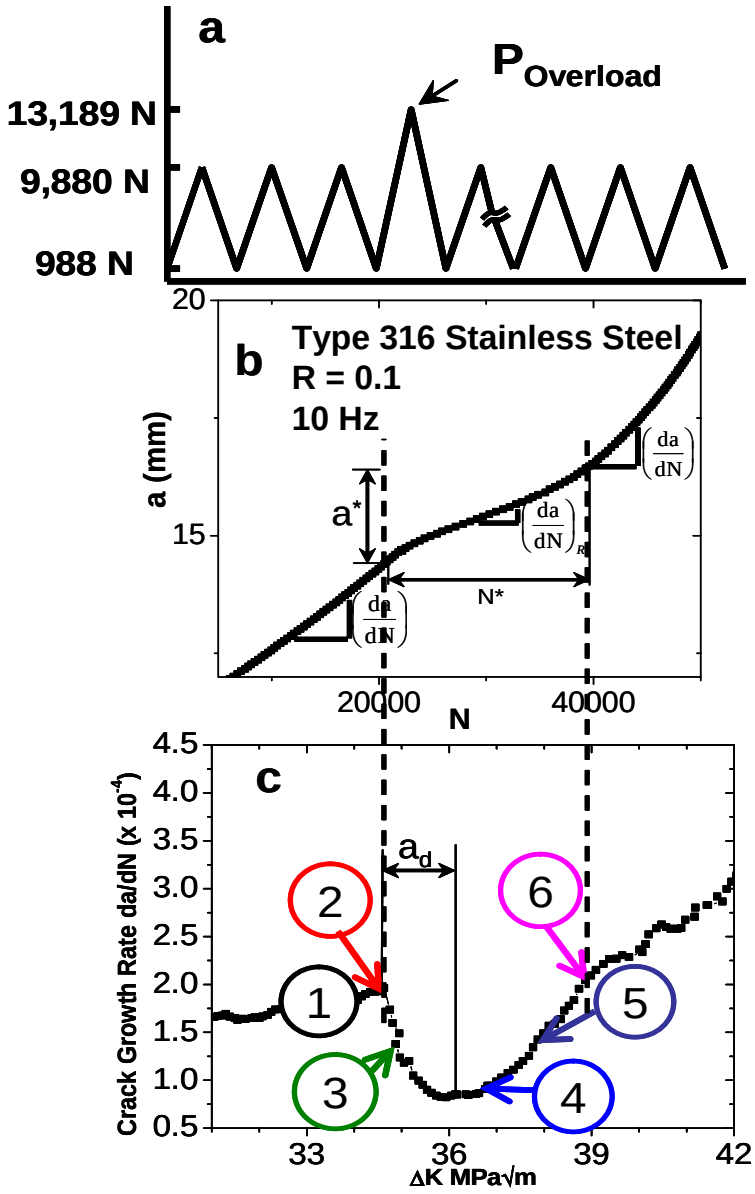


Figure 7.3: (a) Fatigue-loading pattern, (b) crack length vs.number of cycles, and (c) crack-growth rate vs. stress-intensity-factor range, ΔK. Six specimens were prepared at different stages during the retardation period.

and (c) present the fatigue experimental results. A total of six compact-tension (CT) specimens were prepared to represent different stages through the da/dN vs. ΔK curve as marked in Figure 7.3(c). As shown in Figures 7.3(b) and (c), as the stress-intensity-factor range, ΔK, increased, the crack-growth rate (da/dN) increased linearly on the log-log scales. Specimen 1 (SP1) did not experience the overload and was subjected only to the fatigue deformation. The specimen 2 (SP2) was stopped right after the overload, and the crack length extended to 15.3 mm. After the tensile overload was applied, the exponentially increasing crack growth was followed by a period of decelerated crack growth. This progressive reduction in the crack velocity continued over a crack-growth distance of a_d (about 1 mm), which is known as the delay distance. Specimen 3 (SP3) was prepared during the delay distance, and the crack length extended to 15.6 mm. Then the crack-growth rate reached a minimum. The specimen 4 (SP4) was prepared as the crack-growth rate reached the minimum, and the crack length was 16.28 mm. Following the minimum crack velocity, the crack growth rates began to increase. As the crack-growth rate increased, specimen 5 (SP5) and specimen 6 (SP6) were prepared, and the crack length reached 17 mm and 17.92 mm, respectively. Eventually, the crack-growth rates catch up with the pre-overload value (da/dN). The total crack growth, a*, was 2.6 mm, and the number of post-overload cycles, N*, was 41,000 cycles, over which the transient effects of the single tensile overload affect crack growth, and were a strong function of ΔK, the microstructure, and environment, as well as factors like the R ratio, and overload ratio, $r_{ol} = P_{overload} / P_{max}$, $P_{overload}$ is the overload [102]. After the post-overload, the fatigue crack was subjected to the same fatigue parameters as in the pre-overload

Table 7.1: Crack length of the specimens

Specimens	1	2	3	4	5	6
Crack Length (mm)	13	15.3	15.6	16.3	17	17.9

regime, the crack-growth rate recovered to (da/dN). SP1 did not experience the overload. The overload (13,189 N) was applied as the crack length reached 15.3 mm. SP2 was stopped right after the overload. SP3 to 6 were fatigue deformed further after the overload through the retardation period as shown in Figure 7.3 and Table 7.1.

7.3.2 Neutron Experiments

Neutron-diffraction strain measurements were performed, using the neutron residual strain/stress measurement facility (NRSF2) instrument at the High Flux Isotope Reactor of the Oak Ridge National Laboratory. The wavelength from the Si331 doubly-focusing monochromator was 1.73 $\mathring{A}$. The stainless-steel (311) reflection was used for determining the strain. The incident neutron beam was defined by 2-mm wide and 1-mm tall (along the crack length) incident beam slits, and the diffracted beam was collimated using a 2-mm wide slit, resulting in a 4-mm^3 gauge volume defined at the middle of the specimen thickness. For one-dimensional (1-D) strain measurements, about thirty diffraction patterns were recorded for each specimen along the crack length from approximately 5 mm behind the crack tip to about 20 mm ahead of the crack tip. The d-spacings along transverse (parallel to the fatigue loading direction), longitudinal (along the crack-growth direction), and normal directions (the through-thickness direction) were determined by the Pseudo-Voigt fitting of the

(311) reflections and, subsequently, the lattice strains were calculated using:

$$\varepsilon = (d - d_0)/d_0 \tag{7.4}$$

where d_0 is the stress-free lattice parameter, which was measured away from the crack tip at a corner of each CT specimen, using the same gauge volume for all orientations.

For two-dimensional (2-D) strains mapping, only SP 1, 2, and 6 were measured, and the mapping positions are shown in Figure 7.4. . The (0, 0) position is the crack tip. The mappings were conducted from -5 mm to 25 mm along the x direction, and from -5 mm to 20 mm along the y direction, resulting in a 30 mm x 25 mm mapping area. Only the d-spacings along the transverse direction (parallel to the fatigue-loading direction) were determined. The stress-free lattice parameter is an averaged value over several different positions on an undeformed CT specimen.

7.4 Results

7.4.1 Strain/Stress Profiles

Strain profiles along the transverse direction are shown as a function of the distance from the overload point, Figure 7.5. Note that the distance from the overload point is the same as the distance from the crack-tip position of the SP2. The profile of SP1 shows small compressive (negative) strains near its crack-tip position (-5 - 0 mm) with balancing tensile (positive) residual strains at 0 - 8 mm. SP2 (the overloaded

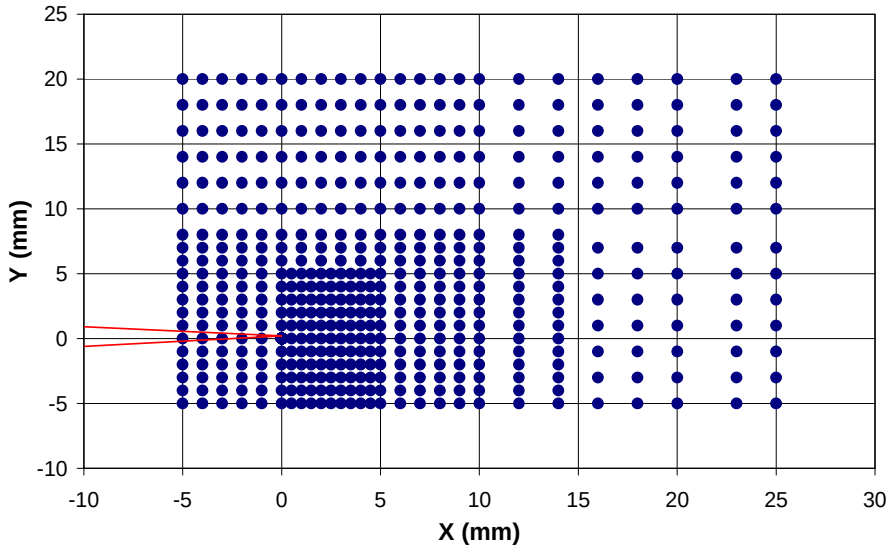


Figure 7.4: Measurement positions for the two-dimensional (2-D) strain mapping

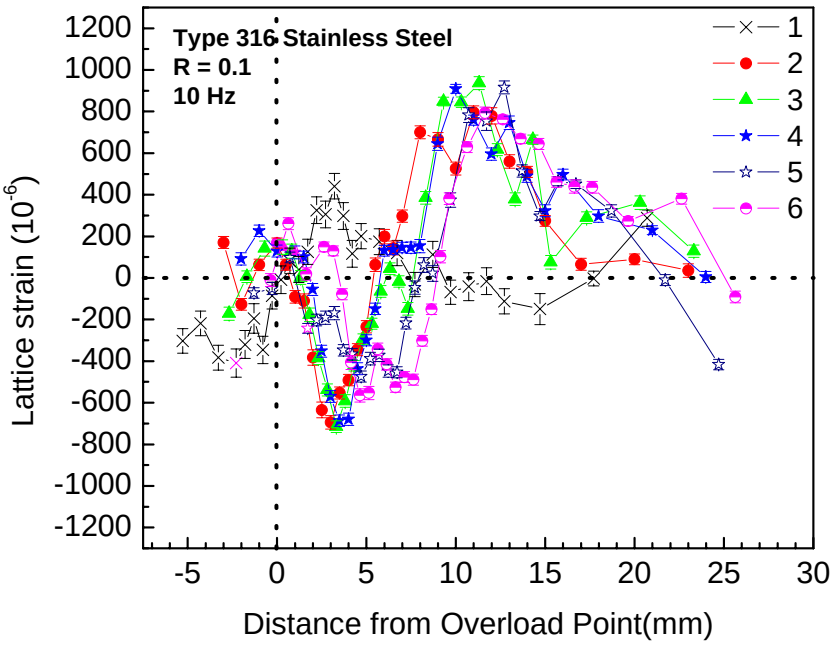


Figure 7.5: Lattice-strain profile for SP1, SP2, SP3, SP4, SP5 and SP6 along the transverse direction.

specimen) exhibits large compressive strains (maximum of about - 800 x 10^{-6} or $\mu\varepsilon$) around 0 - 5 mm in front of its crack tip due to the overload. Tensile strains were observed around 6 - 17 mm. SP3, SP4 which are fatigue deformed after the overload, shows a similar profile as SP2. However, SP5 and SP6 exhibits a significantly different strain profile with a smaller magnitude (about - 600 $\mu\varepsilon$) and a wider double valley shape. The first compressive minimum is at 5 mm, and the second is at about 7 mm.

Strain profiles along the transverse, longitudinal, and normal directions are shown as a function of the distance from the crack tip for specimen 2, are shown in Figure 7.6 The strains along normal direction reach maximum at about 3 mm from the crack tip, and minimum at about 9 mm from the crack tip, which are opposite to that along the transverse direction. The strains along longitudinal are close to zero.

Stresses were calculated from three orientation lattice-strain measurements using Equation 7.5

$$\begin{aligned} \sigma_x &= \tfrac{E}{1+\nu}\varepsilon_x + \tfrac{\nu E}{(1+\nu)(1-2\nu)}(\varepsilon_x + \varepsilon_y + \varepsilon_z) \\ \sigma_y &= \tfrac{E}{1+\nu}\varepsilon_y + \tfrac{\nu E}{(1+\nu)(1-2\nu)}(\varepsilon_x + \varepsilon_y + \varepsilon_z) \\ \sigma_z &= \tfrac{E}{1+\nu}\varepsilon_z + \tfrac{\nu E}{(1+\nu)(1-2\nu)}(\varepsilon_x + \varepsilon_y + \varepsilon_z) \end{aligned} \tag{7.5}$$

Here we only report stress distributions for SP1, SP2, SP4, and SP6, which are shown in Figures 7.7 and 7.8. The stress profile of SP1, which was subjected only to fatigue deformation, shows compressive stresses behind the crack tip from -5 to 0 mm. The stress profile of SP2, which experienced the overload, exhibits compressive stresses up to -150 MPa from 0 mm to 7 mm from the crack tip, and tensil stresses from 7 mm to 17 mm. For SP4, fatigue deformed following the overload, the stress profile exhibits a minimum compressive stresss of -180 MPa at about 3 mm from

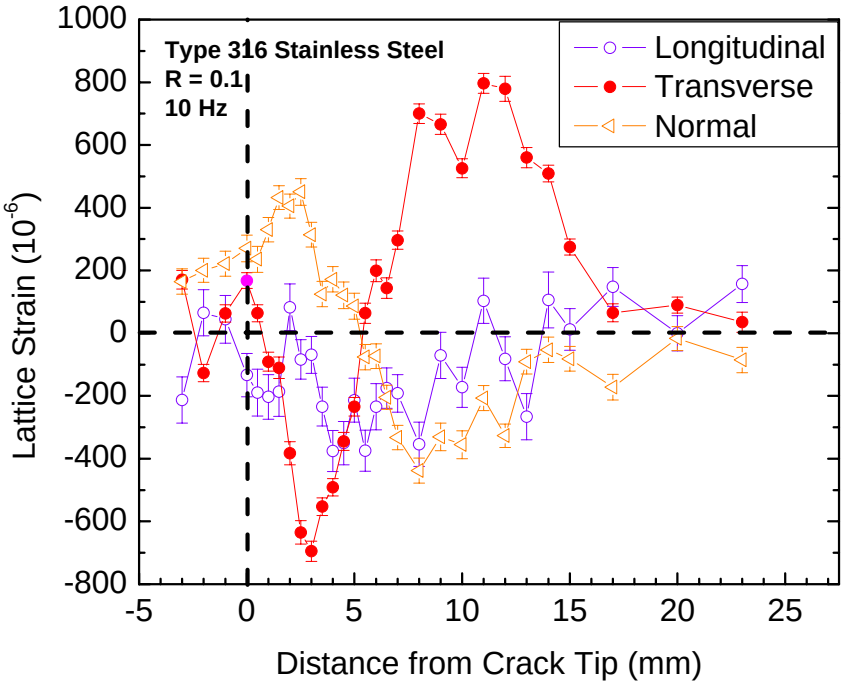


Figure 7.6: Lattice-strain profile for SP2 along transverse, longitudinal, and normal directions.

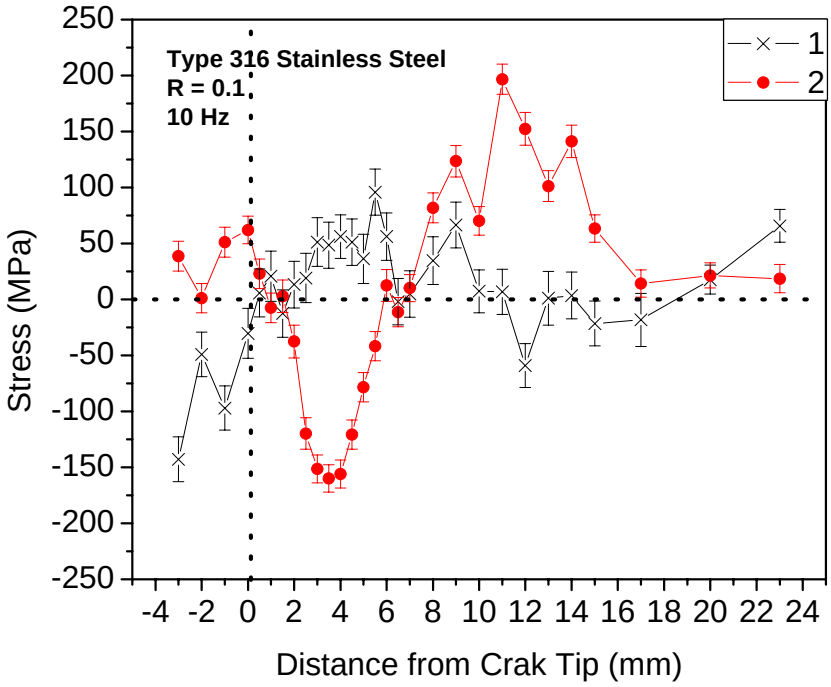


Figure 7.7: Stress distributions as a function of the distance from the crack tip for SP1 and SP2

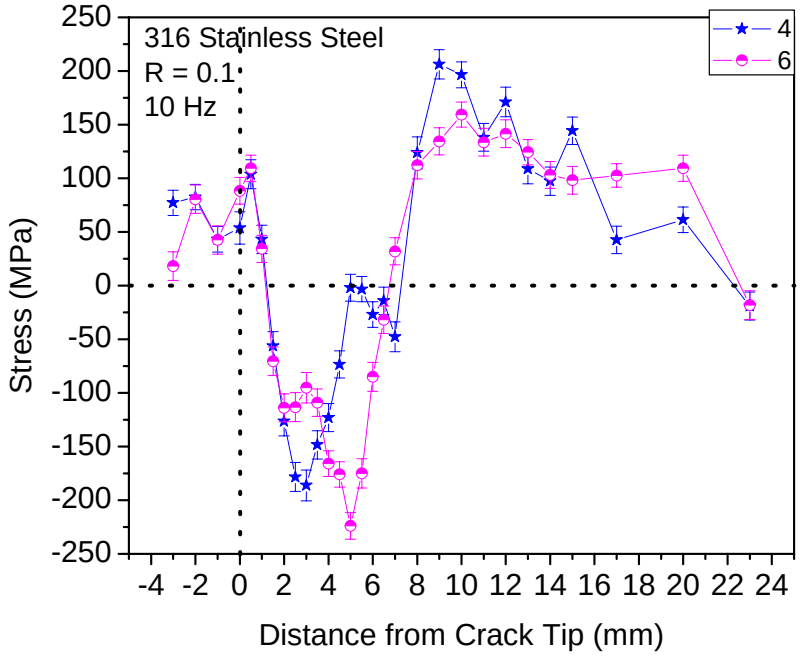


Figure 7.8: Stress distributions as a function of the distance from the crack tip for SP4 and SP6

the crack tip, and a second minimum compressive stress of -50 MPa at about 7 mm from the crack tip. The tensile stresses were observed from 8 mm to 24 mm, which balance the compressive stresses. The stress profile of SP6 is similar to that of SP4. The first minimum compressive stress of -120 MPa was observed at about 2 mm to 3 mm from the crack tip, and a second mimimum compressive stress of -230 MPa appeared at approximately 5 mm from the crack tip. The tensile stresses exhibit from 8 to 24 mm.

7.4.2 Two-Dimensional (2-D) Strain-Mapping Contours

The 2-D strain-mapping positions for SP 1, 2, and 6 are shown in Figure 7.9 . In Figures 7.9(a), (b), and (c) show the strain-mapping contours for SP1, SP2, and SP6, respectively. Presented in the mapping contour of SP1, the compressive strain region (along the x direction from 0 to 3 mm) is observed around the crack tip. The minimum compressive strain is about - 200 $\mu\varepsilon$. The tensile strain region is from 5 to 16 mm along the x direction, and the maximum tensile strain of 400 $\mu\varepsilon$ exhibit at about (8 mm, 0 mm). Along the y direction, the maximum values at y = 0 were found. The SP2 was overloaded. The maximum compressive strain reachs -500 $\mu\varepsilon$ at (2 mm, 0 mm). The maximum tensile strain of 700 $\mu\varepsilon$ exhibits at (8 mm, 0 mm). The areas of compressive and tensile strains are larger than those of the SP1. The SP6 is continually fatigue tested after the overload. The minimum compressive strain of -350 $\mu\varepsilon$ and tensile strains of 700 $\mu\varepsilon$ are also observed at about (2 mm, 0 mm) and (8 mm, 0 mm). The tensile strains area of SP6 is smaller than that of SP2.

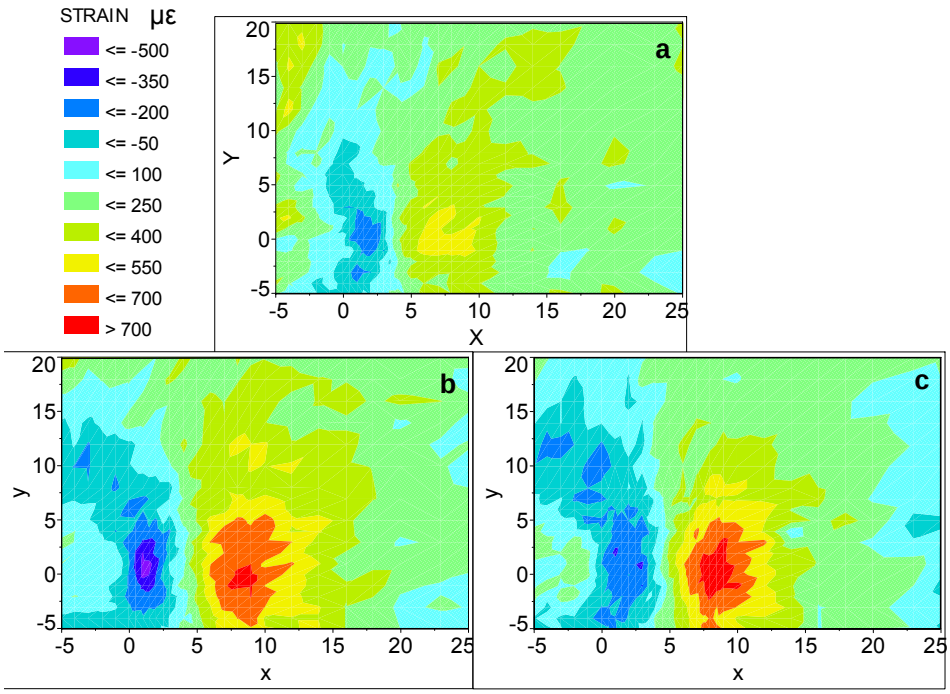


Figure 7.9: (a), (b), and (c) strain contours for SP1, SP2, and SP6, respectively

The strain contours for all the three specimens exhibit the symmetric deformation along y = 0.

7.5 Discussions

7.5.1 Crack Closure

During fatigue cycling, the monotonic plastic zone generated on loading is compressed by the surrounding elastic material as the load is reduced from K_{max}. This trend leads to a residual compressive stress at the crack tip that will reach the yield stress, producing a reverse plastic zone. Under constant-amplitude fatigue, this region of the reverse plasticity is repeatedly yielded in tension and compression, which is referred to as the cyclic plastic zone. The reverse yielding ahead of a fatigue crack loaded in the cyclic tension produces a residual compressive stress in the cyclic plastic zone. When an overload is applied, the overload produces a large plastic deformation, which causes the size of the zone of the residual compression to increase. It has been suggested that these residual compressive stress can retard the post-overload crack growth [74, 118]. The compressive stress decays gradually outside the cyclic plastic zone, and to maintain equilibrium, a residual-tensile-stress field is established in the remainder of the uncracked ligament [1].

The residual stress/strain mappings around the crack tip were observed from the neutron residual stress/strain measurements. The 1-D stress and 2-D strain mappings show a good agreement on the stress/strain distribution. For SP1 (without the overload), a small amount of compressive stress/strain was found near the crack

tip, which is due to the reverse-plastic deformation produced by fatigue experiments. For SP2 (right after the overload), there are clearly large compressive stresses/strains around the crack tip, ranging from 0 mm to 5 mm, which is caused by the overload-induced instantaneous large plasticity. The overload increased the size of the cyclic plastic zone, and also the residual compressive stresses/strains. These compressive stresses/strains retard the crack-propagation rate. The tensile stress/strain fields range from 5 to 20 mm, which can balance the compressive stress/strain field. These 1-D stress and 2-D strain mapping results show that both the shape and magnitude of the local residual stress/strain field and caused by the overload event.

7.5.2 Perturbed-Plastic Zone

During fatigue experiments, the yielding of the material near the crack tip produced plastic zone. After an overload was imposed, the overload induced an instantaneous large plastic zone. Right after the overload, the following subsequent fatigue plastic zone grew inside the large overload-induced plastic zone. And then, as the crack grew longer, the subsequent fatigue plastic zone began grew outside of the overload induced one. Finally, the fatigue plastic zone did not perturb with the overload-induced plastic zone anymore.

The stress/strain distribution measured by neutron diffraction technique shown in Figures 7.5, 7.7, 7.8, and 7.9, can be explained by the perturbed plastic zone with the schematic of the perturbed plastic zone represented in Figure 7.1. As described before in the results section: The SP1 (Figures 7.5, 7.7, and 7.9), there are small amount of the compressive stresses/strains near the crack tip; The SP2 (Figures 7.5,

7.7, and 7.9), large compressive stresses/strains are observed in front of the crack tip; The SP6 (Figures 7.5, 7.8 and 7.9), the stress/strain profile also has two minimum compressive stress regions.

Fatigue experiments induced a relatively small amount of the plastic deformation. The small compressive stress/strain near the crack tip of SP1 is due to the reversed fatigue-plastic zone. Right after the application of the overload, the large plasticity results in the large compressive stress/strain in front of the crack tip of SP2. The crack of SP4 increased about 1 mm during the subsequent fatigue. The fatigue-induced plastic zone went through the plastic zone already created by the overload. The first minimum compressive stress in the compressive stress region of SP4 is due to the large plastic zone created by the overload, and the second minimum compressive stress is caused by the subsequent fatigue cycles. The SP6 has a sufficiently longer crack length (about 1.6 mm longer that SP4). The first minimum compressive stress/strain (about 3 mm away from the crack tip) is due to the large plastic zone created by the overload, which seems to have relaxed by about 100 MPa, and the second minimum compressive stress/strain (about 5 mm away from the crack tip) is caused by the subsequent fatigue cycles, which increased 200 MPa compared with that of SP4. This trend indicates that the fatigue-induced plastic zone had grown out of the large plastic zone caused by the overload, and the fatigue-induced deformation dominates the stress distribution. Hence, the crack-growth rate begun to recover back to the pre-overload crack-propagation rate. In summary, as it was illustrated in Figure 7.3, the overload produced the large plastic deformation (SP2), which, in turn, led to a dramatic decrease in the crack-growth rates (SP3 and

Table 7.2: Stress-intensity calculations and fatigue-plastic zone sizes for SP2, SP3, SP4, SP5, and SP6.

	2	3	4	5	6
K MPa$\sqrt{m}$	51.8	39.52	40.9	42.42	44.44
$R_{Y(C)}$ (mm)	1.7 - 5.15	1 - 3	1.07 - 3.21	1.15 - 3.46	1.26 - 3.79

SP4). As the crack grew longer and out of the overload-perturbed region during the subsequent fatigue deformation (SP5 and SP6), the crack-growth rates recovered to the original slope. These results greatly enhance our understanding of the overload effect during cyclic loading.

Using Equations 7.1 and 7.2, the overload induced plastic zone and current fatigue plastic zone can be estimated. At the overload, the maximum stress-intensity factor, K_O, is 51.8 MPa$\sqrt{m}$. $R_{y(O)}$ ranges from 1.7 - 5.2 mm. The compressive strain/stress region of SP2 ranges from 0 - 5 mm. Also the current plastic zones $R_{y(c)}$ for SP3, SP4, SP5, and SP6 are listed in Table 7.2. The sizes of the compressive strain/stress region measured by the neutron-diffraction technique are close to the estimated plastic zone size.

7.6 Conclusions

1. The compressive strains/stresses in front of the crack tip, caused by the instantaneous large plastic zone induced by the overload, retarded the crack-growth rate.

2. When the subsequent fatigue-induced plastic zone grows out of the large plastic zone induced by the overload, the crack-growth rate begins to increase, and eventually reaches the pre-overload crack-growth rate.

Chapter 8

Conclusions

During fatigue-crack-growth tests, after the overload, the crack-growth-retardation period was observed. During the retardation period, the crack-growth rate significantly deceased, which is because of the plastic deformation induced by the overload. The retardation period is also confirmed by the measurement of the striation-spacing changes before and after the overload. Crack closure at the retardation period due to the plastic deformation was investigated by neutron diffraction.

Elastic-lattice strains and the associated plastic zone around the crack tip in Type 316 LN steel were investigated using an in-situ neutron-diffraction technique. The elastic strains in the in-plane direction (parallel to the loading direction) were measured as a function of the distance from the crack tip at different applied loads ranging from 667 N to 8,889 N. The results showed the evolution of lattice-strain profiles associated with the in-situ applied loading as well as the residual-strain profile generated by an overload. Lattice-stain profiles from the through-thickness (TT) and

in-plan (IP) directions have the opposite signs, which agree with the Possion's effect. As the in-situ load increased from 667 N to 6,667 N, the maximum lattice strain in the IP direction increased. As the load decreased from 8,889 N to 667 N, the lattice strain decreased. After the overload, a significant compressive strain of - 600 $\mu\varepsilon$ (or $\times 10^{-6}$) was observed in front of the crack tip, which is related to the crack-closure phenomenon and retardation of crack growth. Also from the lattice-strain profiles, the large compressive strain at LP7 was observed after the overload, which indicates the crack closure, because the compressive stress retards the crack growth.

The plastic deformation is irreversible. The peak-width change after the overload is due to the plastic deformation. The plastic-zone size in front of the crack tip was estimated using the peak-broadening analysis, which agrees well with the theoretically-predicted plastic-zone size of 7.9 mm.

The dislocation density around the crack tip is calculated. The averaged dislocation density is about 10^{10} cm^{-1}. The dislocation density is high in front of the crack tip from the IP direction calculation. The dislocation density changes slightly as a function of the distance from the crack tip in the TT direction. The different neutron-diffraction results from IP and TT directions indicates the inhomogeneity of the plastic deformation at the scale of $\sim$ 1 mm.

The inhomogeneous plastic deformations at meso-scales ($\sim$ 1 μm) were observed with the synchrotron PXM, which provides the very local structural information within a 0.5 μm mapping around the crack tip. The length of the "streak" of the Laue pattern depends mainly of the number of geometrically-necessary dislocations

(GNDs) within the irradiated volume, causing local lattice rotations. The Laue patterns obtained at different locations near the crack tip. The analysis of these Laue patterns demonstrates that the plastic-deformation results in the formation of the alternating regions with high and low GNDs densities. Some of the patterns consist of relatively sharp spots corresponding to grains with a relatively low GNDs density. At the same time, some of the patterns demonstrate an intensive "streaking" of all Laue spots. Such streaking is indicative of the strong lattice curvature in these grains. Neighbor grains were deformed differently, depending on their crystallographic orientation, size, and surroundings.

After the retardation period was observed from fatigue experiments. 7 specimens (SP1, SP2, SP3, SP4, SP5, SP6, and SP7) (in Figure 6.1) through the retardation period were prepared. Neutron-diffraction experiments were designed to investigate what cause the increase of the crack-growth rate, and what cause the decease of the crack-growth rate. Strain profiles along the transverse direction are reported as a function of the distance from the overload point. Note that the distance from the overload point is the same as the distance from the crack-tip position of the SP2. The profile of SP1 shows small compressive (negative) strains near the crack tip. SP2 (the overloaded specimen) exhibits large compressive strains (the maximum of about - 950×10^{-6} or $\mu\varepsilon$) around $0 \sim 7$ mm in front of the crack tip due to the overload. SP3 shows a similar profile as SP2. However, SP6 exhibits a significantly different strain profile with a smaller magnitude (about - 600 $\mu\varepsilon$) and a wider double-peak shape.

The evolution of strain profiles described above could explain the retardation phenomenon with a schematic of the perturbed plastic zone represented. SP1, without the overload, showed small compressive strains generated by the fatigue deformation. The large compressive strains observed after the overload are associated with the overload-induced plastic zone. The strain profile of SP3 is quite similar to that of SP2 because the increase in the crack length during the subsequent fatigue is too small to go through the plastic zone already created by the overload. SP6, with a sufficiently longer crack length, there are two peaks in the compressive strain profile. The first peak is due to the large plastic zone created by the overload, which seems to have relaxed, and the second peak is caused by the subsequent fatigue cycles. This trend indicates that the fatigue-induced plastic zone had grown out of the large plastic zone caused by the overload. In summary, the overload produced the large plastic deformation (SP2), which, in turn, led to a dramatic decrease in the crack-growth rates (SP3). As the crack grew longer and out of the overload-perturbed region during the subsequent fatigue deformation (SP6), the crack-growth rates recovered to the original slope. These results greatly enhance our understanding of the overload effect during cyclic loading.

The finite-element-model simulations aim to capture the deformation evolution around a crack tip, as well as the crack-propagation behavior.

In terms of the crack-propagation behavior, our modeling result qualitatively matches with the fatigue-experimental result. Total 800 fatigue cycles were conducted. The overload of 1.33 times of P_{max} was applied at the 400th cycle. A small

amount of temporarily accelerated growth occurs during the cycle of the application of the overload. A period of the decelerated crack growth followed the burst of the accelerated crack advance. After the 500th cycle, the crack-growth rates began to increase. Up to 620th cycle, the crack-growth rate almost catch up with the pre-overload value.

Neutron-diffraction results are direct measurements, which can, then, be used to validate finite-element-modeling predictions. In terms of the contours of the predicted strain, the strain distributions in front of the crack tip from the FEM, have a very good agreement with the results from neutron-diffraction measurements, Figure 7.9. In particular, two features are very well reproduced: compressive stress/strain field evolutions around the crack tip through the retardation period; and the shapes of the tensile strain/stress distribution. The ability of the FEM to predict the precise deformation in the measured strain maps shows that it is a good physical descriptor of the crack-closure mechanism. The present result is promising for the next step, which is to develop a model that is capable of predicting crack-propagation rates under variable-amplitude loading.

Chapter 9

Future Work

First, the strain distribution around a fatigue-crack-tip after the overload have been measured during tensile loading and unloading cycles using neutron diffraction on the Spectrometer for Materials Research at Temperature and Stress (SMARTS) at the Los Alamos Neutron Science Center (LANSCE). The goal of this experiment is to investigate the beginning and the end of the crack-closure within each cycle. The data need to be fully analyzed.

Second, x-ray microbeam diffraction experimental data need to be fully analyzed. The polychromatic x-ray microdiffraction (PXM) can provide a submicron spatial resolution, which is an excellent technique for mapping the deformation around the crack tip at the mesoscale. Using the Laue method we can quantitatively determine the elastic strain and the local orientation distribution in individual grains or subgrains. The Laue spot is sensitive to the deformation, which can provide the precise

information on the phase, grain orientation, and morphology of polycrystalline materials. The results from neutron-diffraction measurements (in millimeter) will be compared with those from x-ray microbeam diffraction measurements. The deformations comparison on multiple scales will provide a better understanding of the damage process that takes place at the crack tip.

Third, an irreversible, hysteretic cohesive model has been implemented into the commercial FEM software, ABAQUS, through a user-define element (UEL) subroutine. In this model, the crack is modeled by a set of cohesive interface elements, which separate according to the constitutive equations relating the traction acting on the two bonded solids to the separation between them. The nucleation and propagation of the crack are the natural result of the finite-element simulation; no ad hoc fracture criterion is required. We can see that the trend of the experimental result from neutron diffraction measurement is qualitatively agreed with the modeling results: the compressive stress fields' evolution around the crack tip through the retardation period; and the shapes of the tensile strain/stress distribution. The model needs to be further advanced in order to obtain quantitatively matched results, including the crack-propagation behavior, stress/strain distribution around the crack tip.

Fourth, stress/strain distributions have been investigated using finite-element model. Our goal is to provide a master curve, which can be used to present the stress distribution at any fatigue process. We need to normalized the stress distribution curves. One master stress/strain curves, which can present the whole fatigue process, needs to be developed.

Fifth, publish papers on all sets of data.

Bibliography

Bibliography

[1] A. Saxena. *Nonlinear Fracture Mechanics for Engineers*. CRC PRESS New York, 1998.

[2] S. Suresh. *Fatiuge of Materials*. Cambridge university press, 1998.

[3] H. Glaucio and Z. Zhang. *5 GRACM International Gongress on Computational Mechanics Limassol*, 2005.

[4] A. Needleman. *J. Appl. Mech.*, 54:525–531, 1987.

[5] K. H. Schwalbe and A. Cornec. Modeling crack growth using local process zones. chapter Technical report, GKSS research centre, Geesthacht.

[6] A. Needlman. *International Journal of Fracture*, 42:21–40, 1990.

[7] V. Tvergaard and J. W. Hutchinson. *J. Mech. Phys. Solids*, 40:1377–1397, 1992.

[8] I. Scheider. Cohesive model for crack propagation analyses of structures with elastic-plastic materials behavior. page April 2001.

[9] J. C. Newman Jr. *ASTM STP*, 761:255, 1982.

[10] E. Wheeler. *Journal of Basic Engineering*, 94:181, 1972.

[11] H. Tian. *Effects of Environment and Frequency on the Fatigue Behavior of the Spallation Neutron Source (SNS) Target Container Material C 316 LN Stainless Steel*. PhD thesis, University of Tennessee, 2003.

[12] H Tian, P. K. Liaw, H Wang, D Fielden, J. P. Strizak, L. K. Mansur, and J. R. Distefano. *Materials Science and Engineering A-Structural Materials Properties Microstructure and Processing*, 314:140–149, 2001.

[13] H. Tian, P. K. Liaw, J. P. Strizak, and L. K. Mansur. *Journal of Nuclear Materials*, 318:157–166, 2003.

[14] H. Tian, P. K. Liaw, D. E. Fielden, J. P. Strizak, and L. K. Mansur. *Metallurgical and Materials Transactions A-Physical Metallurgy and Materials Science*, 35A(10):3334–3339, oct 2004.

[15] H. Tian, P. K. Liaw, D. E. Fielden, L. Jiang, B. Yang, C. R. Brooks, M. D. Brotherton, H. Wang, J. P. Strizak, and L. K. Mansur. *Metallurgical and Materials Transactions A-Physical Metallurgy and Materials Science*, 37A(1):163–173, JAN 2006.

[16] H. Tian, D. Fielden, M. J. Kirkham, and P. K. Liaw. *Journal of Testing and Evaluation*, 34(2):92–97, 2006.

[17] J. P. Strizak, H. Tian, P. K. Liaw, and L. K. Mansur. *Jounal of Nuclear Materials*, 343(1-3):134–144, Aug 2005.

[18] S. Degallaix, G. Degallaix, and J. Foct. In *ASTM STP 942*, pages 798–811. ASTM, Philadelphia, PA, 1988.

[19] J. B. Vogt, J. Foct, C. Regnard, G. Robert, and J. Dhers. *Metallurgical Transactions A*, 22A:2385–2392, October 1991.

[20] C. E. Inglis. *Transactions of the institute of Naval Architects*, 55:219–241, 1913.

[21] A. A. Griffith. *Philosophical Transactions*, A221:163–198, 1920.

[22] H. M. Westergaard. *Journal of Applied Mechnics*, 6:49–53, 1939.

[23] G. R. Irwin. In *Americn Society for Metals*, pages 147–166, Cleveland, 1948.

[24] E. Orowan. *Reports on Progress in Physics*, X11:185–232, 1948.

[25] G. R. Irwin. *Journal of Applied Mechanics*, 24:361–364, 1957.

[26] P. C. Paris, M. P. Gomez, and W. P. Anderson. *The Trend in Engineering*, 13:9–14, 1961.

[27] J. R. Rice. *Journal of Applied Mechanics*, 35:379–386, 1968.

[28] J. A. Begley and J. D. Landes. *American Society for Testing and Materials, STP*, 1(84), 1961.

[29] J. A. Begley and J. D. Landes. *American Society for Testing and Materials, STP*, pages 1–23, 1972.

[30] A. Saxena. In *In fracture Mechanics: ASTM STP 905*, volume Seveneenth, pages 185–201. American Society for Testing the Materials, 1986.

[31] J. Schijve. chapter Advances in Aeronautical Sciences 3. Oxford: Pergamon Press, 1961.

[32] P. C. Paris and F. Erdogan. *Journal of Basic Engineering*, 85:528–534, 1960.

[33] C. Laird. *Fatigue Crack Propagation, ASTM STP 415*, pages 131–180, 1967.

[34] L. Bairstow. *Trans. R. Soc. London*, A210:35–55, 1910.

[35] F. Ellyin. *Fatigue damage, crack growth and life prediction*. Chapman & Hall, 1997.

[36] L. J. Chen, P. K. Liaw, H. Wang, Y. H. He, R. L. McDaniels, L. Jiang, B. Yang, and D. L. Klarstrom. *Mechanics of Materials*, 36(1-2):85–98, 2004.

[37] Y. H. He, L. J. Chen, P. K. Liaw, R. L. McDaniels, C. R. Brooks, R. R. Seeley, and D. L. Klarstrom. *International Journal of Fatigue*, 24(9):931–942, 2002.

[38] L. Jiang, P. K. Liaw, C. R. Brooks, and and D. L. Klarstrom B. Somieski. *Materials Science and Engineering A-Structural Materials Properties Microstructure and Processing*, 313(1-2):153–159, 2001.

[39] D. Broek. *The practical use of fracture mechanics*. Kluwer Academic Publishers, 1989.

[40] W. Elber. *Engineering Fracture Mechanics*, 2:37–45, 1970.

[41] W. Elber. *In Damage Tolerance in Aircraft Structures, Special Technical Publication*, 486(Philadelphica: American Society for Testing and Materials):230–43, 1971.

[42] B. Budiansky and J. W. Hutchinson. *Journal of Applied Mechanics*, 45:267–76, 1978.

[43] J. C. Newman. *Mechanics of Fatigue Crack Growth, Special Technical Publication*, 590:281–301, 1976.

[44] G. T. Gray, J. C. Williams, and A. W. Thompson. *Metallurgical Transactions*, 14(A):421–433, 1983.

[45] P. C. Paris, R. J. Bucci, E. T. Wessel, W. G. Clark, and T. R. Mager. *Stress Analysis and Growth of Cracks, Special Technical Publication*, 513:141–76, 1972.

[46] R. R. Skelton and J. R. Haigh. *Materials Science and Engineering*, 36:1–25, 1978.

[47] P. K. Liaw, T. R. Leax, and W. A. Logsdon. *Acta, Metallurgica*, 31(10):1581–1587, 1983.

[48] S. Suresh, G. F. Zamiski, and R. O. Ritchie. *Metallurgical Transactions*, 31:1581–7, 1981.

[49] P. K. Liaw, T. R. Leax, R. S. Williams, and M. G. Peck. *Metallurgical Transactions A-Physical Metallurgy and Materials Science*, 13(9):1607–1618, 1982.

[50] J. E. King. *Fatigue of Engineering Materials and Structures*, 5:177–88, 1982.

[51] A. G. Pineau and R. M. N. Pelloux. *Metallurgical Transactions*, 5(A):1103–12, 1974.

[52] E. Hornbogen. *Acta Metallurgica*, 26:147–52, 1978.

[53] S. Suresh. *Metallurgical Transactions*, 14(A):2375–85, 1983.

[54] S. Suresh. *Fracture Mechanics*, 18:577–93, 1983.

[55] R. Marissen, K. H. Trautmann, and H. Nowack. *Engineering Fracture Mechanics*, 19:863–79, 1984.

[56] K. Gall, H. Sehitoglu, and Y. Kadioglu. *Matall Mater Trans A*, 27(A):3491–502, 1996.

[57] K. Solanki, S. R. Daniewicz, and J. C. Newman Jr. *Engineering Fracture Mechanics*, 70:1475–1489, 2003.

[58] J. R. Rice. *American Society for Testing and Materials ASTM STP, In Fatigue crack propagation*, (415):247–309, 1967.

[59] R. S. Blandford, S. R. Daniewicz, and J. D. Skinner. *Fatigue Fract Engng Mater Struct*, 25(1):17–26, 2002.

[60] R. G. Chermahini and A. F. Blom. *Theor Appl Fract Mech*, 15:267–76, 91.

[61] R. G. Chermahini, K. N. Shivakumar, and J. C. Newman. *ASTM STP*, 982:398–413, 1988.

[62] J. Z. Zhang. *Engng Fract Mech*, 60:341–60, 1998.

[63] J. D. Skinner and S. R. Daniewicz. *Engng Fract Mech*, 69:1–11, 2002.

[64] W. T. Riddell, R. S. Piascik, M. A. Sutton, W. Zhao, S. R. McNeil, and J. D. Helm. *ASTM STP*, 1343(2):157–74, 1999.

[65] D. S. Dugdale. *J. Mech. Phys. Solids*, 8:100–1–4, 1960.

[66] G. Barenblatt. *Advances in applied Mechanics*, 5:55–129, 1962.

[67] X. Xu and A. Needleman. *International Journal of Fracture*, 74:289–324, 1995.

[68] G. T. Camacho and M. Ortiz. *International Journal of Solids and Structures*, 33:2899–2938, 1996.

[69] I. Scheider. *found from website*, 2001.

[70] V. Tvergaard. *Material Failure by Void Growth to Coalescence*. Academic press, 1990.

[71] I. Scheider. *Bruchmechanische Bewertung von Laserschweiverbingdungen durch mumerische Rifortschrittsimulation mit dem Kohsivzonenmodell*. PhD thesis, TU, Hamburg-Harburg, Geesthacht, 2001.

[72] A. M. Cuitino and M. Ortiz. *International Journal of Solids and Structures*, 9:437–451, 1992.

[73] O. Nguyen, E. A. Repetto, M. Ortiz, and R. A. Radovitzky. *International Journal of Fracture*, 110:351–369, 2001.

[74] T. Anderson. *Fundamentals and Applications*. Boca CRC Press, Boca Ration, 1995.

[75] Hibbitt, Karlsson, and Sorensen. *ABAQUS Theory manual 5.8 Hibbitt, Karlsson and Sorensen*, 1998.

[76] M. Lang and G. Marci. *Fatigue Fract Eng Mater Struct*, 22:257, 1999.

[77] J. Schijve. *Advances in Aeronautical Sciences*, 3:387–408, 1962.

[78] J. Schijve, D. Rijk, and J. Broek. Technical Report NLR-TN M. Amsterdam, National Aero- and Astronautical Research Institute, 1961.

[79] R. C. Rice and R. I. Stevens. In *ASTM STP*, volume Seveneenth of *536*, page 95. 1973.

[80] R. P. Wei, T. T. Shih, and J. H. Fitzgerald. Technical Report CR-2239, Fitzgerald JH, 1973.

[81] L. G. Vargas and R. I. Stephens. In *3rd Int. Conference on Fracture*. Munich, Germany, 1973.

[82] V. W. Trebules Jr, R. Roberts, and R. W. Hertzberg. In *ASTM STP*, volume 536. 1973.

[83] W. J. Mills and R. W. Hertzberg. *Eng. Fract. Mech.*, 8:657, 1976.

[84] J. D. Almer, J. B. Cohen, and R. A. Winholtz. *Metallurgical and Materials Transactions A- Pysical Metallugrgy and Meterials Science*, 29(8):2127–2136, 1998.

[85] J. Smith, M. N. Bassim, C. D. Liu, and T. M. Holden. *Engineering Fracture Mechanics*, 52(5):843–851, 1995.

[86] H. Tada, P. C. Paris, and G. R. Irwin. *The stress analysis of cracks handbook*. Paris Productions, Inc., St Louis, MO, 2nd edition, 1985.

[87] P. K. Liaw, T. R. Leax, R. S. Williams, and M. G. Peck. *Acta, Metallurgica*, 30(12):2071–2078, 1982.

[88] P. K. Liaw, A. Saxena, V. P. Swaminathan, and T. T. Shin. *Metallurgical Transactions A-Physical Metallurgy and Materials Science*, 14(8):1631–1640, 1983.

[89] W. A. Logsdon, P. K. Liaw, and M. A. Burke. *Engineering Fracture Mechanics*, 36(2):183–218, 1990.

[90] W. A. Logsdon and P. K. Liaw. *Engineering Fracture Mechanics*, 24(5):737–751, 1986.

[91] L. J. Chen, P. K. Liaw, R. L. McDaniels, and D. L. Klarstrom. *Metallurgical and Materials Transactions A-Physical Metallurgy and Materials Science*, 34A(7):1451–1460, 2003.

[92] M. A. M. Bourke, D. C. Dunand, and E. Ustundag. *Applied Physics A-Materials Science Processing*, 74:S1707–S1709, 2002.

[93] H. M. Rietveld. *Journal of Applied Crystallography*, 2:65–71, 1969.

[94] D. J. Smith, R. H. Leggatt, G. A. Webster, H. J. Macgillivray, P. J. Webster, and G. Mill. *Journal of Strain Analysis for Engineering Design*, 23(4):201–211, 1988.

[95] X. L. Wang, Y. D. Wang, A. D. Stoica, D. J. Horton, H. Tian, P. K. Liaw, H. Choo, J. W. Richadson, and E. Maxey. *Materials Science and Engineering A-Structural Materials Properties Microstructrue and Processing*, 399(1-2):114–119, Jun 2005.

[96] V. W. Trebules Jr., R. Roberts, and R. W. Hertzberg. In *ASTM Special Technical Publication 536*, pages 115–116. 1972.

[97] A. P. Renolds. *Fat Fract Eng Mat Struct*, 15:551–62, 1992.

[98] E. P. Philips. *NASA Technical Memorandum 101601*. Langley Research Center, Hampton. VA, 1989.

[99] C. M. Ward-Close and R. O. Ritchie. *ASTM STP 982*, pages 529–535, 1988.

[100] C. S. Shin and S. H. Hsu. *International Jounal of Fatigue*, 15(3):181–192, 1993.

[101] P. J. E. Forsyth and D. A. Ryder. *Aircraft Engineering*, 32:96–99.

[102] S. Suresh. *Fatigue of materials*. Cambridge university press, 1991.

[103] Y. N. Sun, H. Choo, P. K. Liaw, Y. L. Lu, B. Yang, D. W. Brown, and M. A. M. Bourke. *Scripta Materialia*, 53(8):971–975, 2005.

[104] J. D. Budai, W. G. Yang, N. Tamura, J. S. Chung, J. Z. Tischler, B. C. Larson, G. E. Ice, C. Park, and D. P. Norton. *Nature Materials*, 2(7):487–492, 2003.

[105] R. Barabash, G. Ice, and F. Walker. *J. Appl. Phys*, 93:1457, 2003.

[106] R. Barabash, G. Ice, B. Larson, G. Pharr, K. Chung, and W. Yang. *Appl. Phys. Lett*, 79:971, 2001.

[107] M. A. Krivoglaz. Springer, Berlin, 1996.

[108] M. A. Krivoglaz. *Theory of X-ray and Thermal Neutron Scattering by Real Crystals*. Plenum Press, 1969.

[109] J. Mckittrick, P. K. Liaw, S. I. Kwun, and M. E. Fine. *Metallurgical Transactions A-Physical Metallurgy and Materials*, 12:1535, 1981.

[110] W. Woo, H. Choo, D. W. Brown, M. A. M. Bourke, Z. L. Feng, S. A. David, C. R. Hubbard, and P. K. Liaw. *Applied Physics Letters*, 86:231902, 2005.

[111] H. Choo, D. Seo, J. Beddoes, M. A. M. Bourke, and D. W. Brown. *Applied Physics Letters*, 85:4654, 2004.

[112] H. Choo, M. A. M. Bourke, P. Nash, M. Daymond, and N. Shi. *Materials Science and Engineering A-Structural Materials Properties Microstructure and Processing*, 264(1-2):108, 1999.

[113] K. Tao, H. Choo, H. Li, B. Clausen, D. W. Brown, J. E. Jin, and Y. K. Lee. *Residual Stresses VII Materials Science Forum*, 524-525:639, 2006.

[114] G. E. Ice, J. W. J. Pang, R. I. Barabash, and Y. Puzyrev. *Scripta Materialia*, 55:57, 2006.

[115] R. I. Barabash, G. E. Ice, and J. W. L. Pang. *Materials Science and Engineering A-Structural Material Properties Microstructure and Processing*, 400:125, 2005.

[116] Y. F. Gao and A. F. Bower. *Modeling Simul. Mater. Sci. Eng*, 12:453, 2004.

[117] S. M. Xia, Y. F. Gao, A. F. Bower, L. C. Lev, and Y. T. Cheng. *International J. of Solids Structure*, in press, 2006.

[118] J. Willenborg, R. M. Engle, and H. Wood. *Technical Report TFR*, Los Angeles: North American Rockwell:701, 1971.

[119] K. Sadananda, A. K. Vasudevan, R. L. Holtz, and E. U. Lee. *International Journal of Fatigue*, page S233, 1999.

[120] C. Y. Hou and J. J. Charng. *International Journal of Fatigue*, 18(7):463–474, 1996.

[121] L. Clapham, R. Sabet-Sharghi, T. Holden, and D. L. Atherton. *Physica B*, 241:1240–1243, 1997.

[122] P. K. Liaw, A. Saxena, and J. Schaefer. *Engineering Fracture Mechanics*, 32(5):675, 1989.

[123] P. K. Liaw, G. V. Rao, and M. G. Burke. *Materials Science and Engineering A-Structural Materials Properties Microstructure and Processing*, 131(2):187, 1991.

[124] P. K. Liaw, A. Saxena, and J. Schaefer. *Engineering Fracture Mechanics*, 57(1):105, 1997.

[125] Y. L. Lu, P. K. Liaw, G. Y. Wang, M. L. Benson, S. A. Thompson, J. W. Blust, P. F. Browning, A. K. Bhattacharva, J. M. Aurrecoechea, and D. L. Klarstrom. *Science and Engineering A-Structural Materials Properties Microstructure and Processing*, 397(1-2):122, 2005.

Vita

Yinan Sun (Julia) was born in Shenyang, Liaoning, China, in March 1979. She attended Shenyang Univeristy, where she received a Bachelor of Science degree from the Civil Engineering Department in 2001. She entered the Material Science and Engineering graduate program in spring 2003 and earned her Master of Science degree in 2006 and Doctor of Philosophy degree in 2007.